Important Notice

UNIVERSITY OF CALGARY

Estimating elastic properties of sandstone reservoirs using well logs and seismic inversion

by

Maria Fernanda Quijada

A THESIS

SUBMITTED TO THE FACULTY OF GRADUATE STUDIES

IN PARTIAL FULFILMENT OF THE REQUIREMENTS FOR THE DEGREE OF

MASTER OF SCIENCE

DEPARTMENT OF GEOSCIENCE

CALGARY, ALBERTA

APRIL, 2009

UNIVERSITY OF CALGARY

FACULTY OF GRADUATE STUDIES

The undersigned certify that they have read, and recommend to the Faculty of Graduate Studies for acceptance, a thesis entitled "Estimating elastic properties of sandstone reservoirs using well logs and seismic inversion" submitted by Maria Fernanda Quijada in partial fulfillment of the requirements for the degree of Master of Science.

_____

Supervisor, Dr. Robert R. Stewart, Department of Geoscience

_____

Dr. Larry Lines, Department of Geoscience

_____

Dr. Jörn Davidsen, Department of Physics and Astronomy

_____

Date

ABSTRACT

Well logs and seismic data from a heavy oilfield in east-central Saskatchewan are analyzed to estimate the elastic properties of the reservoir facies. The sand-shale interface is characterized by a significant increase in S-wave velocities (Vs), from 800 to 1300 m/s, and almost no change in P-wave velocities. Within the target zone, density values lower than 2250 kg/m^3 are diagnostic of sands. Reservoir sands from Assam, India also have an anomalous Vs response. Including prior lithological information is necessary to model accurate elastic parameters over the complete depth interval. Polarity changes at the reservoir levels and different frequency content of the PP and PS volumes significantly affect the registration and interpretation process. Productive channels are indicated by low-impedance zones, driven by the density decrease in the sands. The mudrock line consistently underestimates Vs values in sands, suggesting the Vs residual can generally be used as a sand indicator.

ACKNOWLEDGEMENTS

For all his help, guidance and support during my M.Sc. Program, I am immensely grateful to my supervisor, Dr. Robert Stewart. I also extend my thanks to Dr. Gary Margrave for helping me understand the world of processing and inversion a little bit better, and especially for getting me started in writing technical papers in English.

Many thanks to all the Professors and staff in CREWES for all their help and feedback during every presentation made to the group. Special thanks to Louise Forgues for keeping things organized and being always available.

This project could not have been done without the well logs and seismic data from Manitou Lake, provided by Calroc Energy Inc, and from the Assam province, provided by Oil India Ltd. Thanks to Hampson-Russell for the use of donated software (Geoview).

The data gathering and use of software could not have been done without the help of Kevin Hall and Rolf Maier. Thank you very much! Also, processing of the PP and PS data from Manitou Lake was performed by Han Xin Lu. Many thanks to Zimin Zhang for providing the Matlab code for modelling effective media, and to Roxana Varga for many useful conversations and feedback about the Manitou Lake project.

Thanks to fellow CREWES students for making my stay at the University a very positive and rewarding experience. Finally, I would like to thank the CREWES sponsors for their financial support.

TABLE OF CONTENTS

LIST OF FIGURES

LIST OF TABLES

LIST OF SYMBOLS

3C	3-Component
3D	3-Dimension
a	Archie's tortuosity factor
AHF30	Induction resistivity (30 inch)
AHF60	Induction resistivity (60 inch)
AVO	Amplitude Versus Offset
BHS	Borehole Compensated Sonic
BHT	Bottom Hole Temperature
DSI	Dipole Shear Sonic Imager
DPHI_SAN	Density porosity using sandstone matrix
DT	P-wave sonic
GR	Gamma Ray
HCAL	Caliper
I_p	P-wave Impedance
I_s	S-wave Impedance
m	Archie's porosity exponent
n	Archie's saturation exponent
NPHI_SAN	Neutron porosity using sandstone matrix
PP	Downgoing and upcoming P-wave
PS	Downgoing P-wave and upgoing S-wave
RESD	Deep resistivity

RESM	Medium resistivity
RHOZ	Bulk density
R^{pp}	P-wave reflectivity
R^{ps}	Converted-wave reflectivity
R^{ss}	Pure-shear reflectivity
R_w	Formation water resistivity
R_{mf}	Mud filtrate resistivity
RXOZ	Shallow resistivity
S_w	Water saturation
S_{xo}	Flushed zone saturation
TEMP	Temperature
V_p	P-wave velocity
V_p / V_s	Ratio between P-wave and S-wave velocity
V_s	S-wave velocity
V_{sh}	Shale volume
ρ	Density
Λ	Wavelength
ϕ_e	Effective porosity
θ	Incidence angle

CHAPTER ONE: INTRODUCTION

1.1. ELASTIC PROPERTIES

The prediction of elastic properties such as density, P- and S-wave velocities, as well as their relations to rock properties such as lithology, porosity or fluid content, is critically important in reservoir characterization. This analysis also constitutes a crucial step for different applications such as seismic modelling, amplitude versus offset (AVO) variations.

Seismic velocities are affected by mineralogy, porosity, pore geometry and fluid, effective stress, cementation, and fractures (McCormack et al., 1985). Shear waves are slower than compressional waves, polarized and cannot propagate through fluids, making converted-wave exploration useful for fluid and lithology discrimination, imaging structure through gas clouds and fracture detection by analysis of shear wave splitting, among other applications (Garotta et al., 2002).

The bulk density of a rock is a function of porosity, hydrocarbon fluid type, water saturation, and mineral composition. Crossplots between rock properties and lithology and pore fluid indicate that density often provides the best differentiation between hydrocarbon reservoirs and other rock/fluid types (Van Koughnet et al., 2003), making accurate density estimates significant for reservoir characterization. Density can also be an important acoustic indicator of the presence of shale, making it an important parameter in oil sands or heavy oil developments where accurate density estimates are necessary to determine the location of shales in the reservoirs, which may interfere with the steaming or recovery process (Gray et al., 2006). Coal density varies with ash, water content, and rank (Ryan,

2006); with higher ash content generally implying a higher specific gravity and lower gas content, suggesting that density can be a key factor in determining the quality of the coal.

Well logging allows direct measurement of elastic-wave characteristics in the proximity of the wellbore, which can be translated into rock properties using different rock models and formulations. Extrapolating these properties to locations away from the wells can be done by generating facies models using several wells in the area, or by correlating them to certain attributes from seismic data. The latter requires accurate correlation of the wells with the seismic data, as well as the definition of appropriate rock physics models. In general, two parameters (i.e., P- and S-impedance, or P- and S-wave velocity) can be reliably estimated from PP and PS seismic inversion (Downton, 2005; Mahmoudian, 2006). However, the lithology and fluid properties of a medium sometimes cannot be inferred from P-wave data alone, requiring information from the S-wave and/or density response. Density can also be estimated from seismic data by seismic inversion (i.e. AVO or waveform inversion) or by geostatistical methods, where linear (i.e. multi-linear regression) or non-linear (i.e. neural networks) relationships can be established between the rock properties calculated at the well location, and the seismic data or a specific seismic attributes. For the density case, the inverse problem is ill-posed, with a small change in the data resulting in a large change in the solution, and unstable, requiring the inclusion of constraints on the parameters to stabilize it (Wang, 1999).

In the following chapters several aspects of the estimation of elastic properties are evaluated. Well log data is analysed to better define the correlation between elastic and rock properties in the area of study. Different empirical and rock physics approaches are used to estimate elastic properties from different logs, and to define local parameters.

Finally, elastic parameters are estimated from seismic data by post-stack inversion of PP and PS volumes.

1.2. AREAS OF STUDY

Two different areas were evaluated during the course of this project. The first data set corresponds to the Manitou Lake oilfield in Saskatchewan, while the second data set is from the Assam province in north-eastern India.

1.2.1. Manitou Lake, Saskatchewan

The Manitou Lake oilfield is located in west central Saskatchewan, approximately 50 km southeast of the city of Lloydminster (Figure 1.1). Production in this field comes mainly from the Colony and Sparky B members of the Cretaceous Mannville group. The Lloydminster heavy oil accumulation is the southern extension of a discontinuous trend of Lower Cretaceous bitumen and heavy oil deposits, extending from Athabasca through Cold Lake to Lloydminster (Orr et al., 1977). Oil gravity in the Lloydminster pools ranges from 9 to 18 °API, falling within the range of 10-22.3 °API defined for heavy oil by the US Department of Energy.

The Sparky pool in the Manitou Lake field was discovered in 1970 and there are currently 159 wells producing heavy oil with a gravity of 15.1°API within an area of 1441 Ha. The mean depth of the Sparky reservoir is 605 m with a net pay of 4.05 m. Core data shows that the average maximum permeability is 573 mD, porosity is 16% and water saturation is 0.3.

Figure 1.1: Location of the Manitou Lake oilfield in west-central Saskatchewan (From GoogleMaps 2008). Red squares highlights the area of interest.

1.2.2. Assam province, Northeastern India.

The Assam area is located in northeastern India (Figure 1.2) and it constitutes one of the most important onshore petroleum provinces in India, producing oil and gas for more than a century. The NE-SW trending basin has similarly oriented faults which control some of the hydrocarbon traps, with most reservoirs occurring in anticlinal structures and some subtle stratigraphic traps. Current oil and gas production in the region occurs mainly south of the Brahmaputra River and north of the Naga thrust system (Figure 1.3).

Important hydrocarbon-producing strata include: the Paleocene Langpar, Eocene Sylhet and Kopili, the upper Eocene-Oligocene Barail Group, and Miocene Tipam and Girujan facies. The main target in this study is the Barail Group, which was deposited in a deltaic environment.

Figure 1.2: Location of the area of study, Assam Province in Northeastern India, highlighted with a red ellipse (From GoogleMaps, 2008).

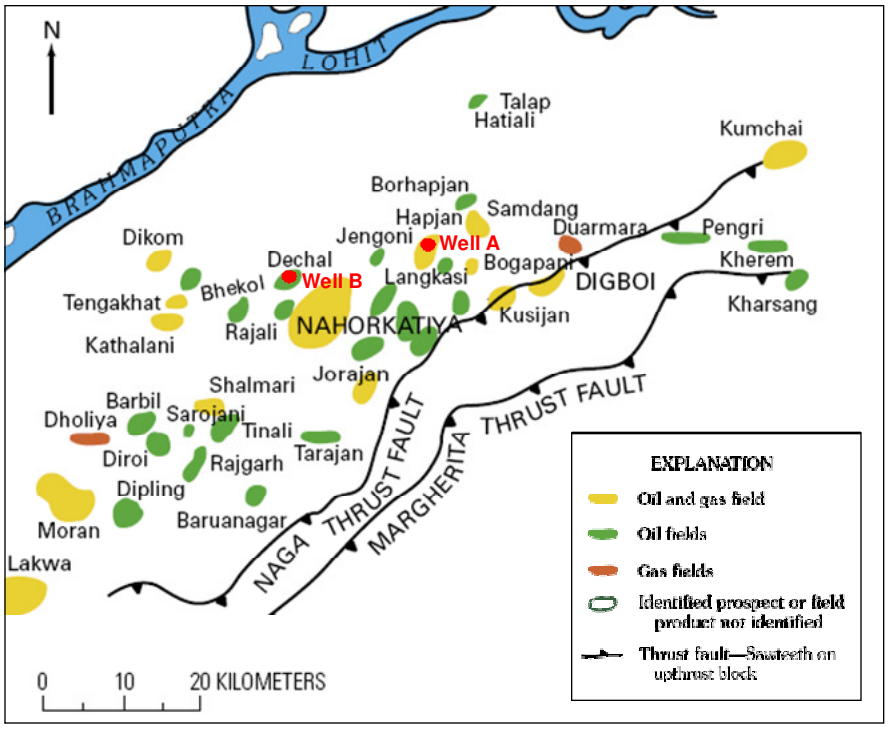

Figure 1.3: Location of oil and gas fields in the Assam geologic province. Location of Wells A and B is shown by red dots. Oil fields are shown in green, gas fields in red, and oil and gas fields in yellow (Modified from Wandrey, 2004)

1.3. GEOPHYSICAL DATA

1.3.1. Manitou Lake, Saskatchewan

The data available from the Manitou Lake oilfield includes a suite of logs from three wells, named A11-17, C07-16 and C10-17, as well as a 3D-3C seismic survey in the area (See Figure 1.4). A standard suite of logs, including Gamma-ray (GR), caliper (HCAL), spontaneous potential (SP), density (RHOB), neutron (NPHI) and density porosity (DPHI) for sandstone matrix, and shallow (RXOZ), medium (AHF30) and deep (AHF60) resistivity were available for each well. Note that most wells drilled in the area are following linear trends, generally associated with sand channel deposits.

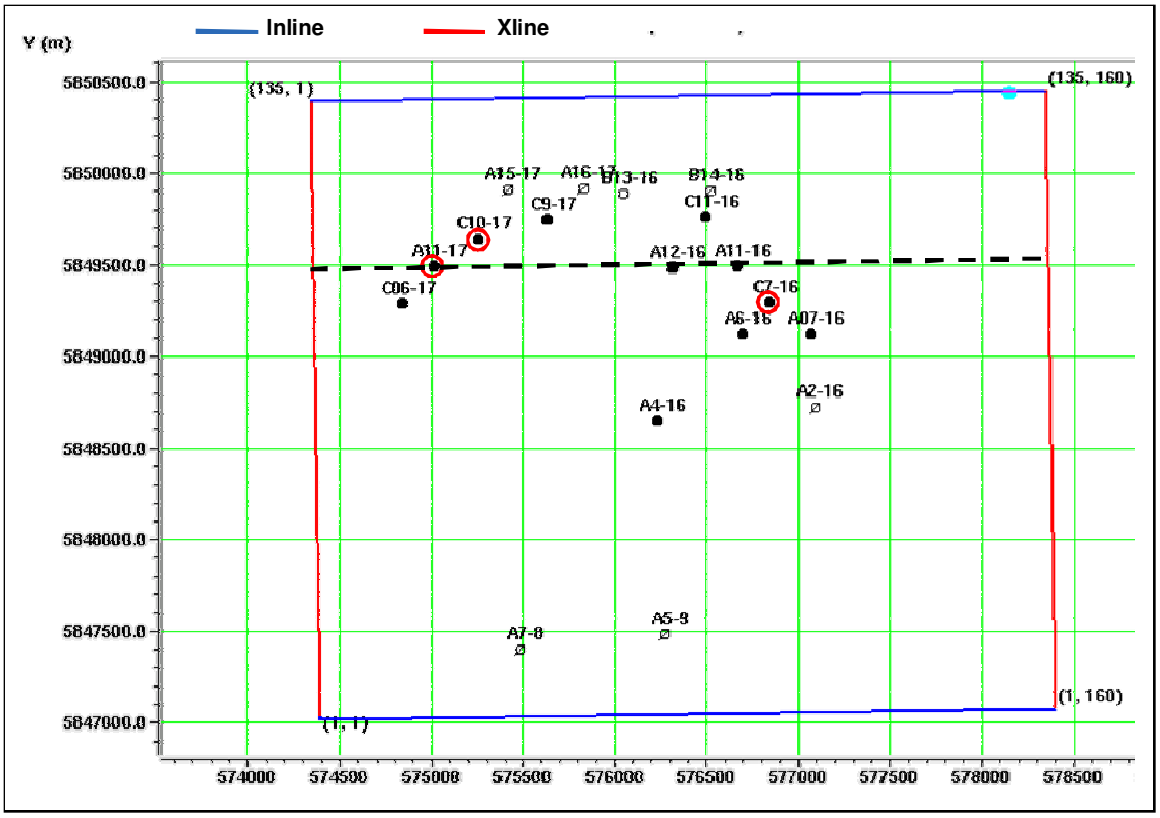

Figure 1.4: Base map for the seismic survey. Black dots indicate wells within the 3D survey, and highlighted in red circles are the wells used in this project. Dashed line indicates location of inline 100.

Figures 1.5 and 1.6 show a typical suite of logs for wells A11-17 and C07-16 over the complete depth interval, which generally ranged from 100 to 600 m depth. P-wave sonic is only available for these two wells, while an S-wave sonic was also acquired in well A11-17. Note the distinct change in character on all the logs at the top of the Colony interval (approximately at 550 m), which separates the predominant shales of the Colorado Group from the sandier Mannville interval. There appears to be little variability of the elastic properties (i.e. density, P- and S-wave velocity) in the shaly section in comparison to the more significant changes seen in these properties within the Mannville interval, where the sands are interbedded with shales and several coal seams.

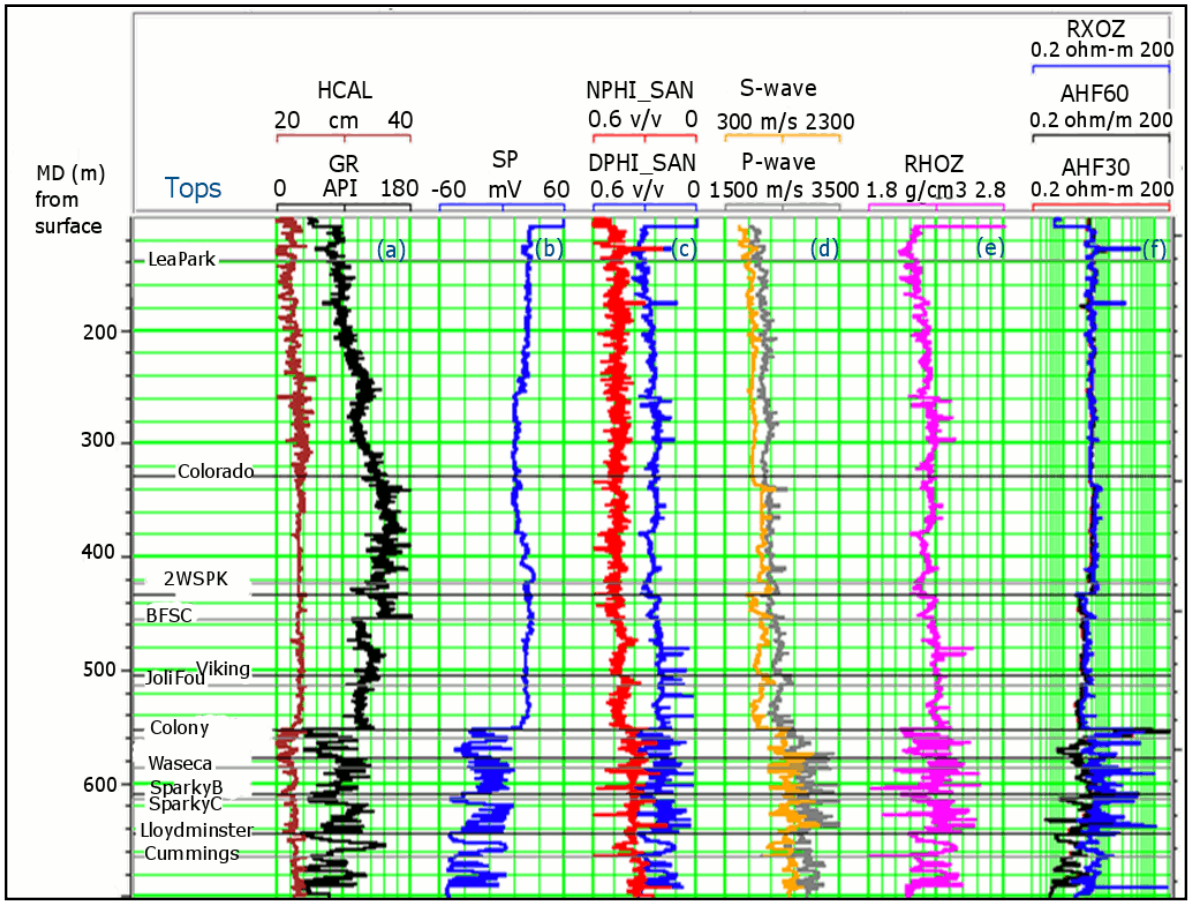

Figure 1.5: Suite of logs from well A11-17 in the Manitou Lake oilfield, Saskatchewan. Tops are shown in the left. (a)GR and calliper, (b) Spontaneous potential, (c) neutron and density porosity, (d) P- and S-wave velocity, (e) density, and (f)resistivity.

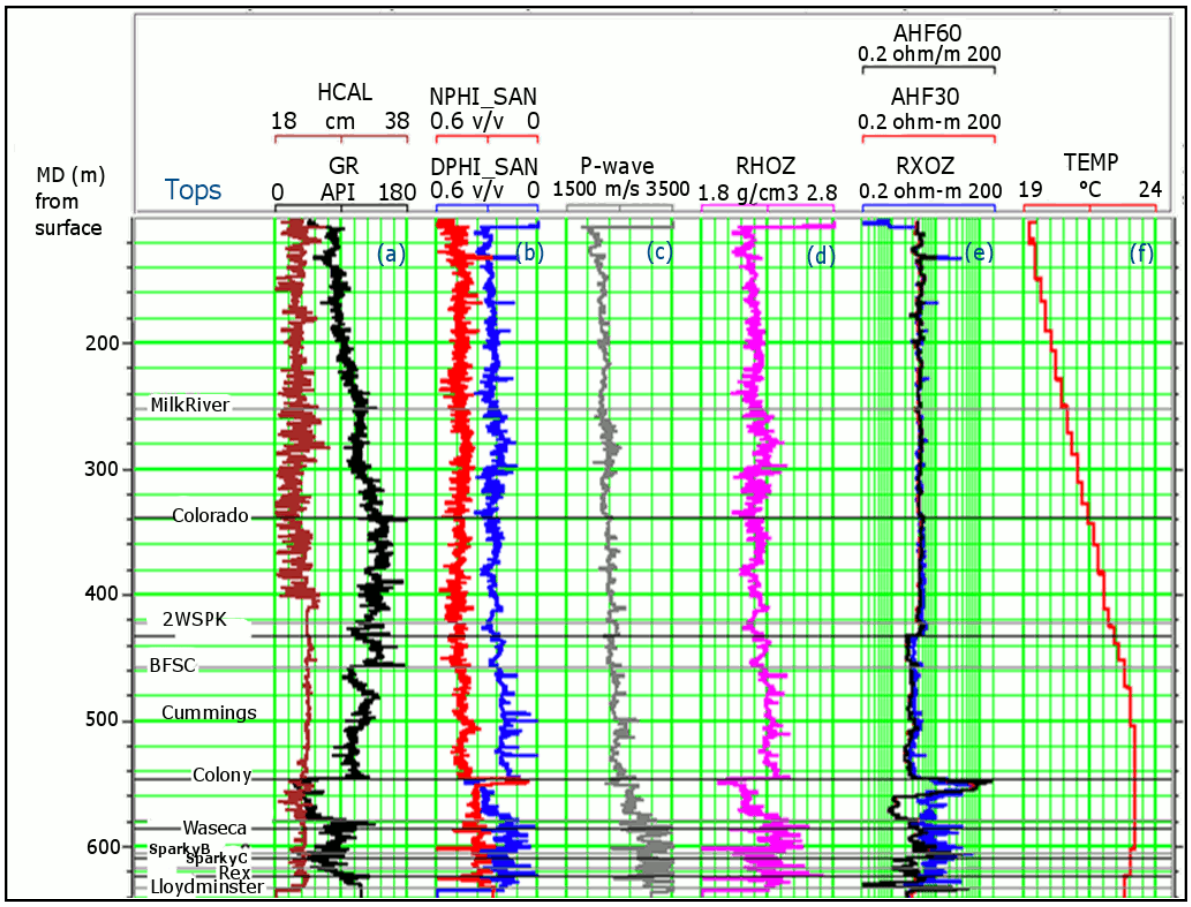

Figure 1.6: Suite of logs from well C07-16 in the Manitou Lake oilfield, Saskatchewan. Tops are shown in the left. (a)GR and calliper, (b) neutron and density porosity, (c) P-wave velocity, (d) density, (e)resistivity, and (f) temperature.

A seismic survey was acquired for Calroc Energy Inc. by Kinetex Inc. in February 2005, consisting of twenty-one south-north receiver lines and eighteen west-east source lines (Figure 1.7), with 200 m line spacing and 50 m station spacing (Lu et al., 2006). The survey covers an area of approximately 14 Km2, with 135 inlines running East-West, and 160 crosslines running North-South. The exploration targets of this survey were sand channels within the Colony and Sparky members of the Mannville Group, which are currently producing oil in the area. Well A11-17 is producing oil from the Colony interval, while C07-16 and C10-17 are producing oil from the Sparky interval. Multicomponent data was acquired in an attempt to better delineate the reservoir sand channels.

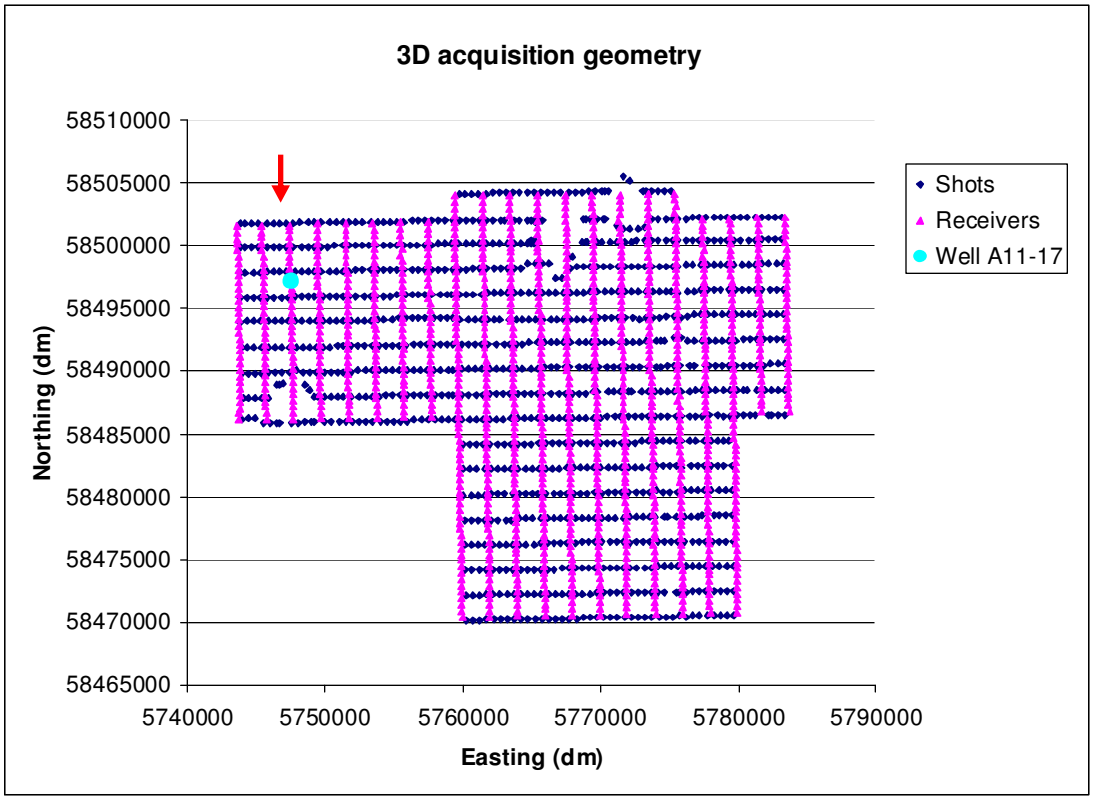

Figure 1.7: Acquisition geometry for the Manitou Lake Survey. Shots are displayed in blue, and receivers in purple. Location of well A11-17 is indicated by the cyan circle.

PP and PS stacked volumes and gathers were used to estimate elastic parameters through seismic inversion. The volumes have 135 inlines and 160 crosslines. Migrated vertical and radial stacked sections along inline 100 are shown in Figures 1.8 and 1.9, respectively. Note the lower resolution of the converted wave with respect to the P-wave data, as well as the lower quality in the shallower and deeper parts of the section. Target horizons are between 450 and 600 ms in PP time, and between 1000 and 1300 ms in PS time.

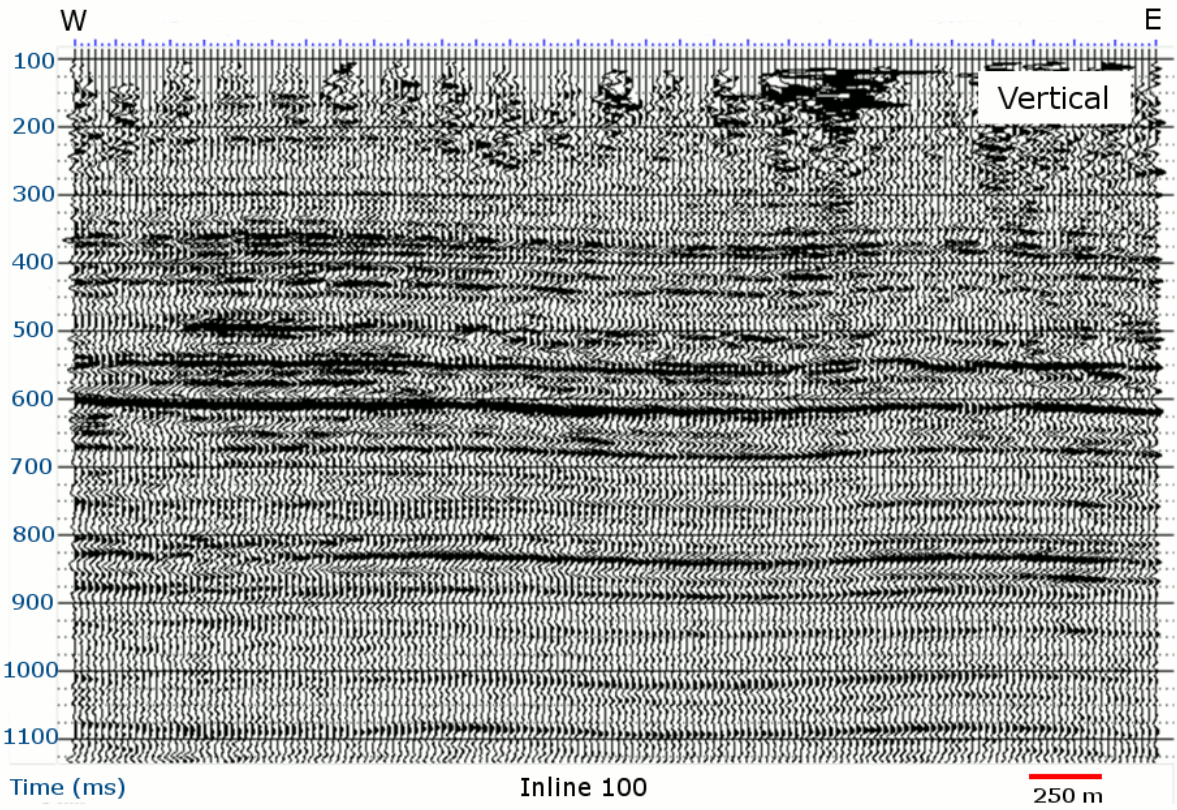

Figure 1.8: Vertical component from the migrated stack along inline 100.

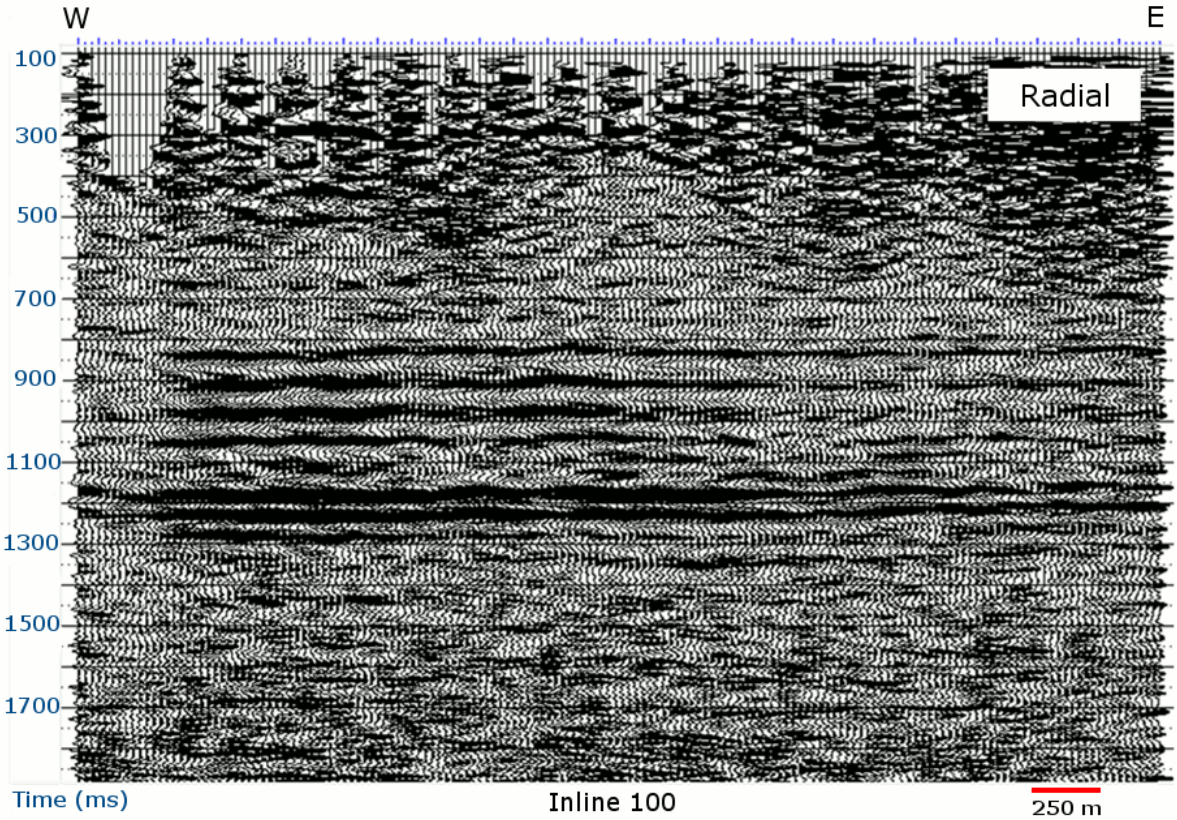

Figure 1.9: Radial component from the migrated stack along inline 100.

1.3.2. Assam Province, Northeast India

A full suite of logs from two wells in the Assam province was available to develop a feasibility study on the improvements multicomponent seismic could bring to the hydrocarbon exploration efforts in the area. Well A is located in the oil and gas producing Hapjan field, while Well B is located in the gas producing Deohal field (See Figure 1.3 for location). The suite of logs includes GR, caliper, spontaneous potential, P- and S- wave sonic, density, resistivity and porosity logs, among others.

The reservoir sands in the area are generally thin fluvial deposits, interbedded with shales and coal seams. Main targets in the area are within the Tipam and Barail formations, both of which are encountered at depths of over 2000 m. Average GR values are around 70 API degrees, showing the predominantly shaly character of the section. The calliper log shows several washouts, which seem to correlate with zones of questionable density and S-wave sonic readings (Figures 1.10 and 1.11).

1.4. PREVIOUS WORK

The estimation of elastic parameters such as shear wave velocity and density has become crucial for reservoir characterization, especially in cases where the P-wave information leads to ambiguous results. Pickett (1963) was one of the first to suggest using V_p/V_s as a lithologic indicator, by determining V_p/V_s values from core measurements from different types of rocks, such as dolomite, limestone and sandstone. Clay content can also significantly affect V_p/V_s values, as it makes the rock less resistant to shearing forces, lowering both V_p and V_s, but having a greater effect on V_s, which results in an overall increase in V_p/V_s (Minear, 1982).

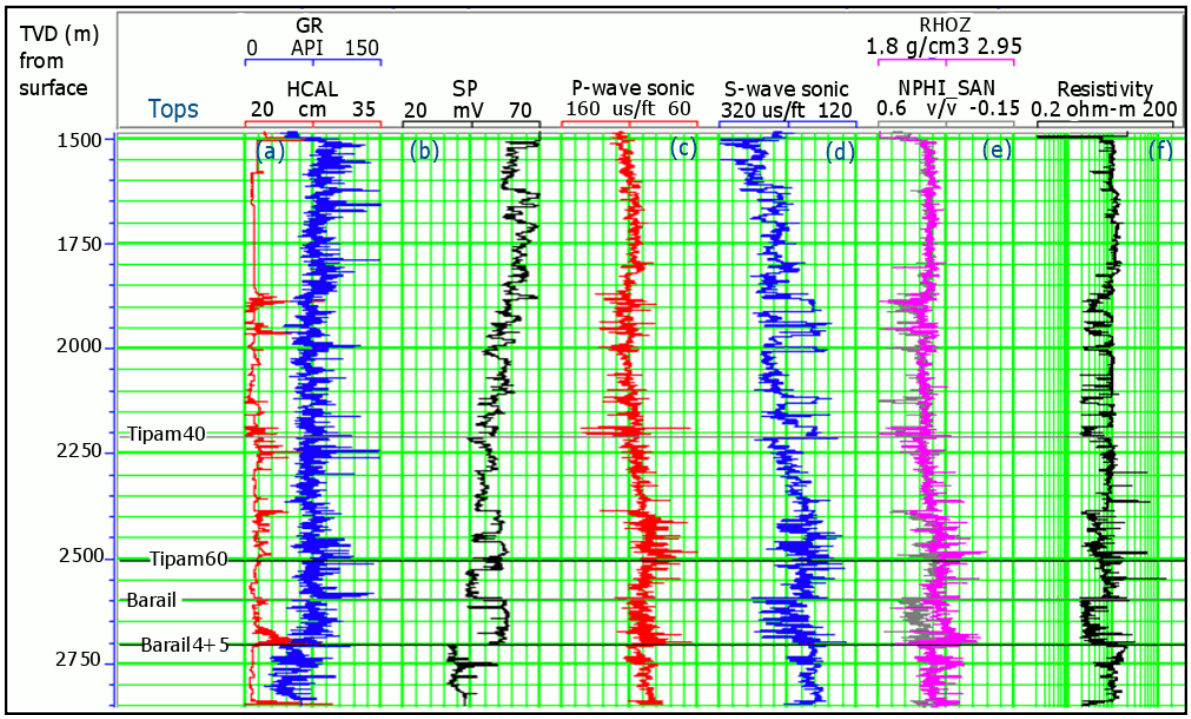

Figure 1.10: Suite of logs for well A in the Hapjan field, Assam province, India. (a)GR and calliper, (b) Spontaneous potential, (c) P-wave sonic, (d) S-wave sonic, (e) neutron porosity and density, and (f)resistivity.

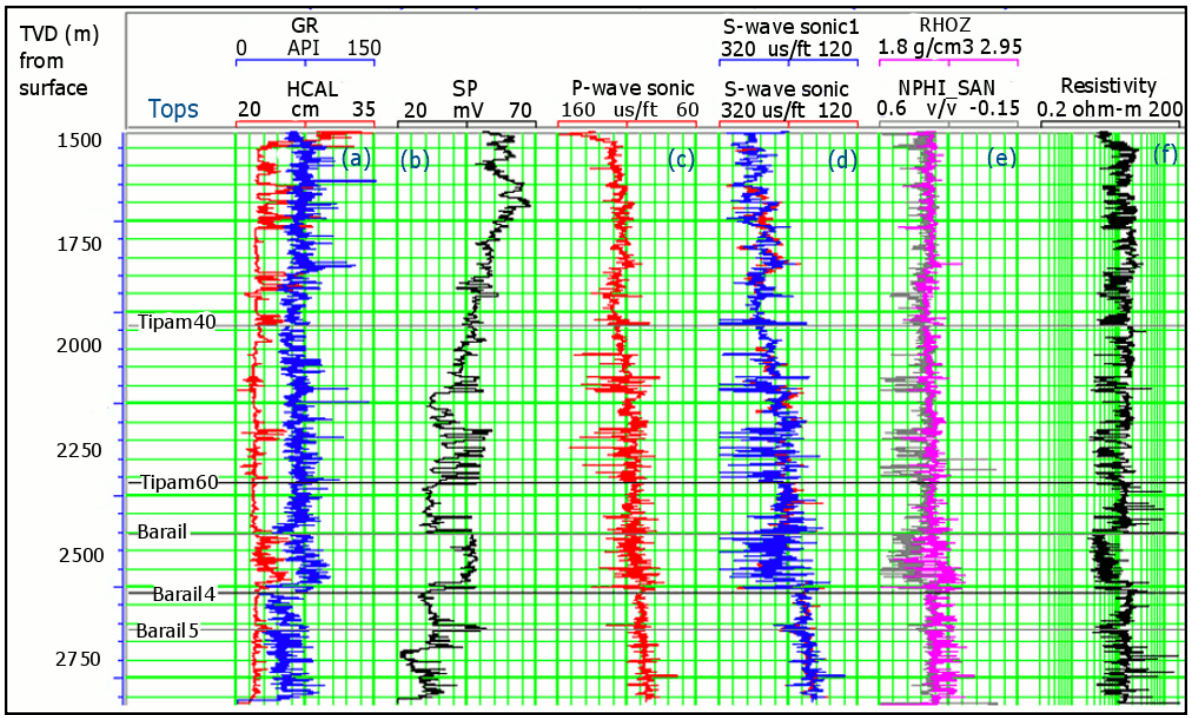

Figure 1.11: Suite of logs from well B in the Deohal field, Assam Province, India. (a)GR and calliper, (b) Spontaneous potential, (c) P-wave sonic, (d) dipole S-wave sonics, (e) neutron porosity and density, and (f)resistivity.

Several empirical relations have been developed to relate different elastic rock properties. Castagna et al. (1985) presented an empirical relation, known as the mudrock line, between P- and S-wave velocities for water saturated clastics. Wang (2000) developed another empirical equation that predicts S-wave velocity using the bulk density of the saturated rock, the pore fluid modulus and the P-wave velocity, allowing for other fluids besides water to fill in the pore space. Rock physics approaches have also been used for predicting elastic properties. Greenberg and Castagna (1992) predict Vs using Biot-Gassmann theory under the assumption that P- and S-wave velocities are related robustly and that nearly linear mixing laws for solid rock constituents are valid. Xu and White (1996) predict S-wave velocity using a combination of Kuster and Töksoz (1974) theory and the differential effective medium theory, incorporating pore aspect ratios to characterize the compliance of the sand and clay components.

The most widely used formulation to estimate density from velocity measurements is that of Gardner et al. (1974). They defined an exponential relationship between density and velocity, based on empirical studies and assuming high effective pressure and fluid saturation. Lindseth (1979) found an empirical linear relationship between acoustic impedance and P-wave velocity, which can also be used to estimate density from velocity information.

Multicomponent studies have not yet become widespread due to their higher cost and difficulty in the acquisition, processing and interpretation. However, converted-wave studies have been successful, especially for fluid and lithology estimations. A 3C-3D seismic survey was acquired in the Blackfoot field in southern Alberta with the objective of distinguishing prospective channel sands from non-productive shales, which showed a similar P-wave impedance response (Pendrel et al., 1999). In this area, Potter et al. (1996)

observed that the P-wave velocity of the shales is very similar or just slightly higher than that of the sands. Log analysis also shows that the shear wave velocity of the sands is greater than for the shales, indicating a decrease of V_p/V_s from shale to sand. Todorov (2000) integrated well logs with 3D-3C seismic data from the Blackfoot field to estimate rock properties, using inversion, geostatistics and multi-attribute analysis.

Several studies have also been done within the Lloydminster area. Soubotcheva (2006) used well logs and multicomponent seismic data to estimate reservoir properties of the productive Waseca interval in the Pikes Peak field, located 40 km east of Lloydminster. Her results show that V_p/V_s is a useful parameter to discriminate between sands and shales. Also, the Colony sand member in east-central Alberta and west-central Saskatchewan has been extensively explored using conventional seismic techniques, with bright spot anomalies on the amplitude maps being the main tool to delineate the sand channels. Royle (2002) used AVO and post-stack attributes to extract fluid and lithology information from seismic and well log data, in an attempt to better delineate the reservoir channels.

1.5. OBJECTIVES

The main objective of this project is to evaluate different methods for estimating elastic properties, both from well logs and multicomponent seismic data, focusing on their accuracy, applicability and limitations. It is also of interest to relate these elastic parameters to rock properties of interest, such as lithology and fluid content.

A secondary objective of the project is to evaluate the importance of different corrections for the wireline data and the empirical relations used, to account for effects of borehole conditions and local geology.

1.6. THESIS OUTLINE AND IMPLEMENTATION

Chapter 2 summarizes the petrophysical analysis of the Manitou Lake data set, showing the calculation of elastic properties using different empirical and deterministic approaches. Editing and display of the logs was done using the eLog application from HampsonRussell software. Matlab was used for fitting the well data to the different models used to predict elastic properties. Matlab code provided by Zimin Zhang was used to predict V_p and V_s using Kuster-Toksöz's formulation for effective media. Chapter 3 shows the synthetic seismograms generated from the well log data, as well as the results from the inversion of the PP and PS volumes. The Syngram application in Matlab was used to generate synthetic seismograms, while ProMC and Strata software from Hampson Russell was used for the interpretation and inversion of the seismic data.

CHAPTER TWO: PETROPHYSICAL ANALYSIS IN MANITOU LAKE, SASKATCHEWAN

2.1. INTRODUCTION

Wireline log measurements are translated into petrophysical properties (e.g. porosity, hydrocarbon saturation, and lithology) by the process of log interpretation or formation evaluation. In this way, reservoir quality can be related to seismic rock properties (P-and S-wave velocity and density) and consequently, to their seismic response.

Significant research has been recently guided towards studying the rock physics and elastic properties of heavy oil, which has shown significant deviations with respect to the properties of conventional oil, due to the high viscosity in the reservoirs. Heavy oil can be present in three different phases: liquid, quasi-solid and glass solid (Han et al., 2006), and acoustic velocities have shown different features at different phases. At high temperatures, when the heavy oil is in liquid phase, velocities are very similar to those observed in conventional oil, with negligible shear velocity and velocity dispersion, and with a near constant velocity gradient with respect to temperature (Han et al., 2008). At very low temperatures (heavy oil as a glass solid type), V_p and V_s should behave elastically and there is no dispersion. In intermediate states, where the heavy oil is in a quasi-solid phase, shear waves are able to propagate in the heavy oil and there is significant velocity dispersion. Kato et al. (2008) evaluate the changes in P- and S-wave velocities with pressure and temperature, using ultrasonic measurements in oil sand samples, in order to evaluate changes in elastic properties during the steam injection process. They found that the slope of P- and S-wave velocities as a function of temperature, at a constant pore pressure of 700 psi, significantly changes at around 30 °C, with velocities steeply decreasing in the lower

temperature range. They found that for temperatures higher than 80 °C Gassmann's equations are applicable for the high frequency ultrasonic lab measurements. The temperature log from wells A11-17 and C07-16 show a reservoir temperature of approximately 20 °C, suggesting velocity dispersion and shear wave propagation.

This chapter shows the results from the petrophysical analysis of the wireline data from Manitou Lake, Saskatchewan. Initially, logs are edited to remove spikes and correct for invasion problems, to ensure the logs are representing true formation properties. Different crossplots are then evaluated to understand the relations between the different elastic measurements and the actual rock properties (i.e. lithology, porosity, type of fluid in the pores, among others). Finally, several empirical and deterministic models (e.g. Gardner, log response equation, and Kuster-Toksöz) are used to predict elastic properties from other logs.

2.2. GEOLOGIC SETTING

Deposition in the Western Canada Sedimentary Basin (WCSB) can be divided into two major successions, based on two different tectonic settings affecting sedimentation. The Paleozoic to Jurassic platformal succession, dominated by carbonate rocks, was deposited on the stable craton adjacent to the ancient margin of North America. The overlying mid-Jurassic to Paleocene foreland basin succession, dominated by clastic rocks, formed during active margin orogenic evolution of the Canadian Cordillera, with the emplacement of imbricate thrust slices progressively from east to west (Mossop and Shetsen, 1994).

The geology of the Lloydminster heavy oil region is quite complex from depositional, structural and economical perspectives, due to extreme lateral facies variations and features associated with salt dissolution (Putnam, 1982). Most of the sediments in the area were deposited during the Cretaceous, and the top of the Mannville Group marks a clear separation between the predominant sands in Mannville and the overlying marine shales of the Colorado and Belly River Groups (See Figure 2.1).

In the area, the Mannville Group lies unconformably on Paleozoic strata, and its sedimentary pattern consists of an interplay of marine, estuarine and fluviatile agents acting in a setting controlled by paleo-topographic relief and eustatic and tectonic changes in relative sea-levels (Christopher, 1997). The thickness of Mannville sediments deposited in the area was controlled to a large degree by the relief on the pre-Cretaceous unconformity (Putnam, 1982). A correlation chart of the Mannville through Alberta, Saskatchewan and Manitoba (Figure 2.2) shows the change in nomenclature for the different units within the Mannville.

The Sparky member conformably overlies the General Petroleum and it is capped by a regional coal marker. It is informally grouped into the middle Mannville, which is dominated by sheet sandstone development, with narrow, channel sandstones and shales also present (Putnam, 1982). These units have been interpreted as a delta-front facies with associated tidal-flat, tidal-channel, and beach environments (Vigrass, 1977). The sheet sandstones in Sparky are commonly 6-9 m thick, and can be traced laterally for several tens of kilometers; however, they are commonly broken by thick ribbon-shaped deposits or sandstone pinchouts (Putnam, 1982).

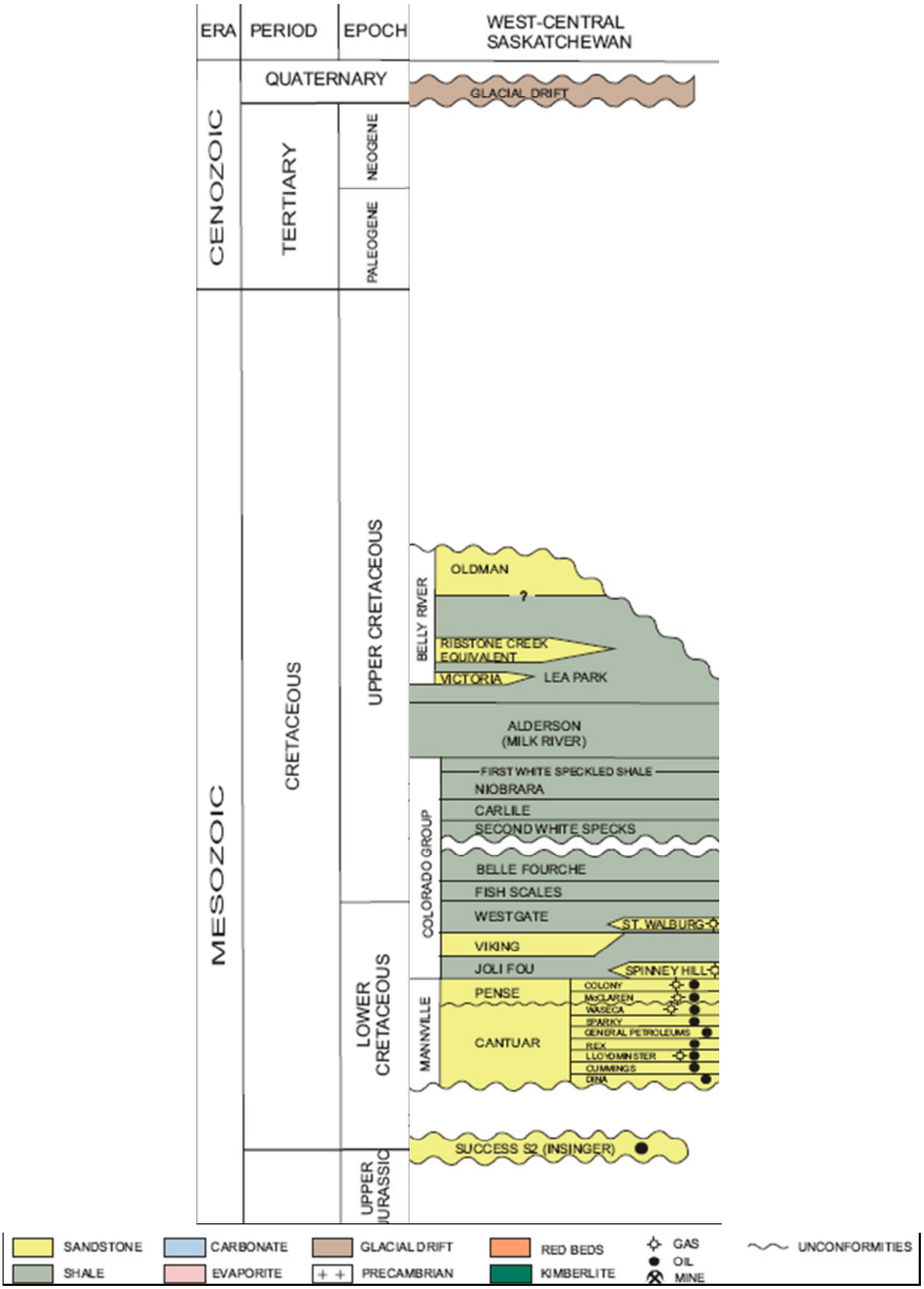

Figure 2.1: Stratigraphic column for west central Saskatchewan (From Saskatchewan Industry and Resources, 2006).

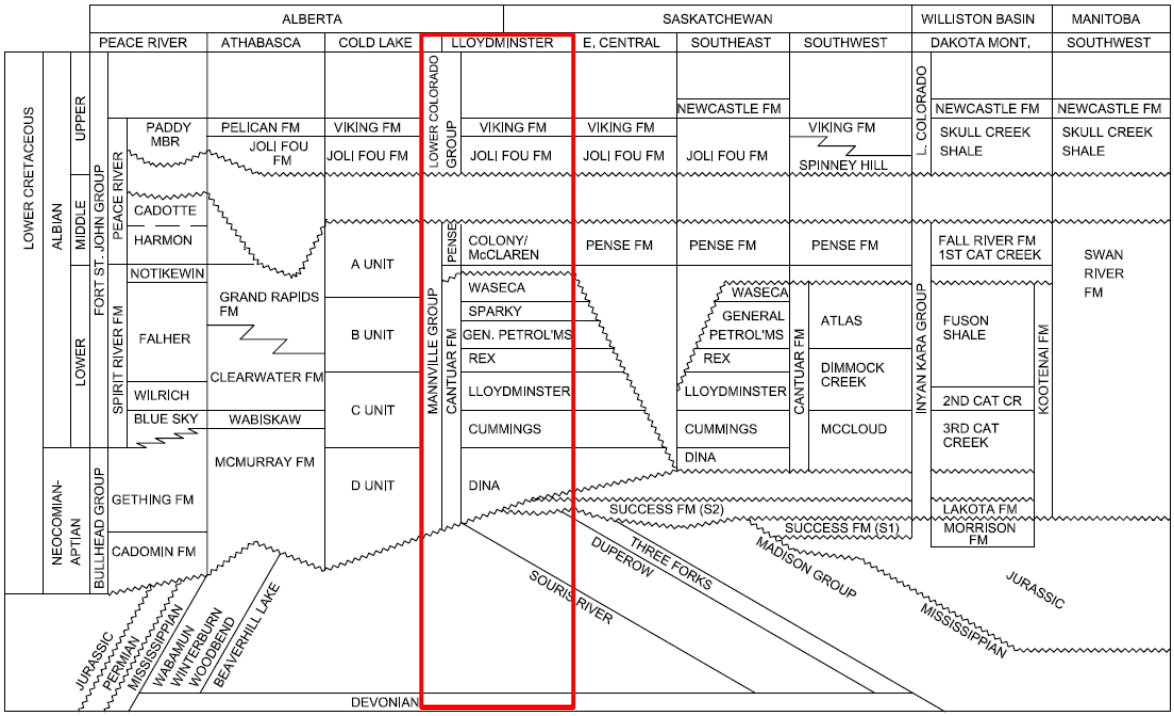

Figure 2.2: Correlation chart of units within the Mannville Group, with stratigraphy of the Lloydminster area highlighted by the red rectangle (Modified from Christopher, 2003).

The Colony member consists of shales, siltstones, coals and sandstones. Deposition of this member occurred in an extensive complex of anastomosing channels sandstones, encased within siltstones, shales, coals and thin sheet sandstones (Putnam and Oliver, 1980). Figure 2.3 shows a schematic depositional model for the Colony sands, including the three distinct facies: channel, crevasse splay and interchannel wetlands. Anastomosing channels have high sinousities, and are characterized by a tendency to split and rejoin at a scale many times the channel width and by prominent levees (Reading, 1996). Crevasse splays are discrete lobes of silty or sandy sediment that extend down the levee to the flood plain, from shallow crevasses on the crest (Reading, 1996). Within the area of study, the reservoir rocks are represented by the channel facies.

The marine shales of the Joli Fou formation unconformably overlay the Colony member, representing the basal unit of the Colorado Group. This group is dominated by

marine shales encasing generally thin but extensive sandstones, such as the Viking, Dunvegan and Cardium formations, which act as important petroleum reservoirs in other areas (Leckie et al., 1994). Within the Colorado Group, the First and Second White Speckled Shales, the Fish Scales Zone, and shale at the base of the Shaftesbury Formation are more radioactive than overlying and underlying shales, have high total organic carbon contents, and have considerable hydrocarbon generating potential. An interval such as the Second White Speckled Shale is potentially both a source and a reservoir rock for hydrocarbons (Mossop and Shetsen, 1994).

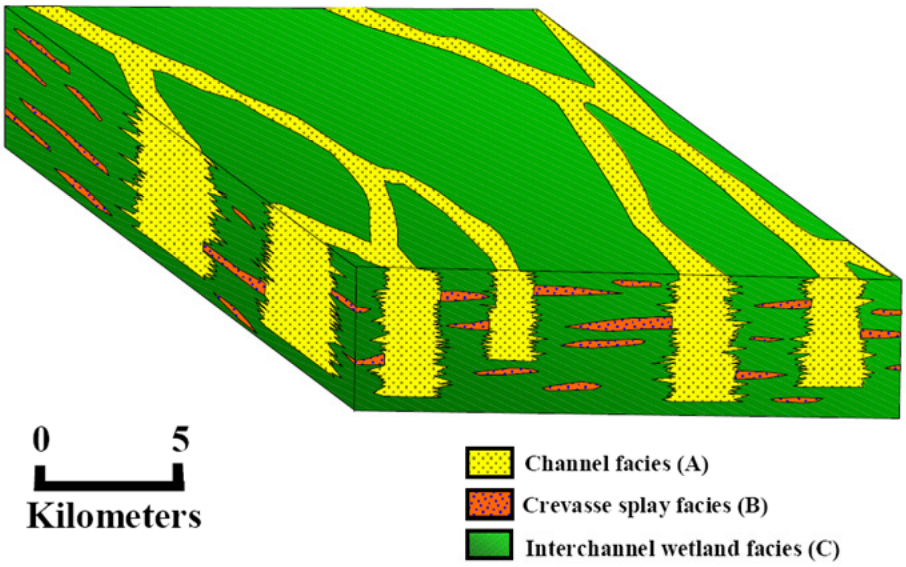

Figure 2.3: Schematic depositional model for the Colony sand member after Putnam and Oliver (1980) as reproduced from Royle (2002). Channel facies are highlighted in yellow, crevasse splays in red and interchannel wetlands in green.

Mannville sub-bituminous coal and lignite are widely distributed throughout central Saskatchewan. In the Lloydminster are, several coal seams are found within the Mannville Group, mostly within Cummings, Lloydminster, Rex and Sparky Formations. The

distribution of coals in the basin is influenced by the tectonic events that created the foredeep, with the rank of the coals decreasing toward the craton, indicating that coalification was a pre-tectonic event (Smith, 1989). The deposition of coal seams is interpreted as an indication that the area emerged after the deposition of the sand, and this would have provided the necessary conditions for the erosive activity of a network of streams to take place (Gross, 1980). These coal deposits are not currently utilized because of high extraction costs associated with their relatively deep burial. However, the prospect of exploitation by in situ gasification remains, and these deposits are therefore a resource for the future (Christopher, 2003).

2.3. LOG CORRECTIONS

Uncertainties in recorded logs can be due to the effects of borehole wall rugosity and mud filtrate invasion. Velocity dispersion and shale alteration also can play an important role (Vasquez et al., 2004). These effects should be removed from the logs to assist in a good well-to-seismic correlation, leading to accurate estimations of rock properties from the seismic data. In the following section several log corrections are performed to remove effects from bad borehole conditions and mud filtrate invasion.

Borehole rugosity affects logging tools in various ways, with density tools being the most affected, as they are held against the side of the borehole wall during logging, and also due to gamma ray scattering at the irregularities of the surface. Generally, the density correction curve (DRHO) indicates how much correction has been added during processing due to borehole effects, and the bulk density curve should be considered suspect whenever the correction exceeds 0.20 g/cm^3 (Asquith and Krygowski, 2004).

Compensation methods used in sonic tools reduce the effects of borehole rugosity, as the signals from different transmitter-receiver pairs are averaged over the same length of the borehole. However, sonic logs still suffer from problems due to cycle skipping and noise spikes, among others. Cycle skipping occurs when the first arrival is too weak to be detected, due to attenuation of the signal caused by fractures or gas zones, resulting in a longer travel time for the formation (i.e. lower velocity). Noise spikes occur when noise around the wellbore triggers the receivers prior to the arrival of the actual signal, resulting in a shorter travel time for the formation (i.e. higher velocity).

In the wells evaluated in this project, borehole rugosity does not seem to be a significant issue. Figure 2.4 shows the GR, caliper, and the raw and edited P-wave velocity and density logs for a shallow depth interval in well C07-16. The caliper log does not indicate any badly washed out areas, showing only small variations of about ± 2 cm from the bit size. In most cases, the location of the spikes correlates between the density and velocity logs, but there is not an obvious correlation to the washed out sections in the caliper log. The spikes also occur within a section of very uniform GR reading, suggesting that they are not related to an actual lithology variation in the section. The spikes in the density log represent a variation of approximately 10 % with respect to the average log value; however, they are a more significant issue in the sonic log, where they can amount up to a 50 % increase in the velocities. Generally, these spikes can be removed using median filters; however, in this particular case the number of points in the filter required to remove the spikes was too high and the filtered log was too smooth, so manual editing was used instead.

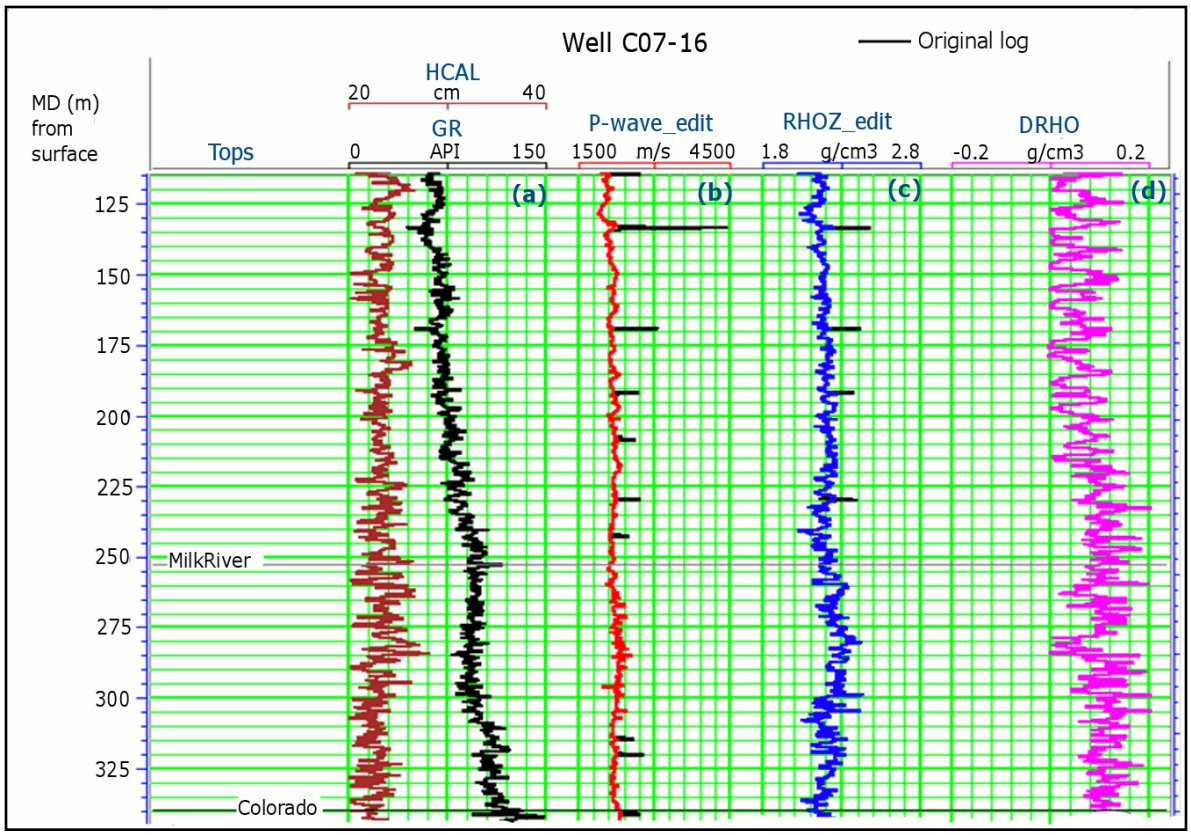

Figure 2.4: Original (black) and edited sonic (red) and density (blue) logs after manual removal of noise spikes in the shallow section of well C07-16. Track 1 shows GR and calliper, track 2 shows the P-wave velocity, track 3 shows density, and track 4 shows the density correction log.

2.3.1. Invasion correction

Mud filtrate invasion occurs when the drilling mud penetrates into the formation, displacing the original fluids, due to the higher pressure of the mud with respect to the pore pressure of the formation. The region closest to the borehole, where all fluids have been displaced by the mud filtrate is referred to as the flushed zone. As this occurs, solid particles of the mud are deposited on the borehole wall forming a mudcake, which reduces the rate of further mud filtrate invasion. Farther away from the borehole, we encounter the transition or invaded zone, where there is a transition from mud filtrate saturation to original formation water saturation, and finally we encounter the undisturbed formation in

what is referred to as the virgin or non-invaded zone (Schlumberger, 1989). Figure 2.5 shows this idealized model of the conditions surrounding the borehole after the invasion process. The extent of the flushed and invaded zones depends on characteristics of the drilling mud, formation porosity and permeability, pressure differential, and the time since the formation was drilled (Schlumberger, 1989).

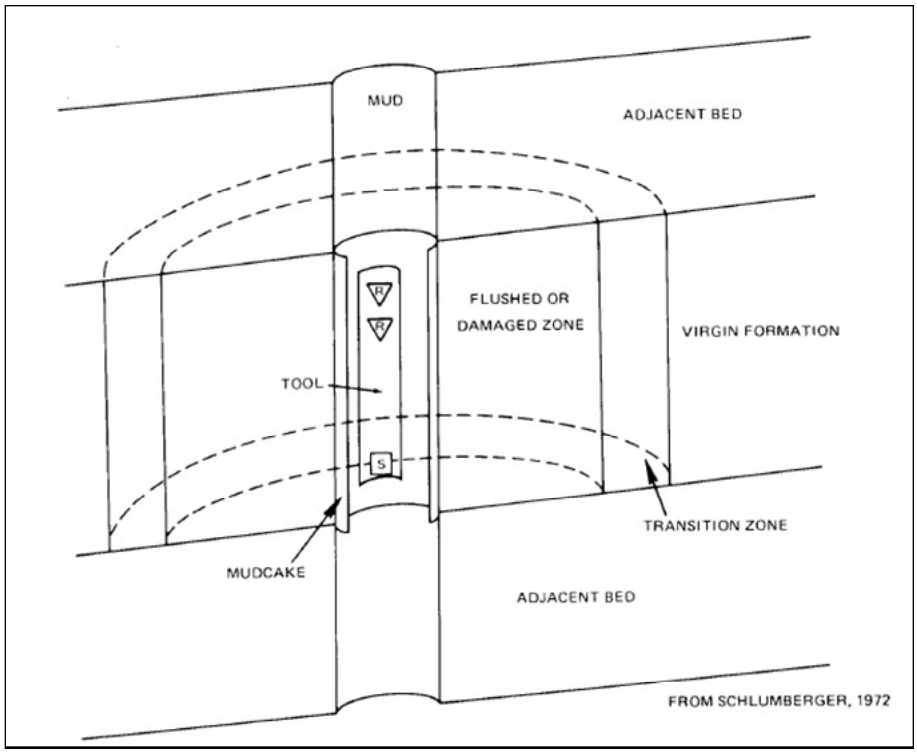

Figure 2.5:Cross-section of an open borehole showing an idealized model for the invasion process (From: Schlumberger, 1972).

Shallower probing tools such as the sonic and density are usually the most affected by mud filtrate invasion, since they only probe a few inches into the formation. Changes in density due to invasion of mud filtrate can be larger than those in velocity, especially in gas zones, where a light gas is being replaced by a heavier liquid filtrate. Considering bulk density as a simple arithmetic sum of the component densities, replacing gas with brine in a 30% porosity rock can increase bulk density by more than 10% (Han and Batzle, 1997).

An important factor to consider when correcting for invasion is the variation in the depth of investigation of the different tools. The depth of investigation for sonic tools is affected by formation type, P- a S-wave velocity, spacing between transmitters and receivers, source frequency, wavelength and wave mode considered, and the type of signal, among others (Chi et al., 2004). In general, the depth of investigation will be approximately one wavelength, which means that a dipole sonic tool can investigate 3 to 4 times deeper than a monopole tool, due to the lower frequency source used. The suite of logs from the Manitou Lake area was acquired using Schlumberger's Platform Express system, and the depth of investigation of the different components varies significantly. The density tool has a depth of investigation of about 13 cm, the neutron porosity tool approximately 23 cm, depending on the hydrogen index of the formation, and the Gamma Ray investigates up to 61 cm into the formation. The three resistivity curves available for these wells (RXOZ, AHF30 and AHF60) investigate about 46, 76 and 152 cm, respectively. The DSI tool, which measures compressional and shear wave sonic, has a depth of investigation of 23 cm, while the borehole compensated sonic (BHS) only investigates up to 8 cm into the formation, due to the higher frequencies used in this tool.

A common approach to correct acoustic logs from mud filtrate invasion effects uses Biot-Gassmann fluid substitution models, where it is assumed that the acoustic logs measure properties of the invaded zone, which is fully saturated with mud filtrate. In order to apply the fluid substitution models, the water saturation of the invaded and the virgin zones must be calculated first, using the shallow and deep resistivity readings, respectively.

The water saturation calculations were done following Archie's methodology. Archie (1942) experimentally determined a relationship for the water saturation of a clean formation in terms of its true resistivity, defined as:

$$S_w = \left(\frac{a \times R_w}{R_t \times \phi^{\mathrm{m}}}\right)^{1/n}, \quad (2.1)$$

where a is the tortuosity factor, m is the cementation exponent, n is the saturation exponent, R_w is the resistivity of the formation water, ϕ is the porosity and R_t is the true formation resistivity. The cementation exponent (m) and the tortuosity factor (a) are determined empirically; however, accepted values for sands are 2.15 and 0.62, respectively. The saturation exponent (n) is generally assumed to be equal to 2.

Equation 2.1 was then used to calculate the water saturation of both the virgin and the flushed zone, in which case the formation water resistivity (R_w) is substituted by the mud filtrate resistivity (R_{mf}), and the true formation resistivity (R_t) by the flushed zone resistivity (R_{xo}). R_t and R_{xo} are assumed to be represented by the deep (AHF60) and shallow (RXOZ) resistivity readings, respectively.

To calculate the formation water resistivity we used the R_0 method (Crain, 1986), which can be used when an obvious clean water zone is present (See Appendix A for more details). The R_w value estimated in the Lloydminster water zone in well A11-17 was 0.12, while R_w at the Colony water zone in well C07-16 was 0.15. These values correlate with those of other Mannville intervals in nearby wells from the R_w Catalog of the Canadian Well Logging Society (2002).

The mud filtrate resistivity at bottom hole temperature (R_{mf}@BHT) can generally be found in the LAS header for the well, and should be corrected to reservoir temperature, if necessary, to obtain the value for R_{mf} in equation 2.1. In this case, the resistivity of mud filtrate at bottom hole temperature (BHT) is 1.280 ohm-m for well A11-17, and 2.455 ohm-m for well C07-16. The LAS header for well A11-17 indicates that the BHT was 22 °C, while at well C07-16 it was 23 °C. The temperature log for each well shows that the

temperature at the reservoir interval is only a degree higher than BHT, suggesting no corrections for temperature had to be applied to the mud filtrate resistivity. Table 2.1 summarizes the parameters used for Archie's water saturation calculation in wells A11-17 and C07-16.

Table 2.1: Parameters used in the calculation of water saturation of the flushed and virgin zones in wells A11-17 and C07-16.

Well	**a**	**m**	**n**	**R_w@FT (ohm-m)**	**R_{mf}@FT (ohm-m)**
A11-17	2.15	0.62	2	0.12	1.28
C07-16	2.15	0.62	2	0.15	2.455

The shallow (RXOZ), medium (AHF30) and deep resistivity (AHF60) logs, calculated water saturation of the invaded (S_{xo}) and the virgin zones (S_w), as well as the temperature log for wells A11-17 and C07-16 are shown in Figures 2.6 and 2.7. Note that the medium and deep resistivities practically overlap each other over the complete interval, suggesting the invaded area is limited to a shallow depth around the borehole. In the shaly section above the Mannville interval the shallow resistivity overlaps the deep resistivity, indicating no invasion is occurring in this interval, probably due to the lack of permeability and very low effective porosities seen in these shales. The more significant invasion effects, evidenced by the separation of the deep and shallow resistivity logs, occur in the water saturated intervals within the Mannville group.

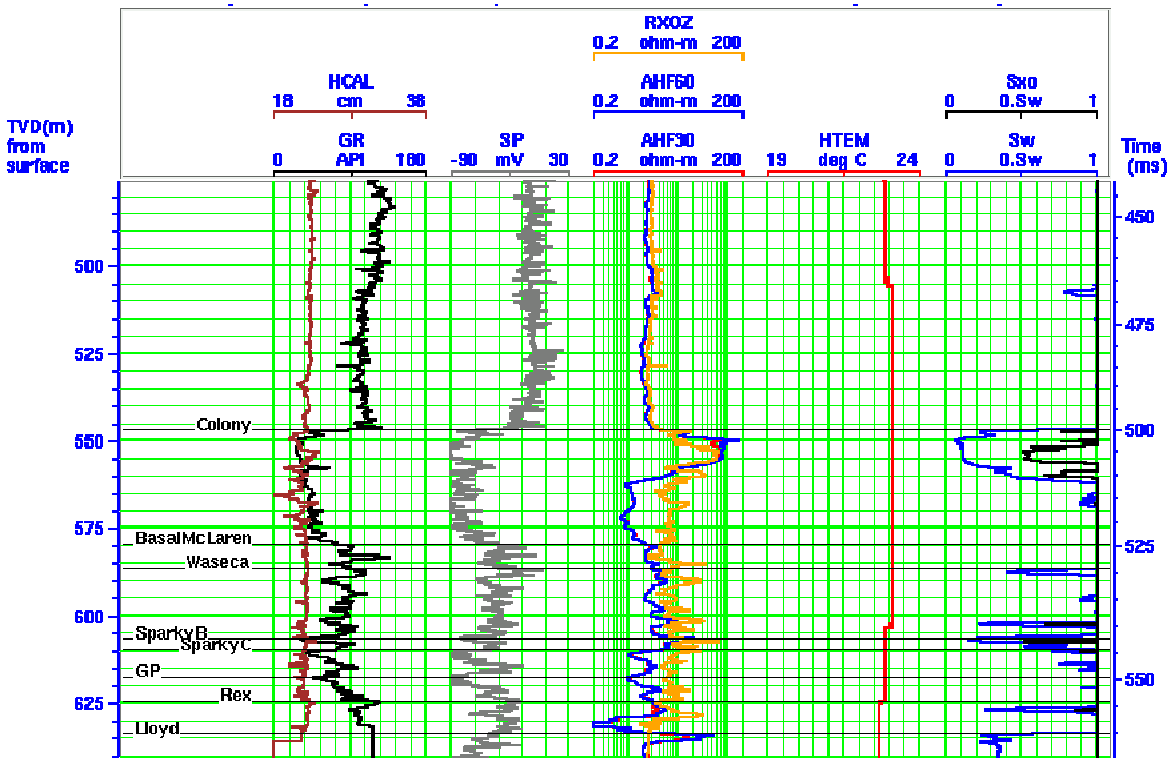

Figure 2.6: Water saturation of the flushed (Sxo) and uninvaded (Sw) zones for well C07-16.

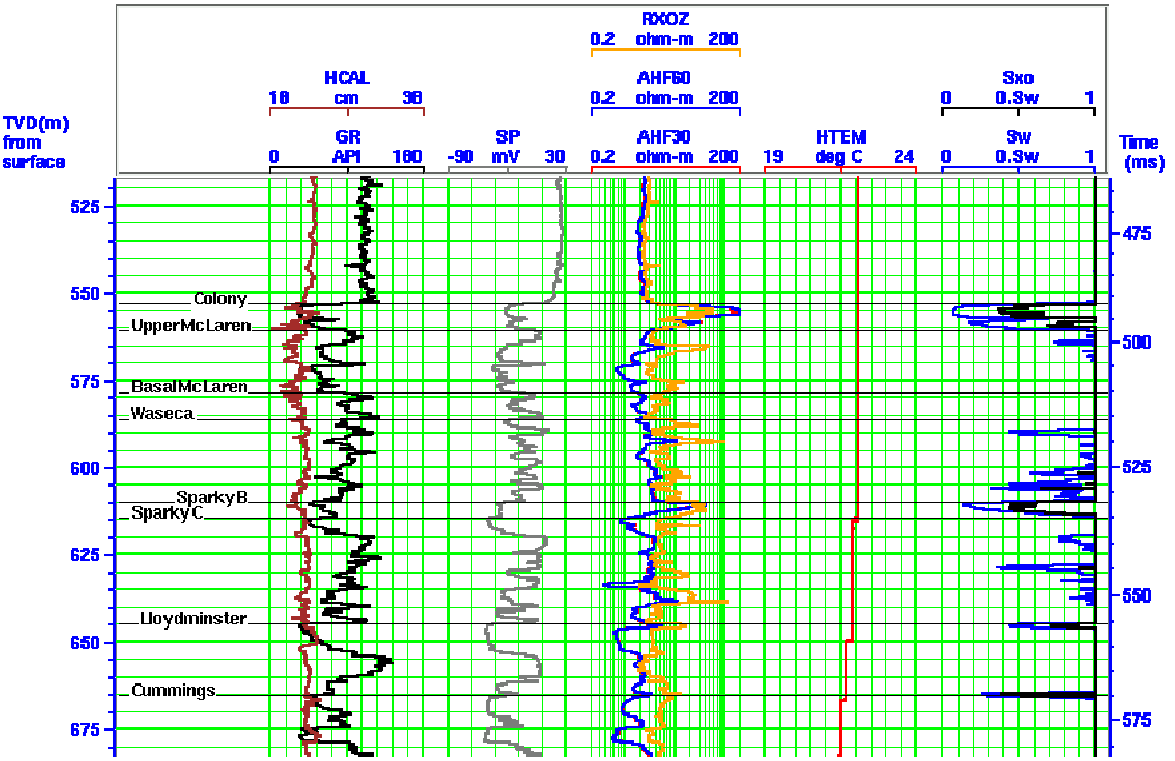

Figure 2.7: Water saturation of the flushed (Sxo) and uninvaded (Sw) zones for well A11-17.

Three fluid phases are interpreted in the Colony channel in well C07-16, with the top 5 m of the sand being gas saturated, the following 10 m saturated with heavy oil and the remaining 20 m saturated by brine. This interval is a good example of the variations in the invasion process depending on the original fluid in the rock. Within the gas interval, the water saturation changes from 0.20 in the virgin zone (Sw) to 1 in the flushed zone, suggesting most of the gas was flushed from the rock closest to the borehole. However, in the oil saturated section, the water saturation changes from 0.1 in the virgin zone to 0.55 in the flushed zone, suggesting that there is a residual hydrocarbon saturation of almost 0.5.

This difference in invasion between the gas and oil saturated zones is probably exaggerated by the high density and viscosity of the heavy oil saturating the rock, which is difficult to displace without any thermal stimulation. Results from well A11-17 are consistent with those seen in C07-16, with water saturation changing from 0.15 in the virgin zone to 0.45 in the flushed zone of the Colony and Sparky intervals.

Biot-Gassmann fluid substitution was performed within the reservoir intervals to reflect virgin zone properties. The V_p, V_s, S_{xo} and density logs are used as input assuming they reflect the conditions of the flushed zone, with an output water saturation equal to S_w. Batzle-Wang's formulation is used to calculate the properties of the saturating fluids using the parameters shown in Table 2.2. Temperature values were obtained from the temperature log, oil gravity was defined based on oil production in nearby well. Table 2.3 shows the calculated density and modulus for each fluid type to be used in Gassmann's fluid substitution, and the calculated pore fluid property for specific oil and gas saturations.

Table 2.2: Parameters used in Batzle-Wang's formulation for the estimation of fluid properties.

Property	**Well A11-17 (Oil/Brine)**	**Well C07-16 (Gas/Brine)**
Pressure	8 MPa	8 MPa
Gas gravity	0.6	0.6
Temperature	22 ℃	22 ℃
Oil gravity	12 API	12 API
Gas-oil ratio	0	100
Salinity	10000 ppm	10000 ppm

Table 2.3: Calculated properties for the different saturating fluids using Batzle-Wang's formulation and the parameters in Table 2.2.

Property	**Oil**	**Gas**	**Brine**	**Pore fluid (Sw=0.66, Oil)**	**Pore fluid (Sw=0.55, Gas)**
Calc. density (g/cm3)	0.9882	0.0581	1.006	1.0004	0.5763
Calc. modulus(GPa)	2.498	0.011	2.2922	2.3577	0.0243

The low gravity (high density) of the heavy oil in the area results in elastic properties very similar to those of the brine, which explains why there is little change in V_p and density after the fluid substitution in the oil saturated zones (Figure 2.8). However, fluid substitution in the gas saturated intervals of well C07-16 results in both P-wave velocity and density decreasing by 10-20 % (Figure 2.9). In both cases, S-wave velocity remains the same as it is assumed to be independent of pore-fluid content.

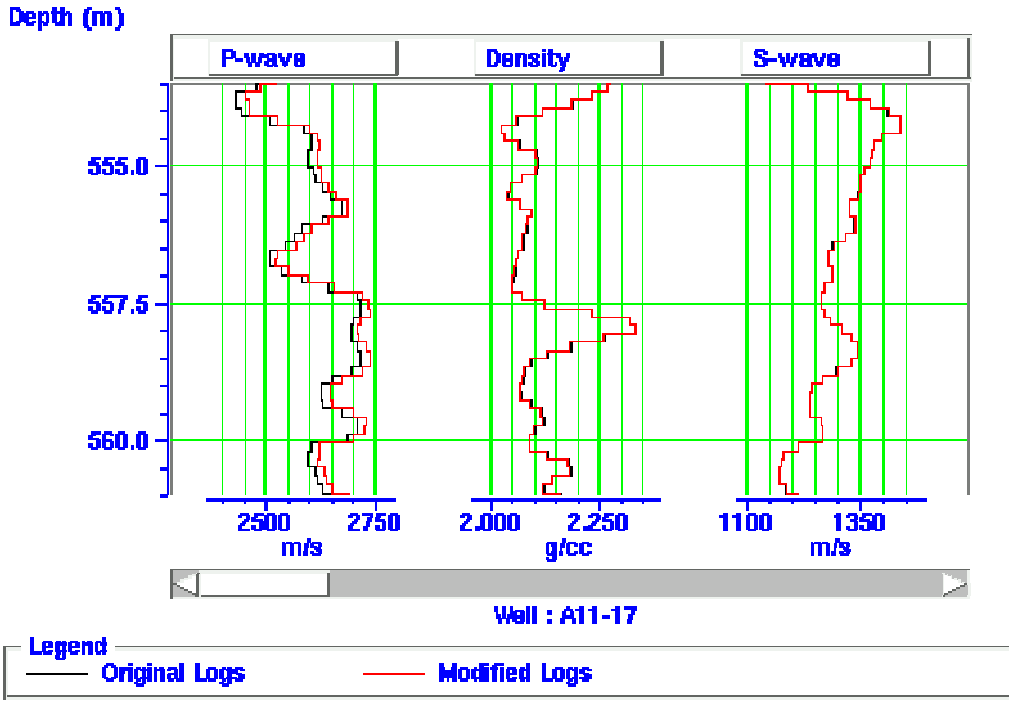

Figure 2.8: Fluid replacement modelling in the oil saturated Colony interval in well A11-17. Black curve shows input logs, and red curves shows the modified logs after the fluid substitution.

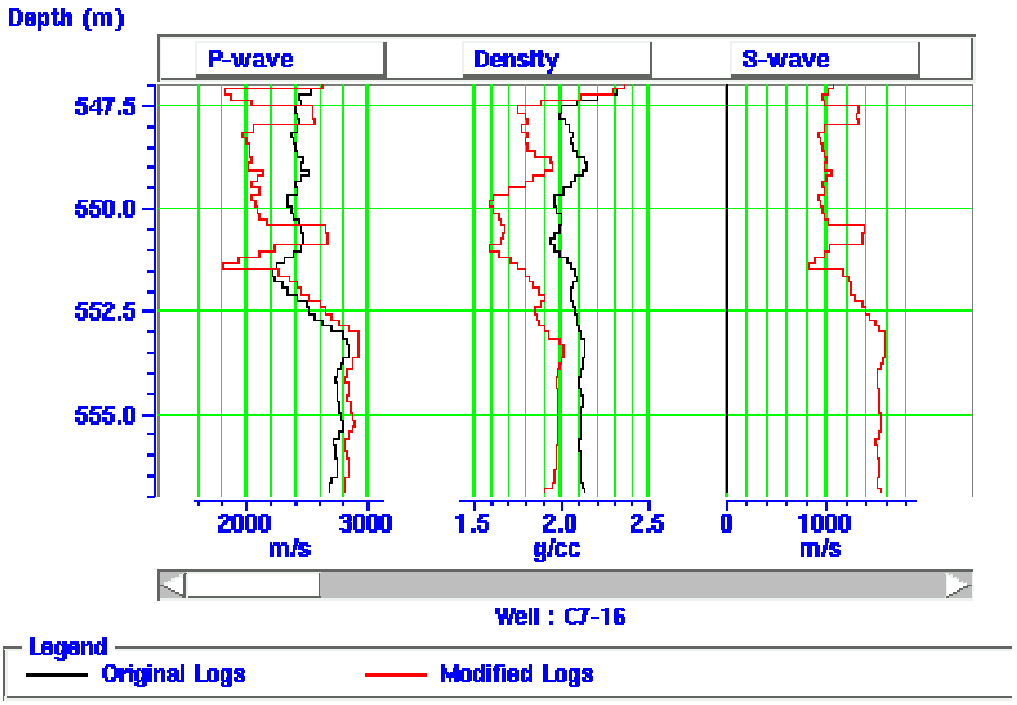

Figure 2.9: Fluid replacement modelling in the gas saturated Colony interval in well C07-16. Black curve shows input logs, and red curves shows the modified logs after the fluid substitution.

2.4. ELASTIC PROPERTIES

Logs from the two wells analysed in the area show a sharp decrease in the GR and SP logs at the top of the Colony sands, indicating the change from the shales of the Colorado Group to the predominantly sandy Mannville Group (Figures 2.10 and 2.11). At this interface the density log decreases, the P-wave shows almost no change and the S-wave velocity shows a very significant increase from 800 m/s in the shales to 1300 m/s in the sands. High resistivity values (from 5 to 200 ohm-m) in the Colony and Sparky members indicate hydrocarbons, while the cross-over between the density and neutron porosity logs in the Colony sands suggests the presence of a gas cap. Several coal beds can be interpreted in the area, based on the lower density values, between 1600 and 1700 kg/m^3.

Density and the velocity logs appear to be anticorrelated in some areas, especially at the top of the Mannville, where there is a significant decrease in the density and a slight increase in velocity. In well C07-16, there is a slight decrease in P-wave velocity at the Colony top, which appears to be related to the gas saturation in the upper part of the channel, since it correlates to the cross-over between the neutron and density porosities.

The petrophysical interpretation of logs from the three wells available showed that the Colony sand member has an average net thickness of 20 m, effective porosity on the order of 40% and very high permeabilities in the order of 5-10 D (See Appendix A). Core data for the Colony member was not available in the surrounding wells; however, core data for the Sparky interval in a nearby well shows results that are consistent with those obtained in the log analysis.

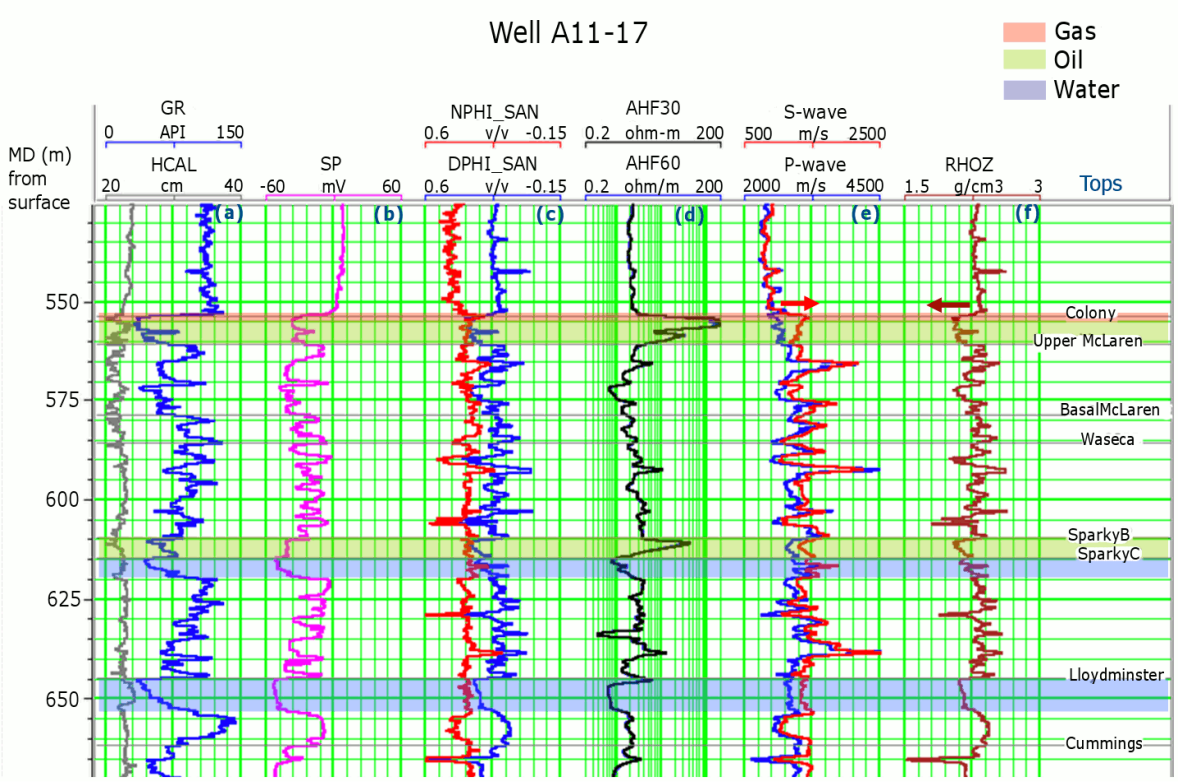

Figure 2.10: Detail of the suite of logs at the reservoir interval in well A11-17. Gas is indicated by red highlight, oil by green and water by blue.

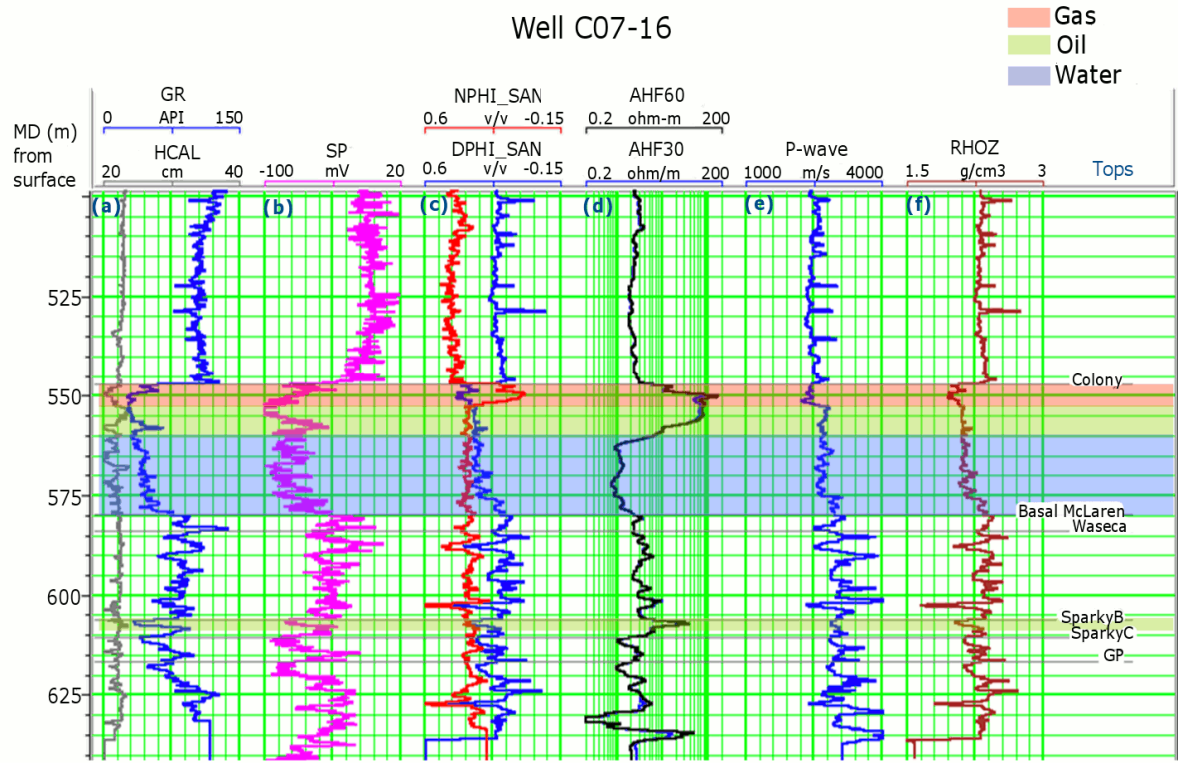

Figure 2.11: Detail of the suite of logs at the reservoir interval in well C07-16. Gas is indicated by red highlight, oil by green and water by blue.

2.4.1. Crossplots

Crossplots of the elastic properties based on the log measurements for each well were evaluated to better define the relationship between elastic parameters and rock properties, such as lithology and saturation (Figures 2.12). The GR log was used as a proxy for lithology, with low GR measurements defined as sand intervals, and high GR values defined as shales. Over the complete depth interval density is not a good lithological indicator, as density values overlap for sands and shales, in a range between 2000 and 2400 kg/m^3. Intervals with densities lower than 2000 kg/m3 were interpreted as coals, which are present in various Mannville intervals. P-wave velocity also shows overlap between the sands and shales, with shales having a generally lower velocity than the sands. On the other hand, S-wave velocity shows very little overlap between sands and shales, which appear to have S-wave velocities lower than 1200 m/s. This anomalous S-wave response at the top of the sands makes Vs and the Vp/Vs ratio the best lithological indicators, with sands having a ratio between 1.7 and 2.2, and shalier intervals ranging between 2.4 and 4.

Within the target zone (400 to 600 m depth) density is also a good lithological indicator, with densities lower than 2220 kg/m^3 indicating sands, and higher values corresponding to shaly sands and shales (See Figure 2.13b). Note how P-wave velocity values overlap for sands and shales within the target interval.

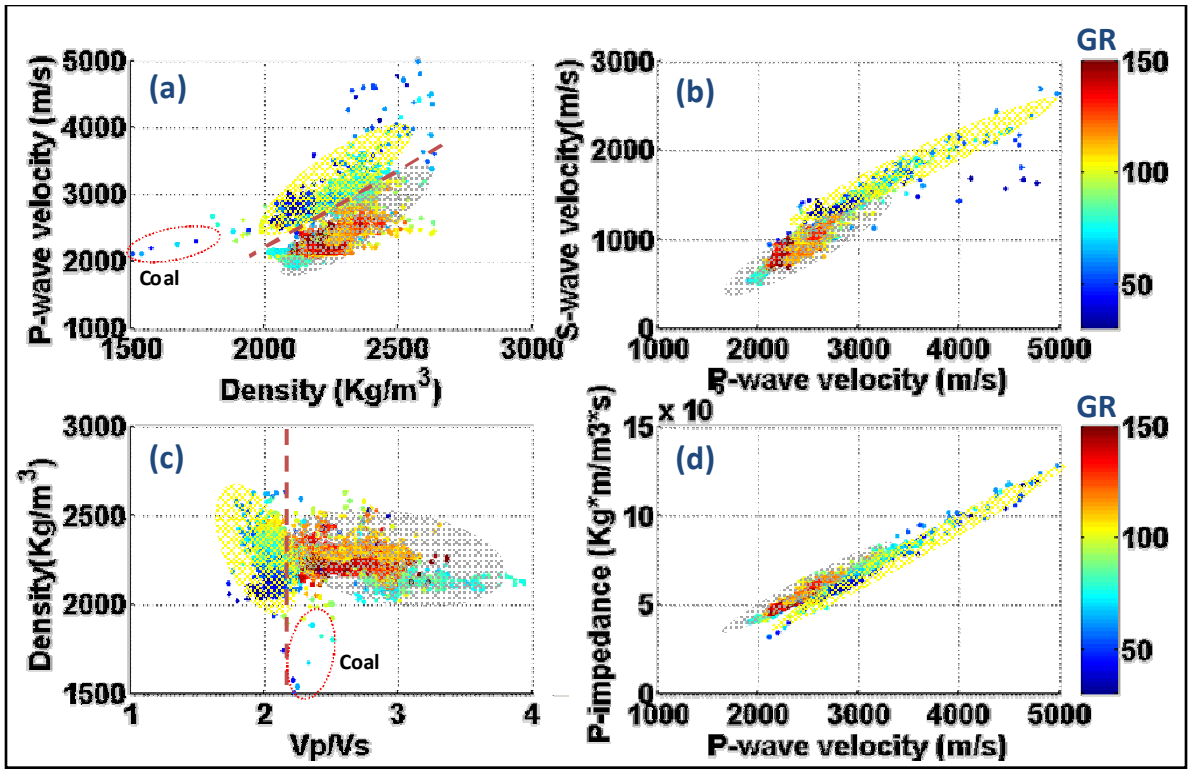

Figure 2.12: Crossplots for well A11-17. (a) P-wave velocity versus density, (b) S-wave velocity versus P-wave velocity, (c) density versus Vp/Vs, and (d) P-impedance versus P-wave velocity. Color bar indicates gamma ray values in API units. Areas with low GR highlighted by yellow ellipses.

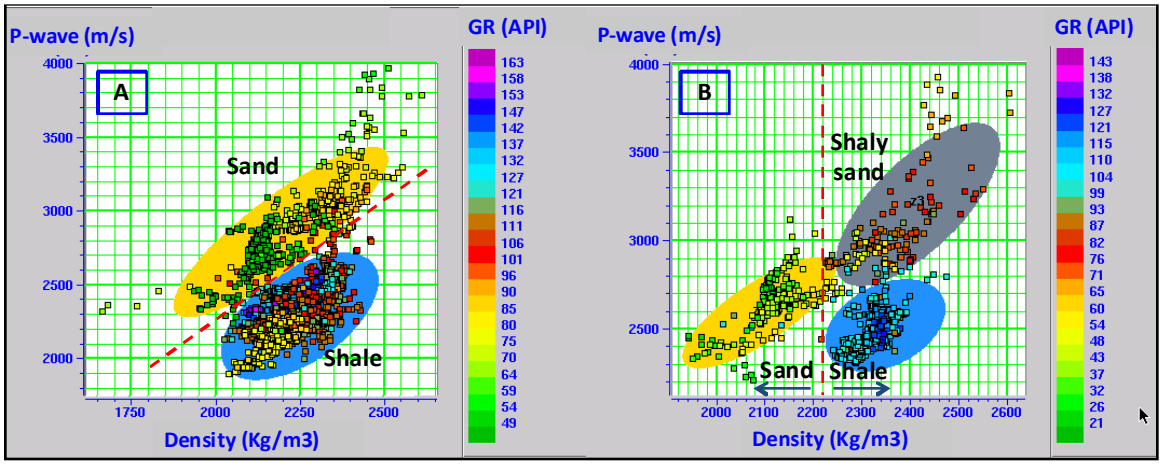

Figure 2.13: P-wave velocity versus density crossplot for well C07-16 (a) over the complete depth interval, and (b) for the interval between 500 and 600 m. Note that there appears to be a separation between sand and shaly sand at 2220 Kg/m^3.

The effect of pore fluid is evaluated using crossplots where only samples from clean sands (GR < 50 API units) and with porosities higher than 30 % were considered (Figure 2.14). The saturating fluid was determined based on the resistivity log, defining a water zone as having resistivities lower than 5 ohm-m and hydrocarbon zones as having resistivities higher than 5 ohm-m. The neutron-density porosity crossover was used to distinguish between oil and gas intervals. The heavy oil in this area has a gravity of approximately 12 API degrees, which is equivalent to a density of 980 kg/m^3 and very close to the density of water, there shouldn't be a big change in density between the oil and water saturated sections. However, when the sands are gas saturated the decrease in density is more significant, and in both well it is possible to note a clear separation between gas and water sands at a density value of 2090 kg/m^3.

2.5. PREDICTING ROCK PROPERTIES FROM WELL LOGS

Bulk density is a simple volumetric average of the rock constituent densities and is closely related to porosity. However, velocity can bear a complicated relationship to porosity, pore fill and density, since cracks and crack-like flaws and grain boundaries, which may have very low porosity, can substantially decrease V_p and V_s (Mavko et al., 1998). Laboratory measurements can be useful to estimate systematic variations of velocity and density, but they do not provide direct control for surface seismic data, due to sampling, scale and frequency considerations (Castagna et al., 1993).

Different empirical relationships exist between the different elastic properties for common sedimentary rocks, including the mudrocck line between P- and S-wave velocities (Castagna et al., 1985), Gardner's relation between density and P-wave velocity (Gardner et al., 1974), and Lindseth's relation between impedance and P-wave velocity (Lindseth,

1969), among others. These relationships often work for pure lithologies; however, many real rocks contain mixed lithologies, making it necessary to average the properties or relationships for pure rock types.

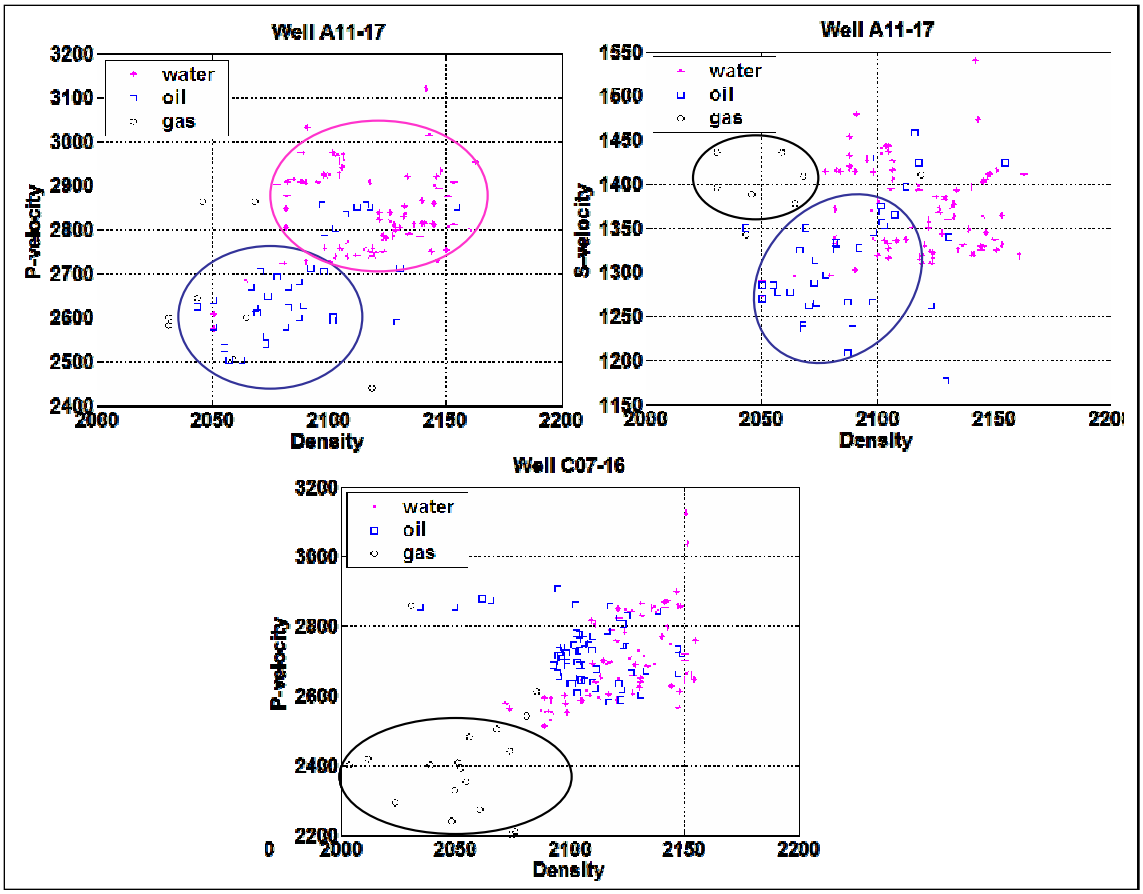

Figure 2.14: Density, P-wave and S-wave velocity variations with saturating fluid based on log samples. Black circles correspond to gas, blue squares to oil and magenta stars to water.

2.5.1. Gardner's relation

Gardner et al. (1974) found an empirical relationship between density and velocity from a series of controlled field and laboratory measurements of brine-saturated rocks, excluding evaporites, from various locations and depths, given by:

$$\rho = aV^m, \tag{2.2}$$

where ρ is density and V is P-wave velocity. Default values for a and m are 0.31 and 0.25, respectively, for density in g/cm^3 and P-wave velocity in m/s. Gardner's relation can be good approximation for shales, sandstones and carbonates, while coals and evaporites depart significantly from the expected behavior.

Taking the logarithm of both sides of equation 2.2 gives a linear relationship between $\log(\rho)$ and $\log(V)$, making it possible to use a linear regression to find the coefficients a and m that best fit the data in a least squares sense, according to the following equation:

$$\log(\rho) = \log(a) + m\log(V)\,. \tag{2.3}$$

Figure 2.15a shows the plot of $\log(\rho)$ vs $\log(V)$ for well A11-17, showing the least-squares fit to equation 2.3. Velocities are in m/s and density is in g/cm^3. Note that the points appear to be differentiated into two clusters, with differentiated GR values. A single fit for all points results in values of a equal to 0.927 and m equal to 0.11; which are significantly different from Gardner's default parameters. There is also considerable scatter of the points from the straight line.

Castagna et al. (1993) suggest using values of a and m specific to each rock type (See Table 2.4). The stratigraphic column shows that shale is the dominant lithology above the top of the Mannville, except for a few interbedded sandstones, while sediments within the Mannville Group are predominantly sands. The Gamma Ray log supports this lithological separation, showing a sharp decrease correlated to the Mannville top. Based on this, the GR was used as a lithology discriminator to estimate values of a and m for specific rock types. Samples with GR values below 70 API units were considered sands, and higher values assigned to shales. Using this constraint, equation 2.3 was refitted to account for

each rock type, resulting in *a* values of 0.225 and 0.516 for sand and shale respectively, and *m* values of 0.28 and 0.19 for sands and shales, respectively.

Table 2.4: Coefficients for the Gardner et al. (1974) velocity-density relationship for specific lithologies (Castagna et al., 1993).

Lithology	A	M	Vp range (km/s)
Shale	1.75	0.265	1.5-5
Sandstone	1.66	0.261	1.5-6
Limestone	1.5	0.225	3.5-6.4
Dolomite	1.74	0.252	4.5-7.1
Anhydrite	2.19	0.160	4.6-7.4

Figure 2.15b shows the density vs P-wave velocity graph with the sand and shale discrimination based on the GR log. Note that the two clusters are now clearly differentiated and there is considerably less scatter of points with respect to the fitted line. Comparing the values fitted to the Manitou Lake data and those suggested by Castagna et al., (1993) for sand and shale, we can see there are significant differences between the two, highlighting the importance of using local parameters that fit the data, instead of using default parameters.

A density log was estimated from the P-wave sonic log using Gardner's default parameters (Figure 2.16a), the parameters from a single fit (Figure 2.16b) and the parameters from the sand and shale separation (Figure 2.16c). Using Gardner's default parameters gives a very poor fit in the shale section of the log, but improves significantly within the Mannville interval; however, the behavior of the log at the top of the Mannville is opposite to that observed in the measured density log, showing an increase in the density instead of a sharp decrease. The parameters estimated from a single fit result in a much averaged density log, showing only very small fluctuations. The best density log is obtained using specific parameters for the two predominant rock types, especially within the

Mannville interval, adequately modelling the sharp decrease in density at the Colony top as well as other smaller fluctuation within this interval.

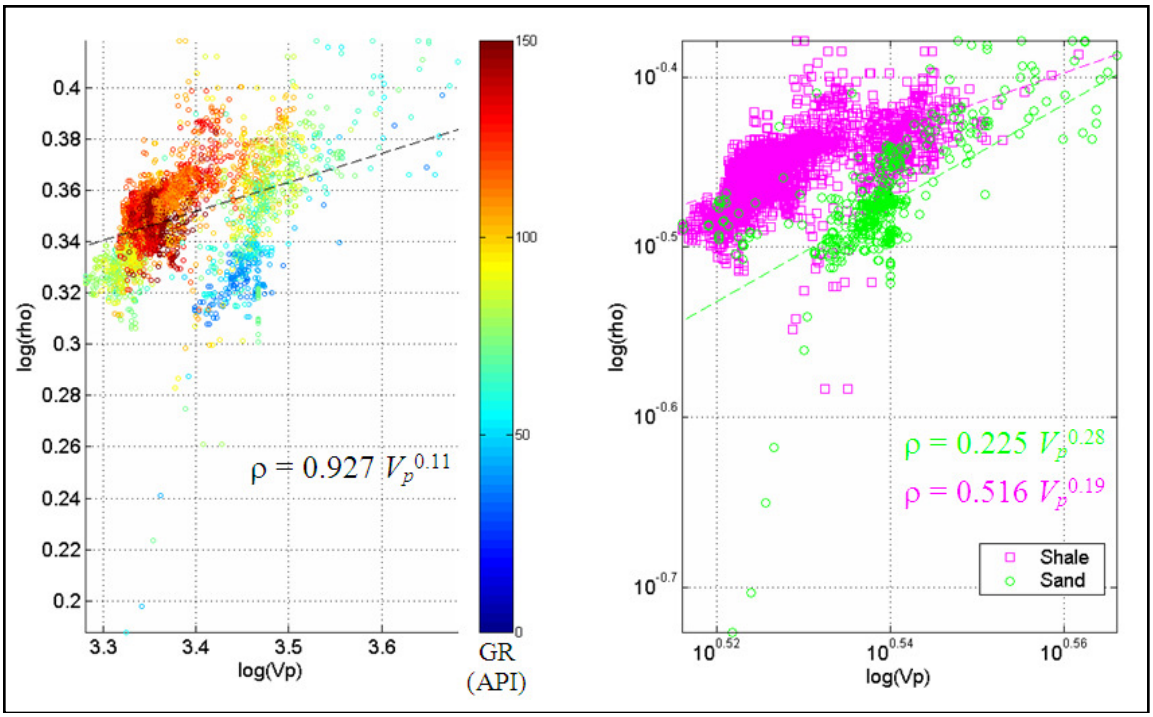

Figure 2.15: (a) Density vs. P-wave crossplot for well A11-17 showing best fit line for Gardner's equation. Colorbar indicates GR values. (b) Sand and shale separation based on a GR cutoff of 70 API units. Magenta points indicate samples with GR higher than 70 API units, and green point samples with GR lower than 70 API units. Best fit lines for each cluster shown in the respective colors.

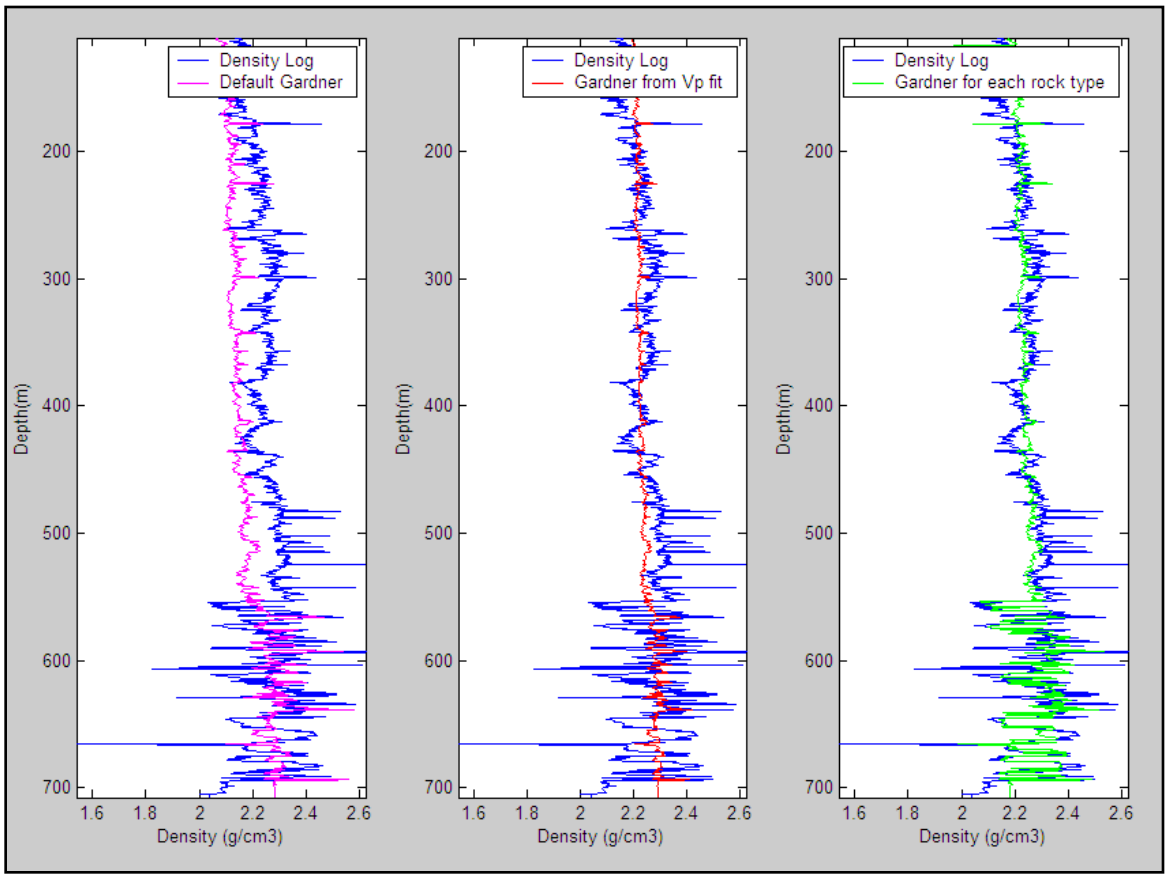

Figure 2.16: Density estimates for well A11-17 using Gardner's equation (a) using default values of *a* and *m*; (b) using single fit for Vp, and (c) using *a* and *m* specific for sand and shale.

2.5.2. Lindseth's relation

Given the linear behavior observed between impedance and velocity, Lindseth's empirical relation was evaluated to estimate density from the sonic log. Lindseth (1979) suggested a linear empirical relation between velocity and impedance, given for velocity in ft/s and ρ in g/cm^3 by:

$$V = 0.308\,\rho V + 3460\ . \tag{2.4}$$

When considering velocity in m/s, the coefficients become 0.308 and 1054. Using a least-square linear fit for the equation

$$V = c\rho V + d \tag{2.5},$$

the coefficients c and d that best fit the data are calculated for both wells. Solving for density in equation (2.5) results in:

$$\rho = \frac{V - d}{cV} \tag{2.6}$$

Figure 2.17 shows the results of different fits for equation 2.5, which were subsequently used to calculate density logs, using equation 2.6. Lindseth's default parameters (magenta line) give a very poor approximation of the density log, especially in the shale interval, where the residual is as big as 0.6 g/cm^3. Using the single fit (red line) improves the density estimates; however, it shows the same issues as Gardner's single fit, resulting in a log with very small variations and showing an increase in density at the top of the Mannville. Finally, the best density log is obtained by using different parameters for sands and shales (green line).

Table 2.5 summarizes the results from using Gardner's and Lindseth's relations to estimate density. Note the significant improvement by fitting the data locally instead of using the default parameters, especially when using Lindseth's equation. The best fit is obtained for the shale section in both cases, probably due to the very small fluctuations in density within this interval. Lindseth's equation does a better work at modelling the very low densities associated to the coal seams within the Mannville, as in Gardner's approach the points with very low densities are not within the fitted trend to the data.

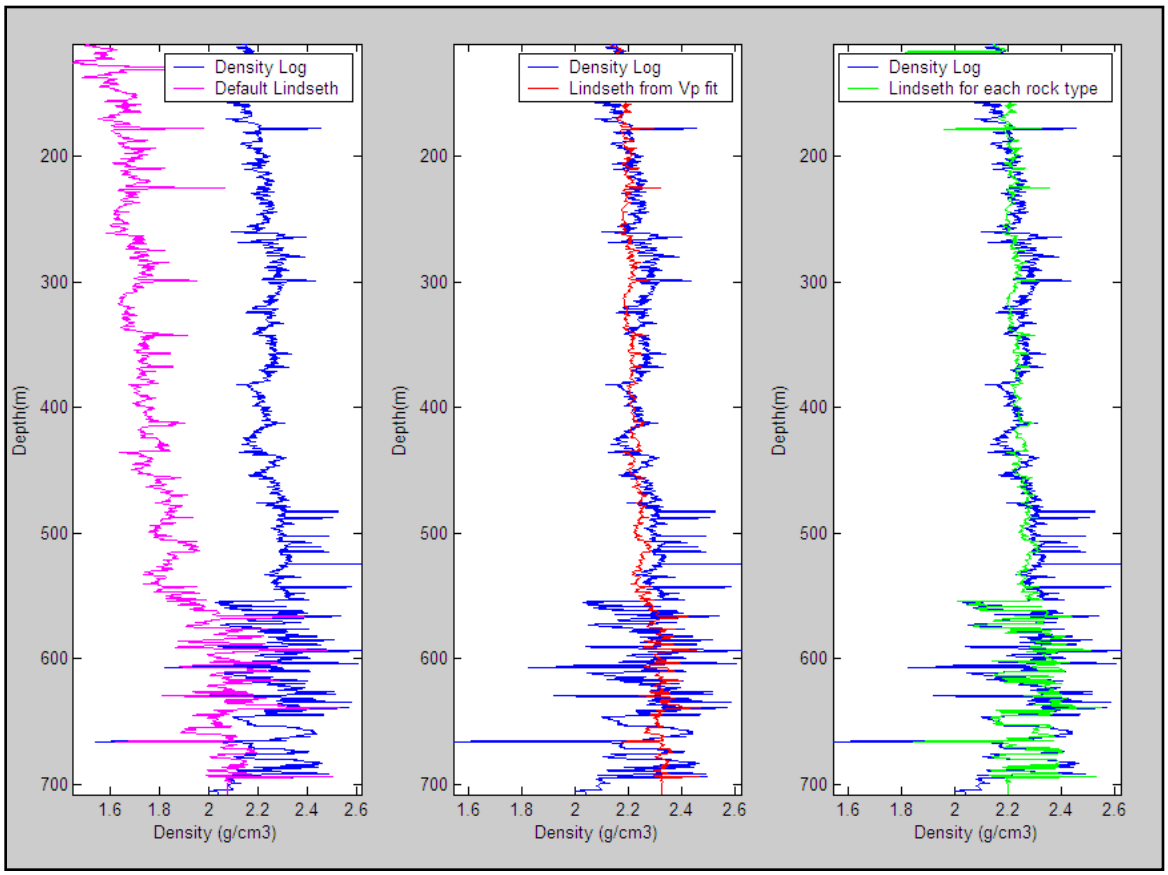

Figure 2.17: Density estimates using Lindseth's linear relation between velocity and impedance for well A11-17 (a) using default parameters; (b) single fit between I_p and V_p, and (c) using different parameter for sand and shale.

Table 2.5: Gardner's and Lindseth's coefficients obtained using different fits to the data, showing RMS value of the density residuals.

Fit	***a***	***m***	**RMS error (g/cm^3)**
Gardner's coefficients	0.310	0.25	0.1147
Gardner's single fit	0.9277	0.1131	0.0848
Gardner's fit for shale	0.5162	0.1896	0.0583
Gardner's fit for sand	0.2249	0.2847	0.0678
Fit	***c***	***d***	**RMS error (g/cm^3)**
Lindseth's coefficients	0.308	1054.06.	0.4550
Lindseth's single fit	0.3702	411.09	0.0879
Lindseth for shale	0.3572	459.25	0.0579
Lindseth for sand	0.3224	855.37	0.0708

The forward modelling done shows that when using density-velocity relations it is necessary to evaluate which equation best fits the data and parameters should be estimated locally, as most of these equations were derived empirically and the coefficients are significantly affected by local geology. Density and velocity can give information about different rock properties, and using these relations results in a loss of information. For example, density can be easily related to the pore fluid density and the porosity, while the velocity is not simply related to the porosity, mostly due to the presence of microcracks, which strongly affect the P- and S-wave velocities (Mavko et al., 1998).

2.5.3. Modelling with the mudrock line

Castagna et al (1985) combined a variety of in situ and laboratory measurements of P- and S-wave velocities for elastic silicate rocks, and concluded that shear-wave velocity is linearly related to compressional-wave velocity for both water-saturated and dry clastic silicate sedimentary rocks by an equation of the form:

$$V_p = 1.16V_s + 1.36, \tag{2.7}$$

where the velocities are in km/s. This relation is generally defined as the mudrock line.

A linear least-square fit of the P- and S-wave velocities logs from Manitou Lake results in a slope of 1.2 and an intercept of 1.257, which are very similar to the parameters defined by Castagna et al. (1985) in equation 2.7. A scatter plot of P- versus S-wave velocity using the logs from well A11-17, with the mudrock line in black, and the least-squares fit in blue, is shown in Figure 2.18. The deviation between the two curves increases with decreasing S-wave velocities, and they start to overlap for velocities higher than 1500 m/s.

The mudrock line and the locally fitted relation between Vp and Vs were used to predict shear-wave velocities in well A11-17. Figure 2.19 shows the original and predicted Vs logs, as well as the residual between the original Vs log and the Vs log predicted from the local fit. The maximum residual values are around ±500 m/s, but they are localized to a few spikes in the log. Note the fit in the shaly section above the Colony top is not very good, with the modelled log overestimating Vs values by approximately 100 m/s. However, the most drastic change in the residual is observed at the top of the Colony sand, where the modelled log is underestimated by as much as 250 m/s.

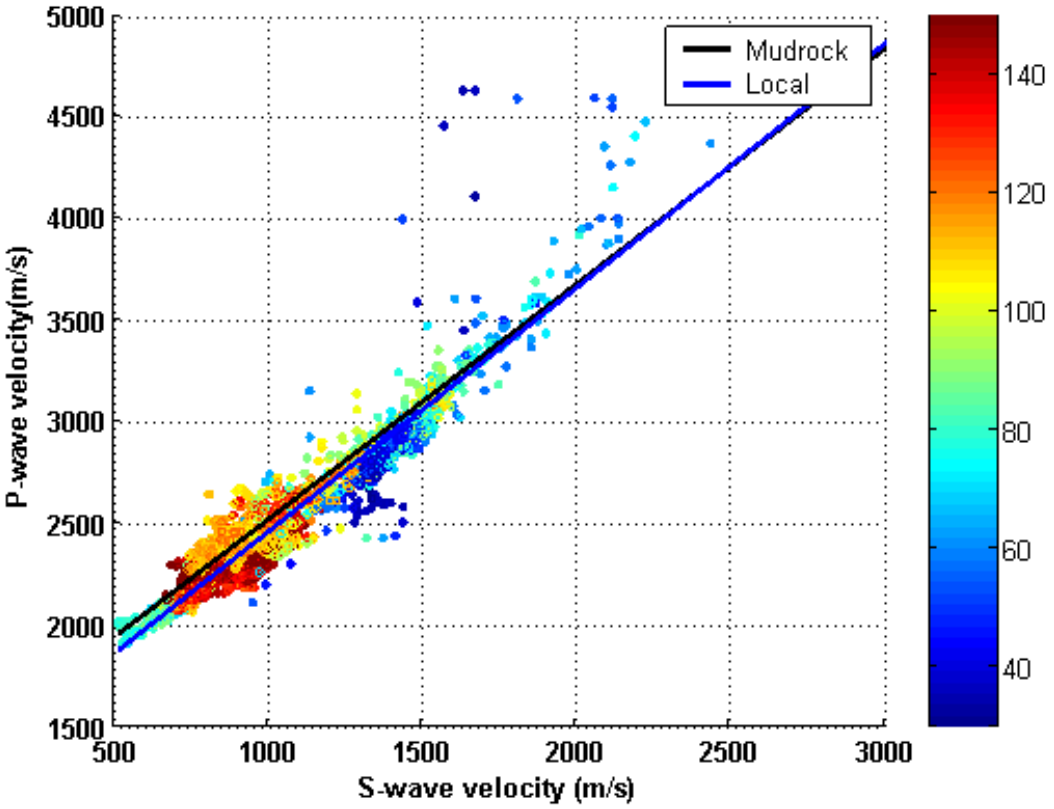

Figure 2.18: P- versus S-wave velocity crossplot for well A11-17. The mudrock and the best fit lines are shown in black and blue, respectively. Colorbar indicates GR values.

A detailed view of the logs within the target zone (Figure 2.20) shows that the difference between the original Vs and the modelled log is positive in regions with higher

sand content, as indicated by the GR log. This suggests that the residual between Vs and the mudrock calculation could be used to identify zones with high sand content, which seem to be associated with anomalously higher S-wave velocities. Analysis of well logs from the Blackfoot field in Southern Alberta have shown the same type of response and differentiation between sands and shales with the Vs residual (See Appendix B).

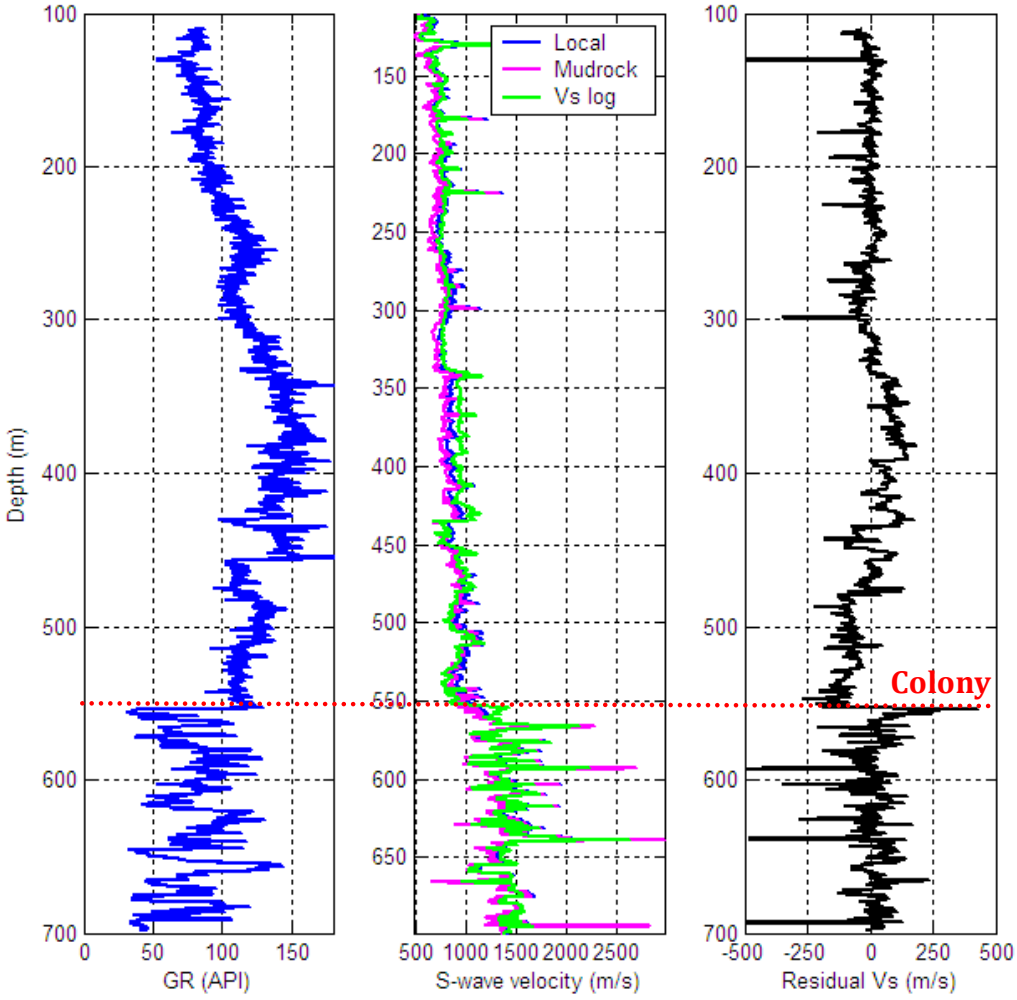

Figure 2.19: (a) GR log, (b) predicted and original Vs logs using the mudrock line and the best fit parameters, and (c) difference between the original Vs log and modelled Vs using the best fit line parameters for well A11-17. Red dotted line indicates the Colony top.

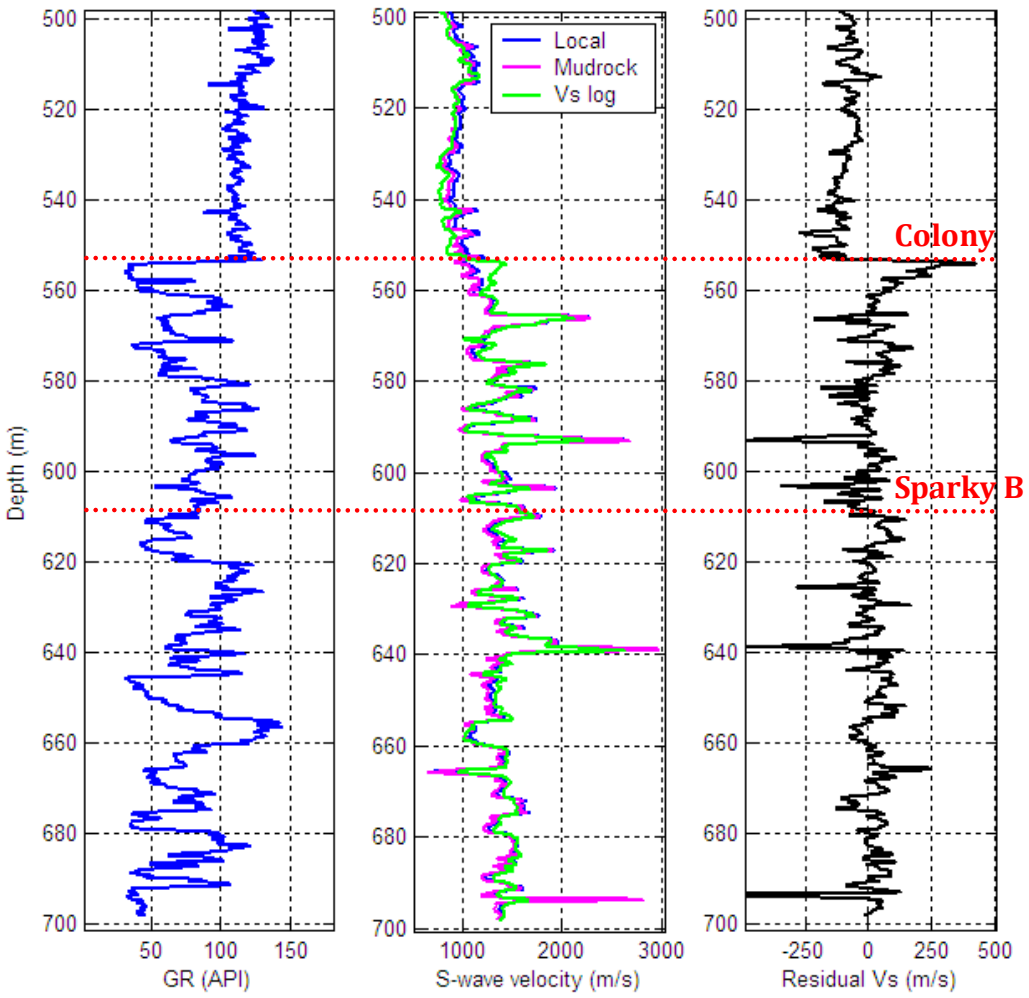

Figure 2.20: Detail of the logs in Figure 2.18. Red dotted lines indicate the Colony and Sparky B tops.

2.5.3. Log response equation

A different modelling approach was considered based on a more specific rock physics model. In this approach the rock is modeled as having four major components that contribute to the log reading (e.g. water, hydrocarbon, shale and matrix). The first term corresponds to the water contribution, the second to the hydrocarbon, the third is shale contribution and the final term is the contribution from the rock matrix (Figure 2.21).

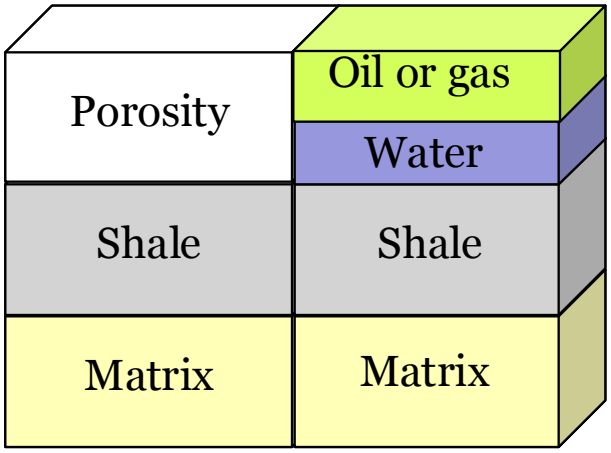

Figure 2.21: Rock physics model for the log response equation.

Density, P-wave sonic and S-wave sonic logs can then be modeled using the following equation (Crain, 1986):

$$l_{reading} = (\phi_e * S_w * l_{water}) + (\phi_e * (1 - S_w) * l_{hydro}) + (V_{sh} * l_{shale}) + ((1 - V_{sh} - \phi_e) * l_{matrix}), \quad (2.7)$$

where ϕ_e is the effective porosity corrected for shale volume, S_w is the water saturation, and l_x is the property value within each component $_x$.

Log values for water, hydrocarbon and matrix were selected from the literature, based on the known lithology and fluid properties (quartz matrix, and 12° API oil ≈ 0.98 g/cm^3). Shale values were selected directly from the logs, as they can have a wide range between different areas. Table 2.6 summarizes the parameters used for each component within the log response modelling approach. Shale volume was calculated from the GR log, effective porosity was calculated from the density-neutron crossplot method and corrected for shale volume, and water saturation was calculated using Archie's formulation (Figure 2.22).

Table 2.6: Parameters used for the log response modelling.

	P-wave sonic (µs/m)	S-wave Sonic (µs/m)	Density (kg/m^3)
Matrix	182	292	2650
Water	616	1200	1000
Shale	500	1450	2200
Oil	664	1200	950

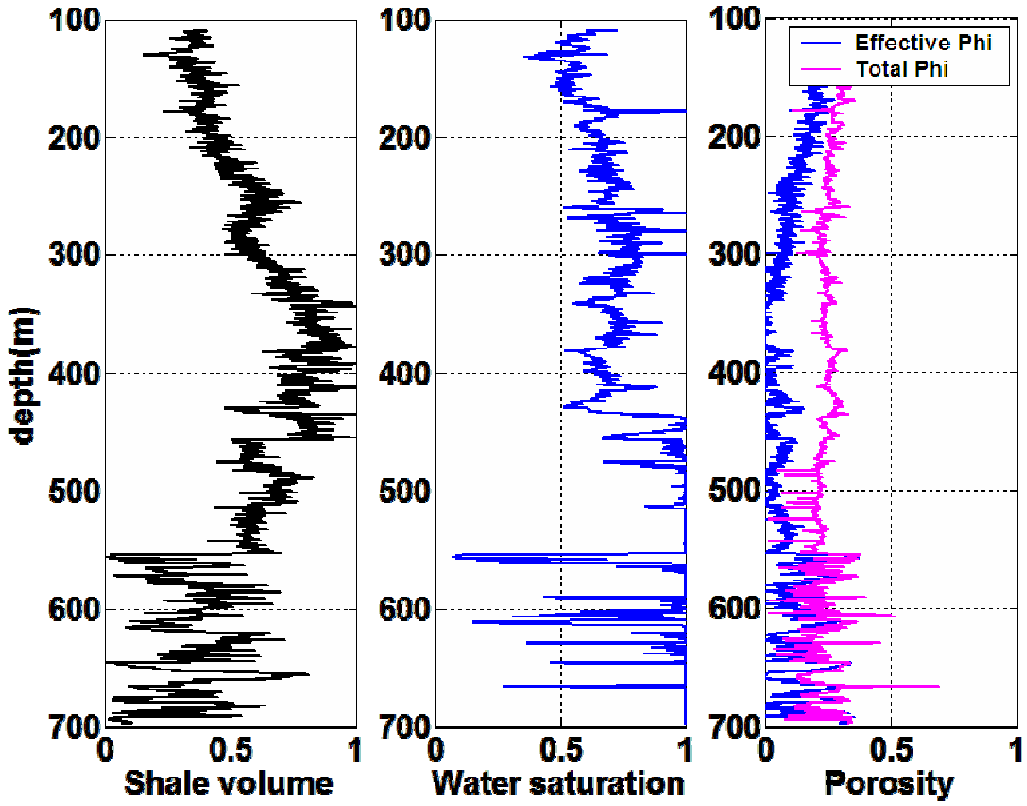

Figure 2.22: Input logs for use in the log response equation (a) shale volume, (b) water saturation, and (c) porosity.

Figure 2.23 shows the modelled V_p, Vs and density logs using the log response equation, while Figure 2.24 shows a detail of the modeled logs within the interval of interest. Note that modeled V_p and density logs fit very well with the original data, while the V_s estimates deviate more from the original log, especially within the shalier section.

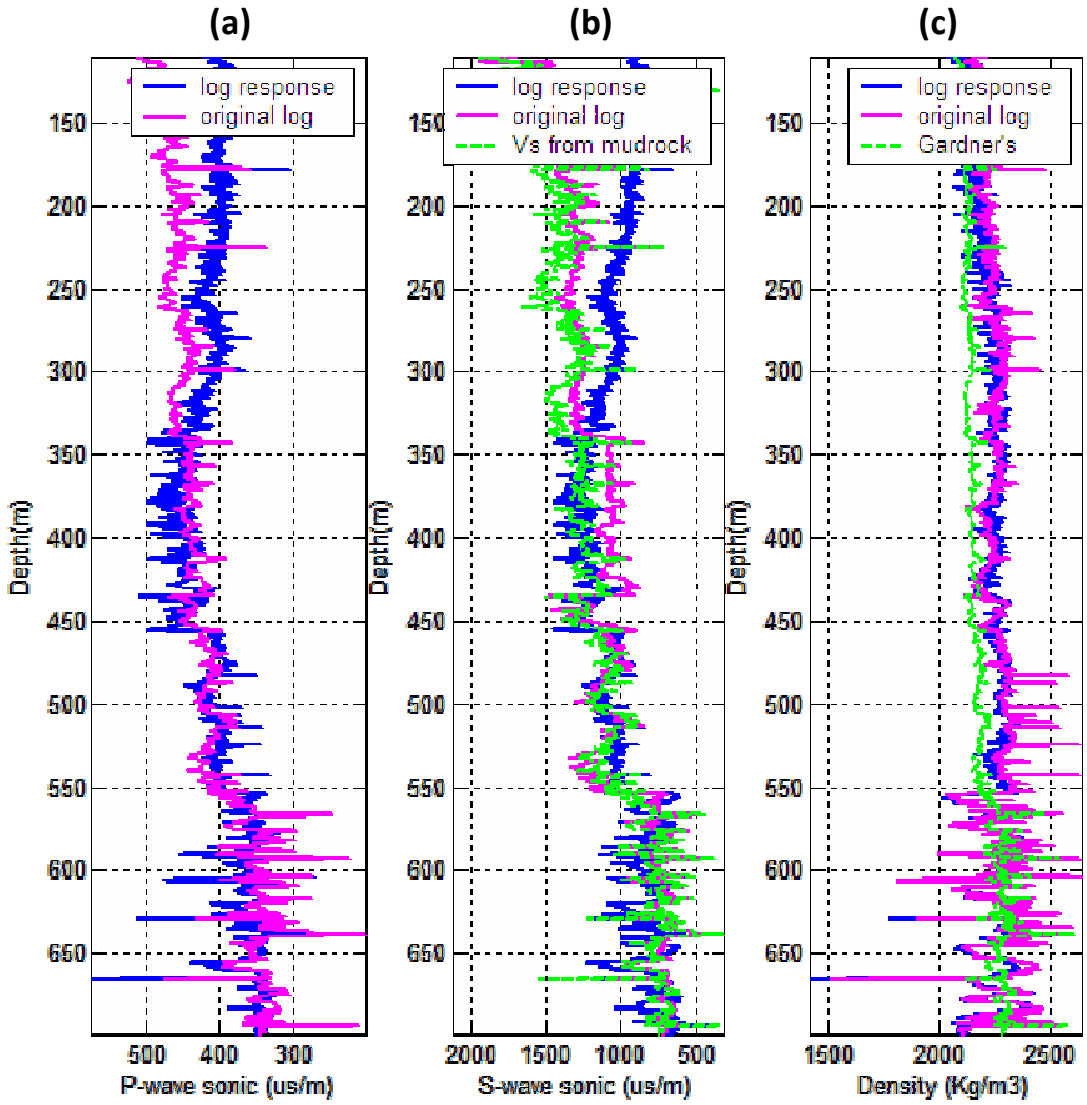

Figure 2.23: (a) P-wave, (b) S-wave and (c) density estimates using the log response equation. Wireline logs are shown in magenta, while the modeled logs are shown in blue. Green lines indicate Vs and density estimates using the mudrock line and Gardner's relation, respectively.

Comparing the results from the log response modelling and empirical relations, such as Gardner's and the mudrock line, we can note that, in general, the Vs estimates using the mudrock line are better, although they fail to reproduce the significant change in Vs at the top of the reservoir. If shear logs modeled from the mudrock line are used to generate synthetic seismograms, the response at the top of the reservoir will not tie with the seismic section.

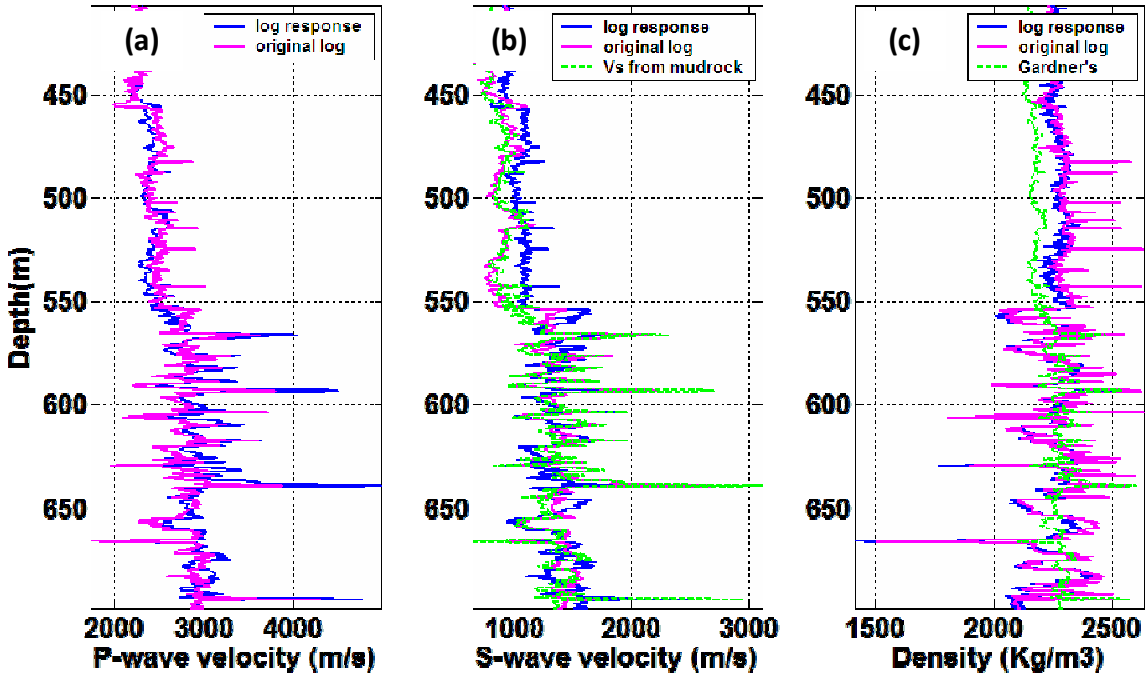

Figure 2.24: Detail of the modeled logs in the interval of interest. The magenta lines correspond to the original wireline logs, the blue lines show the modelled curves, and the green lines show the results of using default parameters in the mudrock and Gardner's equation.

An interesting feature to notice is the deviation of the P- and S-wave velocities in the shallow sections, for depth shallower than 350 m, which suggest that the values selected for the modelling do not represent the near-surface accurately. A possible issue with the modelling approach is that we have not incorporated the increase in matrix velocities with depth (or pressure or compaction). The pressure dependence of seismic velocities in unconsolidated sands is predicted by a power-law relationship, both by theoretical and empirical formulations. However, the exponents of the pressure differ significantly, with these differences being generally attributed to the non-spherical shape of real sand grains or to an increase in the average number of contacts per grain as the sample compacts with loading (Zimmer et al., 2007).

To evaluate the effects of pressure on the seismic velocities, it is necessary to determine the pressure gradient in the area. Lithostatic pressure was calculated from the weight of the overburden, integrating the density log with increasing depth, using the following equation:

$$P_{litho} = P_{atm} + g \sum \rho(z) \Delta z, \tag{2.8}$$

where P_{atm} is atmospheric pressure at the surface, g is gravity acceleration and equal to 9.8 m/s^2, $\rho(z)$ is the density log value at each depth, and Δz is the depth interval. In normally pressured rocks, pore pressure is equal to the hydrostatic, which is the pressure due to the weight of the overlying fluid column. Finally, effective pressure is calculated by subtracting the pore pressure from the lithostatic pressure (Figure 2.25). Note that the effective pressure is almost equal to the hydrostatic pressure.

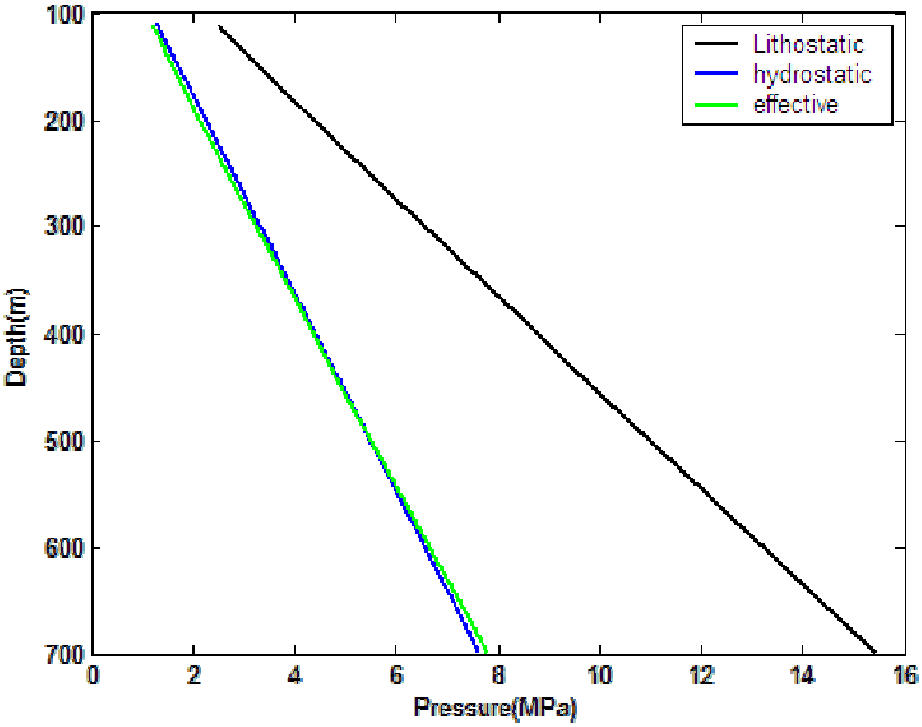

Figure 2.25: Lithostatic (black), hydrostatic (blue) and effective (green) pressures calculated for well A11-17.

Fam and Santamaria (1997) demonstrated that S-wave velocity is related to effective pressure by an equation of the form:

$$V_s = OCR^k S \left(\frac{p\prime}{p_a}\right)^{n/2}, \tag{2.9}$$

where p' is effective pressure and p_a is atmospheric pressure. The term OCR^k corrects for the effects of compaction or preconsolidation of the sample, where OCR is the overconsolidation ratio, and k is a function of the plasticity index. The parameter k is usually assumed to be zero for clean sands, making the term OCR^k equal to 1.

Zimmer et al (2007) measured compressional and shear wave velocities in a series of unconsolidated granular samples, including dry and water saturated natural sands, at pressures ranging from 0.1 to 20 MPa. They applied empirical fits to quantify the velocity-pressure behaviour of the samples, using a modified version of equation 2.9 as follows:

$$V_p = V_{p0} + OCR^k S \left(\frac{p\prime}{p_a}\right)^{n/2}. \tag{2.10}$$

Among the different samples used by Zimmer et al (2007), the Merritt and Gulf of Mexico samples were selected to compare to the Manitou Lake data, as their mineralogic composition (See Table 2.7) was the closest to the expected composition of the sands in Manitou Lake.

Table 2.7: Porosity and mineralogic composition of unconsolidated sand samples used by Zimmer et al (2007).

Sample	**ϕ**	**Quartz %**	**Plagioclase %**	**K-feldspar %**	**Amphibole %**	**Total clay %**	**Other %**
Gulf of Mexico	0.427	63	17	8	1	6	5
Merritt	0.339	59	18	7	5	11	--

Table 2.8: Velocity fit coefficients for equations 2.9 and 2.10 for water saturated samples (From Zimmer et al., 2007).

Sample	S-wave velocity			P-wave velocity			
	S (m/s)	n/2	K	S (m/s)	n/2	K	V_{p0} (m/s)
Gulf of Mexico	174	0.312	0.029	18	0.595	0.223	1744
Merritt sand	169	0.332	0.088	12	0.739	0.437	1799

The P- and S-wave sonic logs from the Manitou Lake area were fitted to equations of the form of 2.9 and 2.10, in order to compare to the modelled results from the Merritt and Gulf of Mexico sands (Figure 2.26). Note that the models based on the Merritt and Gulf of Mexico parameters results in P- and S-wave velocities significantly lower than those seen in the data from Manitou Lake for the same pressure. Although the Manitou Lake sands have a similar mineralogy and porosity to those of the samples in the Zimmer et al (2007) study, they are consolidated, which could account for the significant shift observed in the curves. This suggests that compaction and cementation have a very significant effect on both P- and S-wave velocities, more than doubling the velocities in this particular case.

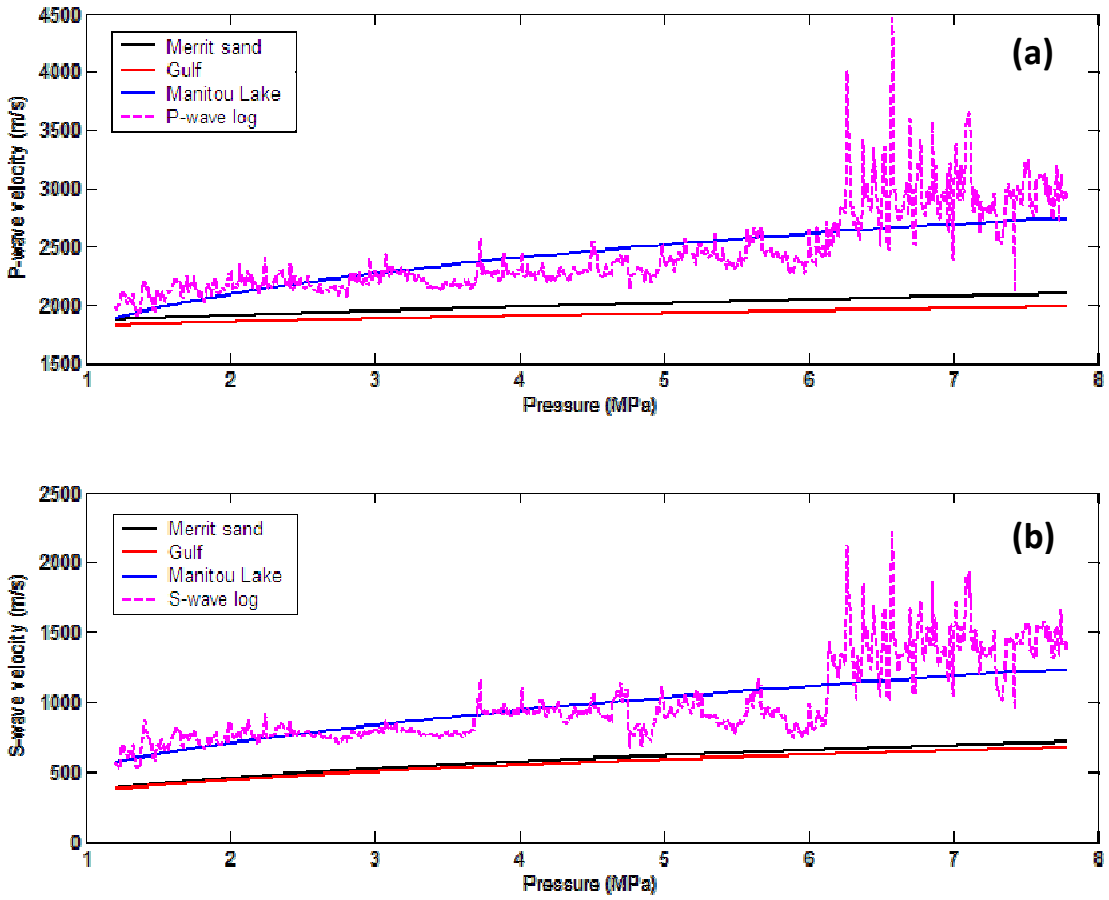

Figure 2.26: (a) P- and (b) S- wave velocity variations with pressure, calculated from equation 2.10, with fit parameters from the Merritt and Gulf of Mexico samples. The sonic log from Manitou Lake data and the best fit polynomial is shown in magenta and blue, respectively.

Applying the pressure dependence on Vp and Vs in the log response modelling approach results in a significantly better fit in the shallow section of the log (Figure 2.27), which confirms that the divergence in the curves in the shallow section is caused by not including compaction effects in the previous approach. However, the discrepancy between the modelled and original velocity logs that occurs between 350 and 450 m is not improved after the pressure correction.

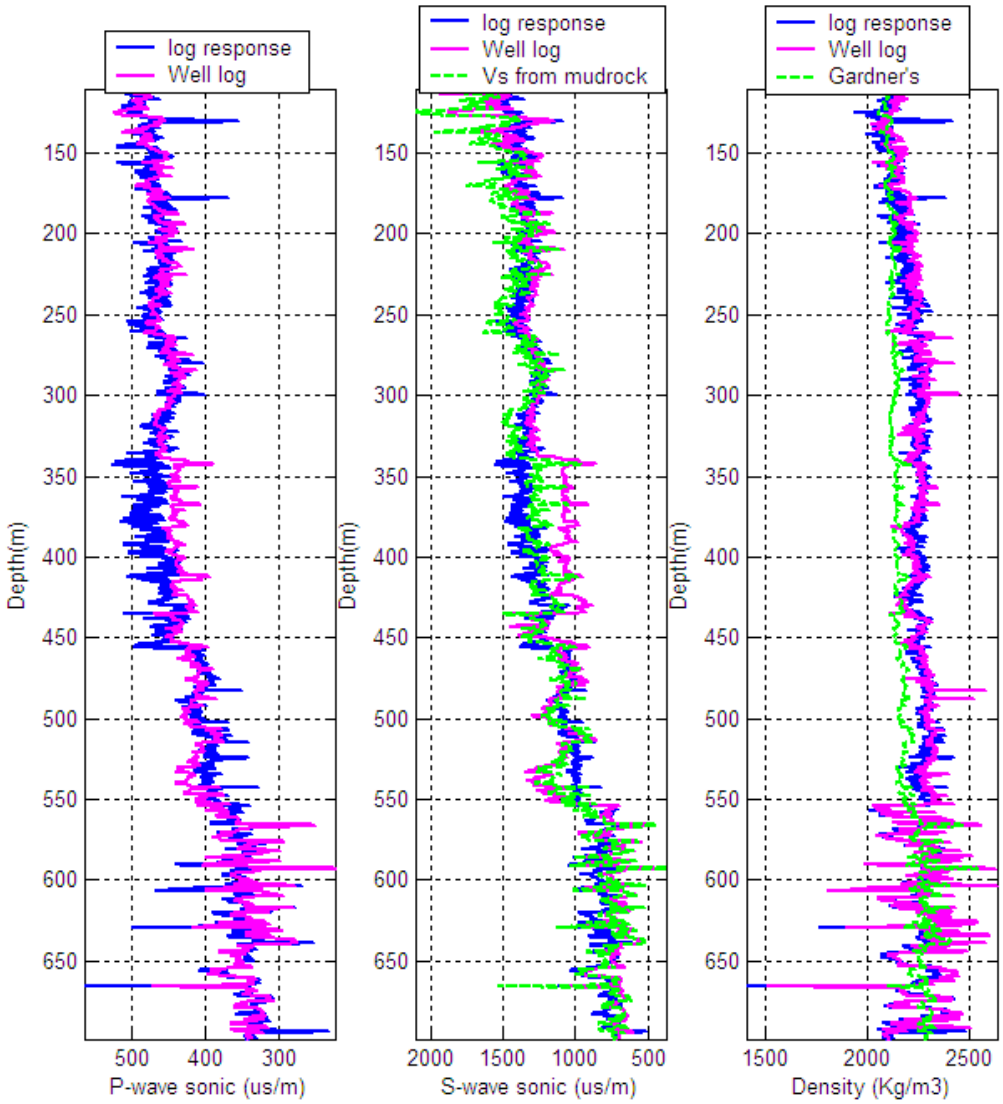

Figure 2.27: Log response modelling after applying the pressure correction for Vp and Vs

2.5.4. Kuster-Toksöz formulation for effective media

An alternative approach for mixed lithologies is composite media modelling, which assumes a solid with inclusions having specific shapes and elastic properties, such as the models by Kuster andTöksoz (1974). These models generally require detailed information about the rock fabric, and they also make assumptions that have not been generally demonstrated to hold for sedimentary rocks (Castagna et al., 1993).

In the next section, the approach by Kuster-Töksoz is evaluated to estimate P- and S-wave velocities. Much of the scatter in porosity-velocity relationships can be attributed to lithology and clay content (Han et al., 1986), impairing the interpretation of well logging data over a broad depth range. Clays are composed of fine sheet like particles, forming pores with much smaller aspect ratios than those associated with sands (Xu and White, 1995).

Using a long-wavelength first–order scattering theory, Kuster and Toksöz (1974) derived equations to estimate P- and S-wave velocities for a two-phase medium with a variety of inclusion shapes. The inclusions must be randomly distributed, generating an isotropic effect, and limited to a dilute concentration, formally limiting these expressions for low porosity cases. The cavities are isolated with respect to flow, simulating very high-frequency saturated-rock behavior, which is appropriate for ultrasonic lab conditions; however, at low frequencies, such as the ones available in seismic data, it is better to find the effective moduli for dry cavities and then saturate them with the Gassmann low frequency relations (Mavko et al., 1998).

The algorithm used for the modelling was coded by Zimin Zhang in Matlab, and it is based on Kuster-Toksöz model and Berryman's (1980) generalization of this model. The input parameters for the algorithm include: density and velocity of uncracked medium, density and velocity of inclusion medium, concentration of the inclusions (e.g. porosity), pore aspect ratio and pore geometry, which can be defined as spheres, needles, disks and penny cracks.

In the first modelling attempt, a single value was given for Vp, Vs and density, concentration of the inclusion was defined by the total porosity, a pore-aspect ratio of 0.3 was selected in order for the ratio between pore aspect ratio and porosity to be less than 1,

and spheres were selected as pore geometry. All rocks are assumed to be saturated with brine. These parameters result in a good fit within the predominantly sandy Mannville interval, however, they significantly overestimate Vp and Vs within the shallow section by more than 500 m/s (Figure 2.28). This likely indicates that the shale properties are significantly different from those of the sands.

Table 2.9: Modelling parameters used in the Kuster-Toksöz approach.

	Fit #1	**Fit #2**	**Fit #3**	**Fit #4**
Pore geometry	Spheres	Spheres	Penny cracks	Spheres
α	0.3	0.3	0.3	0.5
Dens (kg/m^3)	2650	2650	2650	2650
Vp (km/s)	3.2	Sand=4/Shale=2	Sand=4/Shale=2	Sand=4/Shale=2
Vs (km/s)	1.6	Sand=2/Shale-0.8	Sand=2/Shale-0.8	Sand=2/Shale-0.8

To incorporate more constrains into the modelling, the shale volume estimated from the GR log was used to estimate a P- and S-wave velocities linearly varying with shale content. Extreme values were given to Vp and Vs to reflect sand and shale conditions, using the Vp/Vs ratio of 2 for the sands and 2.5 for the shales, as estimated for each lithology from the log crossplots. This approach results in a better fit in the shaly section, especially in the P-wave velocity estimate (Figure 2.29). However, the same overestimation of velocities occurs as seen in the log response approach for depth shallower than 350 m. A detail of the modelled logs within the target interval (Figure 2.30) shows a very good fit for both modelled velocities, except for the S-wave velocity right above the Colony top and the overestimation of P-wave velocity below the Colony top. This overestimation is caused by

the assumption that all rocks are brine saturated, which results in a higher velocity than that of the gas-saturated interval seen in the original logs.

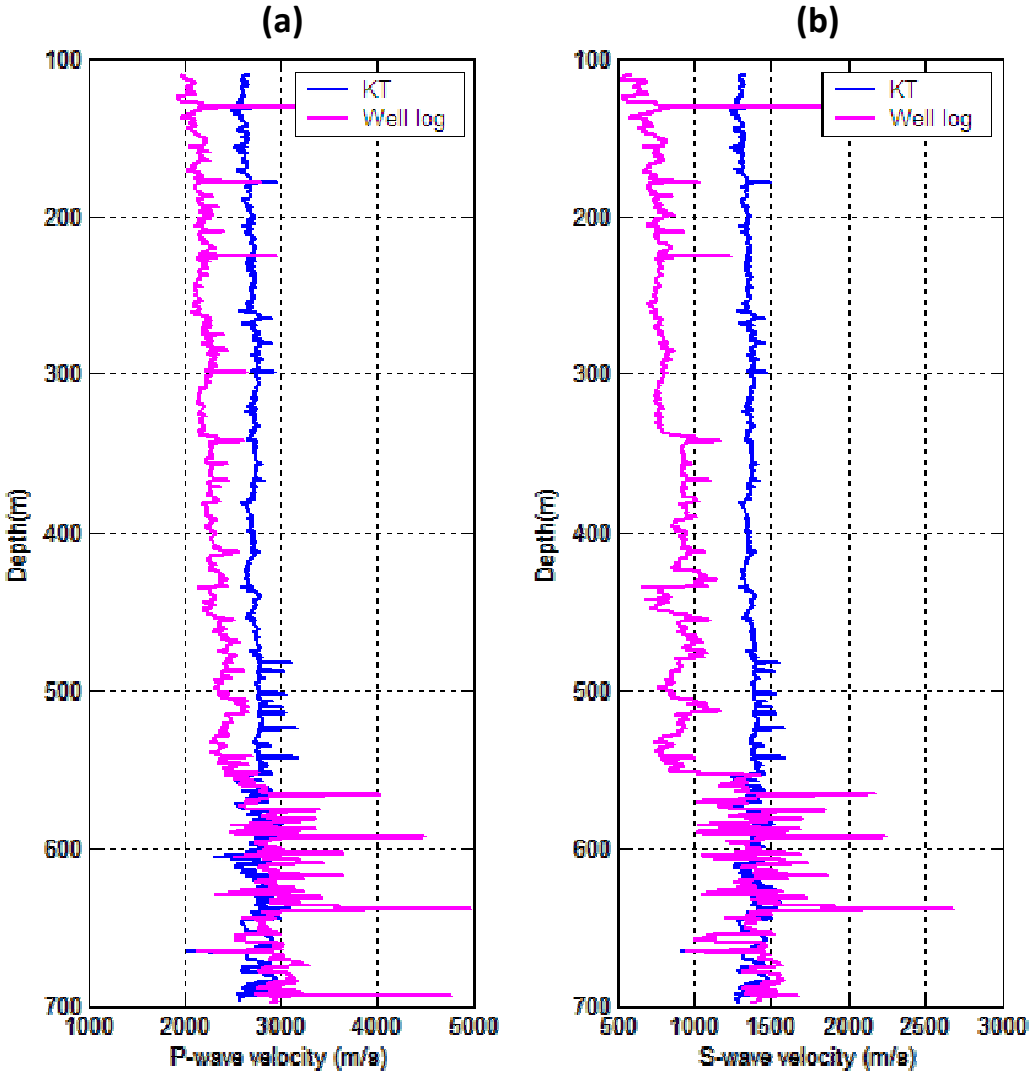

Figure 2.28: Modelled (a)Vp and (b)Vs logs using Kuster-Toksöz's model, with the parameters defined for fit #1 in Table 2.7. Original wireline data shown in magenta, and modelled log shown in blue.

Pore geometries do not affect the modelled velocities very significantly, in particular the P-wave velocity estimation is the same for spheres or penny cracks, with this

change generating variations in the S-wave velocity only. The pore-aspect ratio and the matrix velocities are the most defining factors in the modelling.

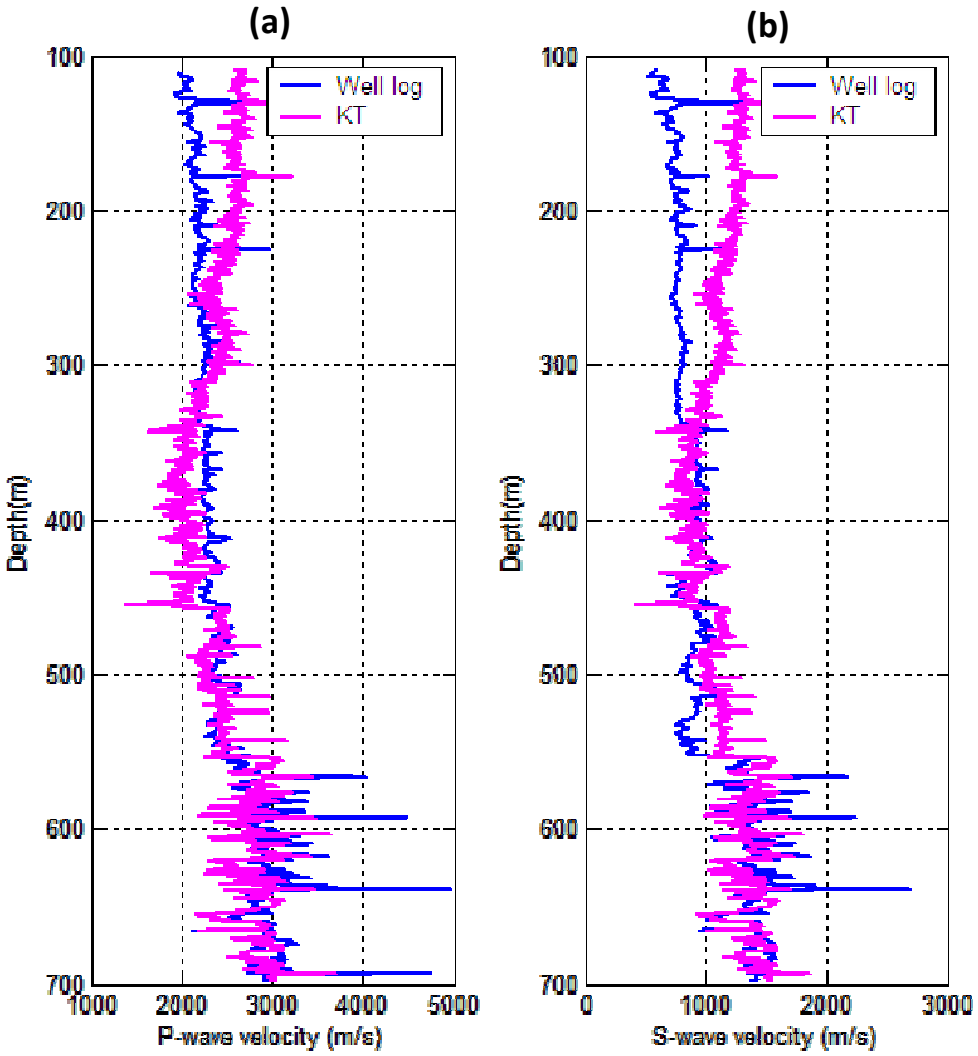

Figure 2.29: Modelled (a)Vp and (b)Vs logs using Kuster-Toksöz's model, with the parameters defined for fit #2 in Table 2.7, assuming matrix velocities are linearly changing with shale volume. Original wireline data shown in magenta, and modelled log shown in blue.

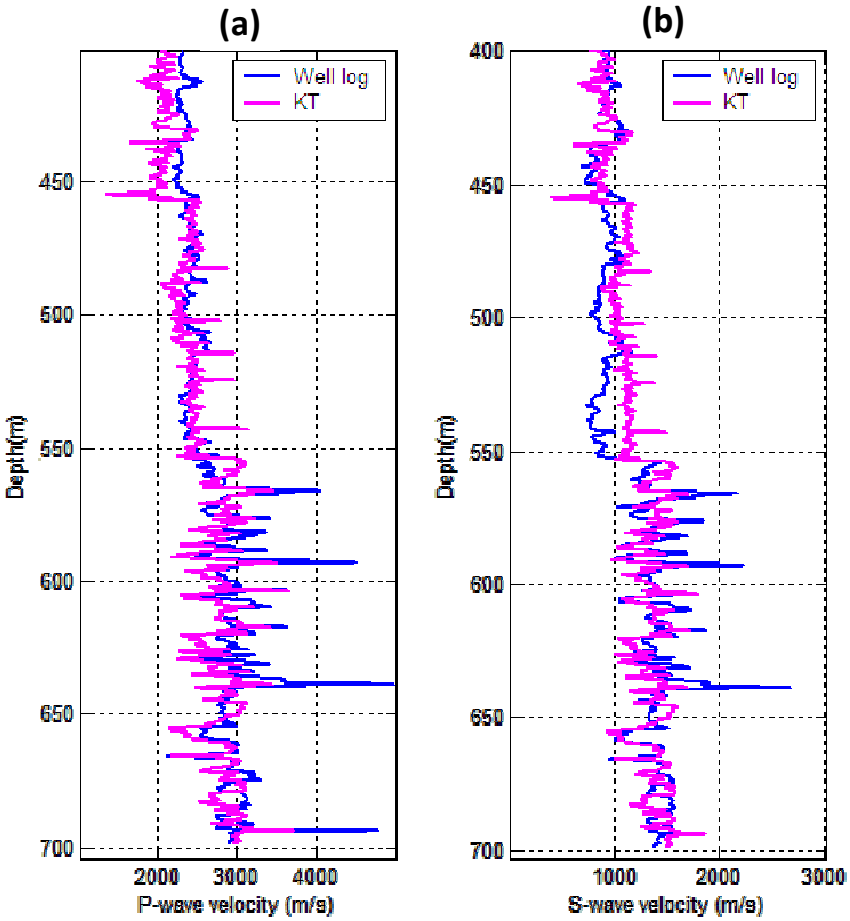

Figure 2.30: Detail of the modeled (a) Vp and (b) Vs logs using fit#2, within the interval of interest.

2.6. SUMMARY

Different modelling techniques were evaluated to predict density and shear-wave velocity. Variations in density in the Manitou Lake area appear to be related to fluid content and lithology. In this particular area, Gardner's empirical relation using the default parameters result in a very poor density estimate, since different factors seem to be affecting density and P-wave velocity. The log response equation method results in accurate velocity and density estimates within the deeper intervals; however, it deviates significantly from the actual logs in the section shallower than 350 m. It also requires a lot

of input parameters, which can be difficult to estimate accurately, limiting the widespread use of this approach.

On the other hand, S-wave predictions with the mudrock line result in accurate Vs estimates, especially within the shalier intervals. The residual between the modeled Vs log and the original log shows potential for use as a sand factor, as Castagna's relation seems to consistently underestimate Vs values within the sand.

CHAPTER THREE: SYNTHETIC MODELLING AND SEISMIC INVERSION

3.1. INTRODUCTION

Multicomponent seismic can significantly improve our understanding of the subsurface, especially in cases when the P-wave data is poor or insufficient. Examples of such cases include: imaging through gas clouds (Stewart et al., 2002) and high-velocity layers (Purnell, 1992, Hanssen et al., 2003), identifying lithology and pore-fluid, detecting aligned fractures using azimuthal anisotropy, and possibly improving time-lapse interpretations. However, converted-wave data usually have some issues that are hard to resolve, such as lower frequency content than the P-wave data, and the difficulty in correlating the P- and S-wave data sets to ensure consistent interpretations of the horizons of interest.

Density can be estimated from seismic data by seismic inversion (i.e. AVO or waveform inversion) or by geostatistical methods, where linear (i.e. multi-linear regression) or non-linear (i.e. neural networks) relationships can be established between the rock properties, calculated at the well location, and the seismic data or a specific seismic attributes.

The following sections show the results from the interpretation and inversion of the converted-wave dataset from Manitou Lake. Synthetic seismograms were generated and tied to the data to allow the interpretation of the horizons of interest. Two inversion approaches (band-limited and model-based) were used to estimate the P- and S-impedance values from the stacked volumes, and finally, the different modelling approaches evaluated in the previous chapter were applied to synthetic traces to evaluate the estimation of density and shear wave velocity from the inverted impedance values.

3.2. INTERPRETATION OF THE MULTICOMPONENT DATA FROM MANITOU LAKE

3.2.1. Synthetic seismograms

To establish a more accurate correlation between the synthetics and the seismic data, and to improve the interpretation of the horizons of interest, a statistical wavelet was extracted from both seismic volumes. A constant phase wavelet was extracted from the PP volume (See Figure 3.1) in the proximity of well C07-16 between crosslines 90 and 100, and inlines 85 to 95. The time window was set from 400 to 650 ms, including all intervals of interest, and the length of the wavelet was set to 100 ms with a taper of 20 ms. The frequency content of the extracted wavelet ranges from 5 to 120 Hz, showing the broad bandwidth of the PP data.

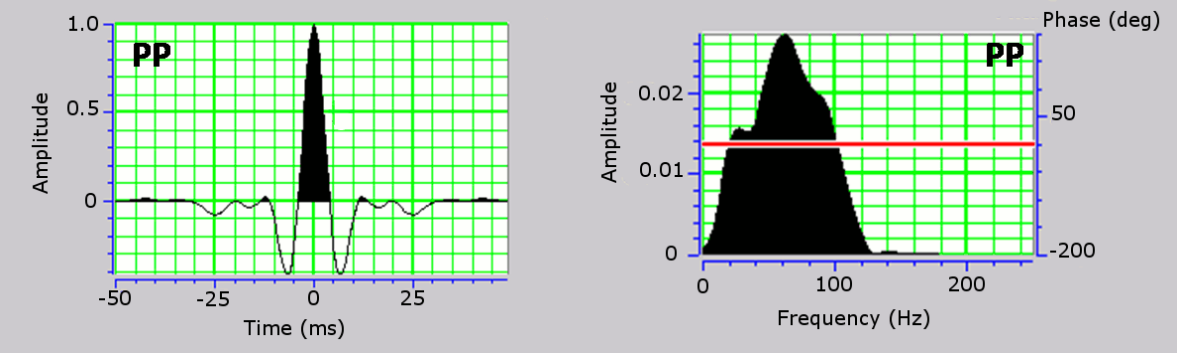

Figure 3.1: (a) Statistical wavelet in time, and (b) amplitude spectrum extracted from the PP seismic volume. The red line indicates the average phase of the wavelet

Synthetic correlations for well A11-17 and C07-16 (Figures 3.2 and 3.3) using the statistical wavelet extracted from the seismic, show a good match with the seismic data, with correlation coefficients of 0.610 and 0.806, respectively. This tie is based on a single shift of -17 ms on the logs to account for the lack of log data in the shallow section, without applying any stretching to the sonic log. In both synthetics, the Colony top corresponds to a trough on the seismic section, while the Sparky corresponds to a zero-crossing.

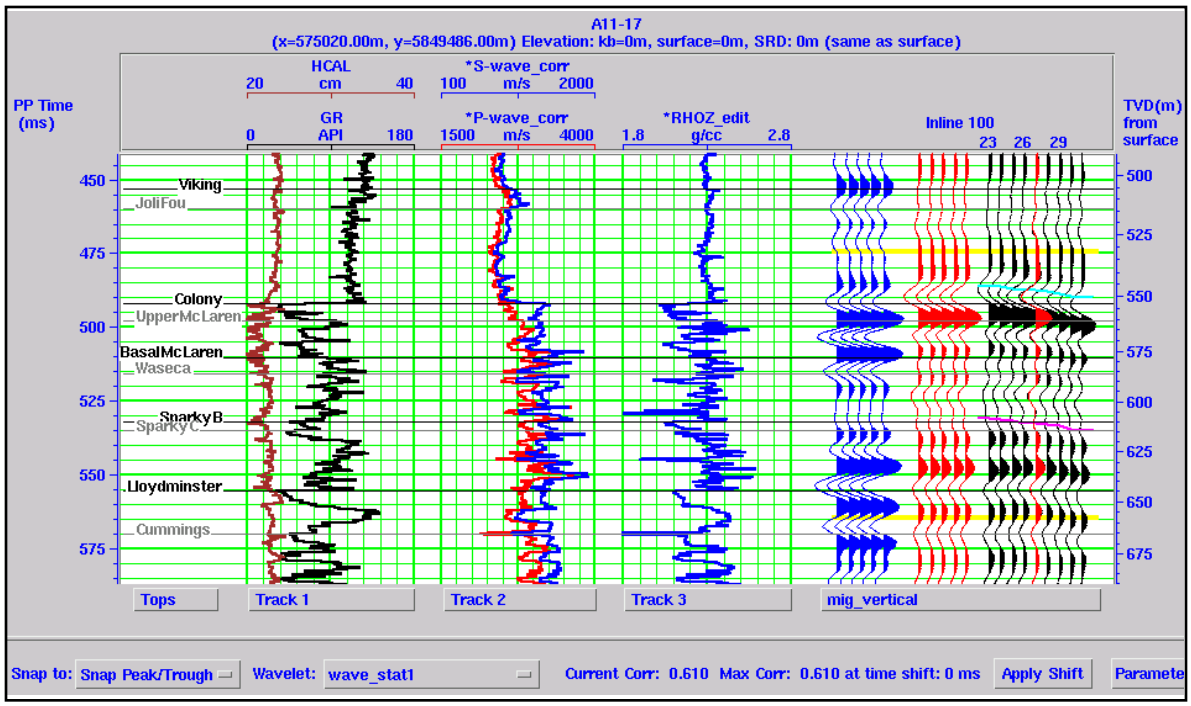

Figure 3.2: Correlation of the PP synthetic and the PP seismic data at well A11-17. Blue traces represent synthetic seismogram, red traces represent the extracted trace from the PP volume at the well location, and black traces shows the ten traces around the well location. Yellow lines show the correlation window used.

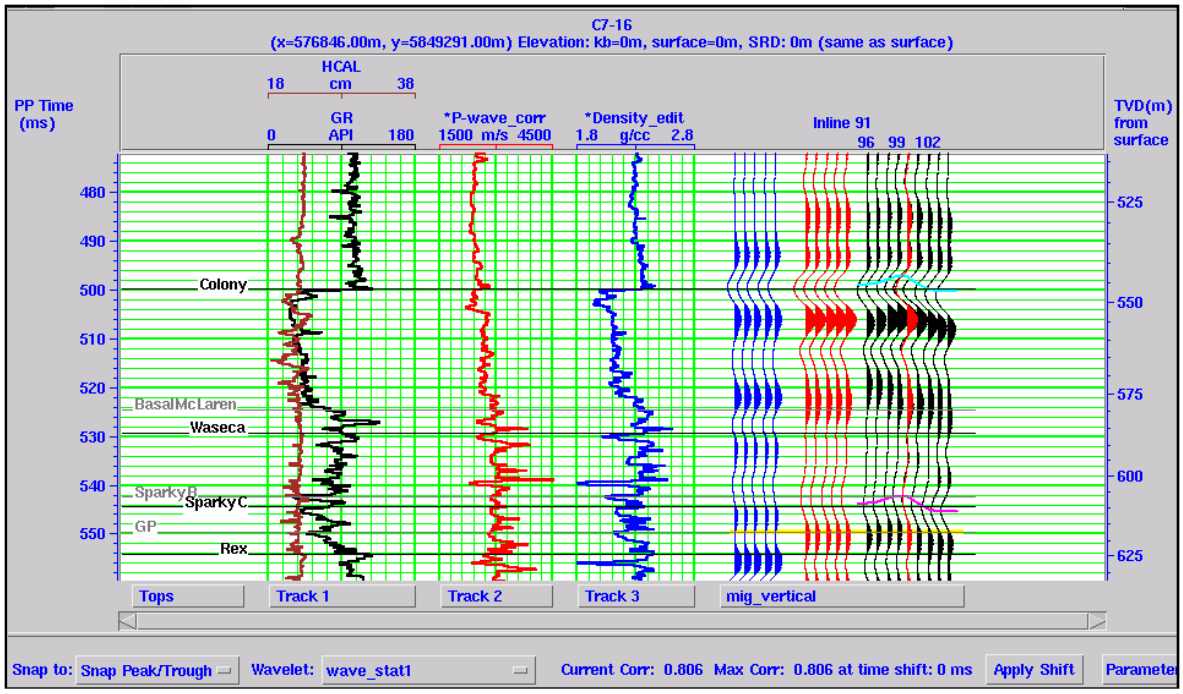

Figure 3.3: Correlation of the PP synthetic and the PP seismic at well C07-16. Blue traces represent synthetic seismogram, red traces represent the extracted trace from the PP volume at the well location, and black traces shows the ten traces around the well location. Yellow lines show the correlation window used.

A statistical wavelet was also extracted from the PS seismic volume (Figure 3.4) in the proximity of well C07-16, between crosslines 90-100 and inlines 85 to 95. The time window was set from 800 to 1300 ms, and the wavelet length was 200 ms with a taper of 50 ms. Note the significantly lower frequency content of the PS data with respect to the PP data. The PS frequency band extends from 5 to 40 Hz, showing a dominant frequency of ~17 Hz. Note the very broad sidelobes of the wavelet, suggesting interference could be a significant problem in the PS section.

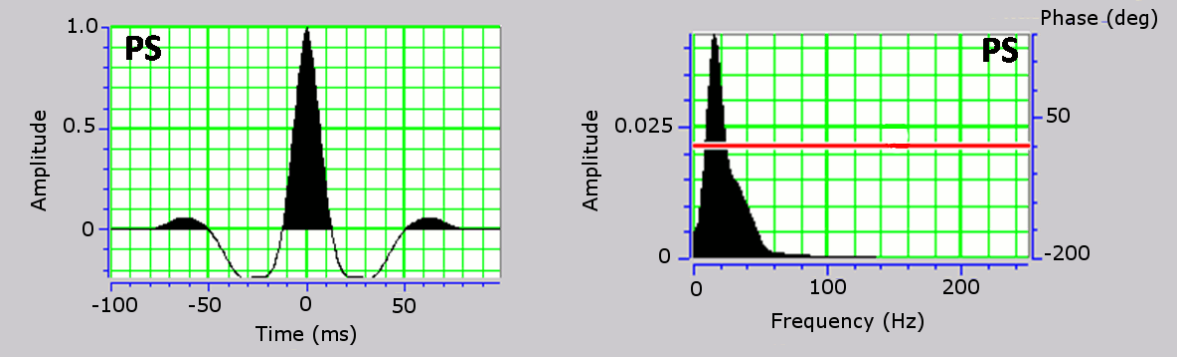

Figure 3.4: (a) Statistical wavelet in time, and (b) amplitude spectrum extracted from the PS seismic volume. The red line shows the average phase of the wavelet.

The correlation between the synthetic and the seismic is very good (Figure 3.5), with a correlation coefficient of 0.751, calculated using a time window from 860 to 1200 ms. The correlation was done applying a single time shift of -57 ms, with no stretching of the sonic log. Both the Colony and Sparky tops correspond to a peak in the PS section. Visual comparison of the synthetic and the extracted seismic trace appears to indicate a phase shift in the seismic; however, it is hard to quantify this phase difference.

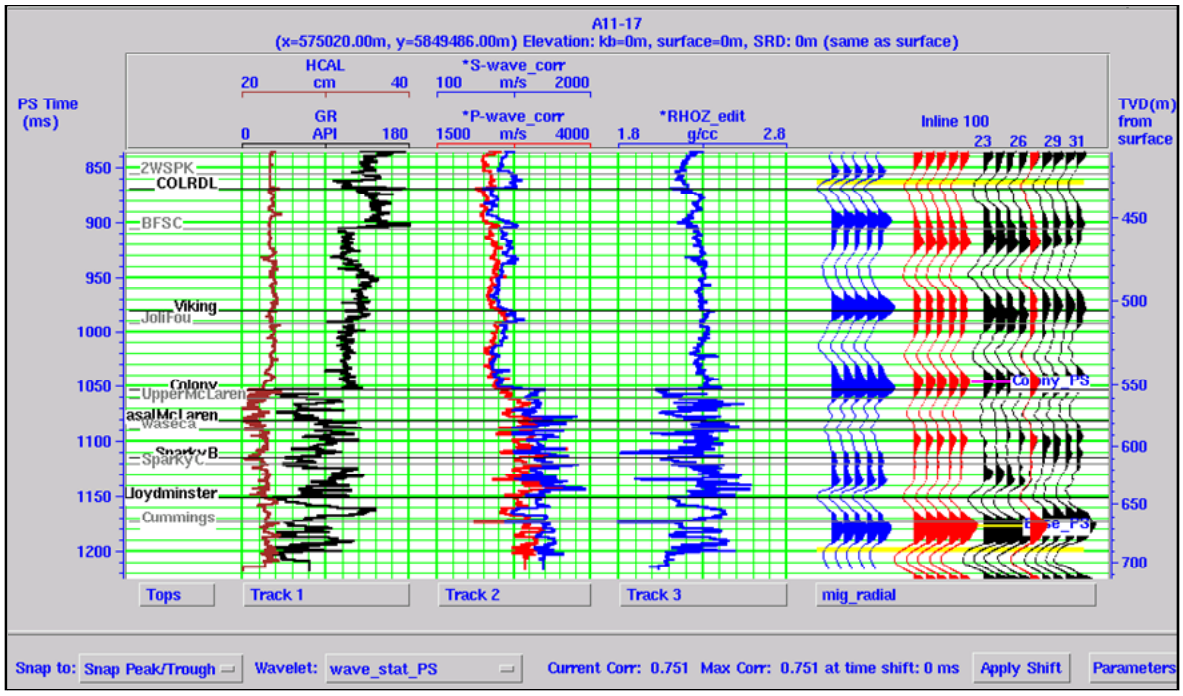

Figure 3.5: Correlation of the PS synthetic from well A11-17 with the PS seismic volume. Blue traces represent synthetic seismogram, red traces represent the extracted trace from the PS volume at the well location, and black traces shows the ten traces around the well location. Yellow lines show the correlation window used.

The stratigraphy in the area is mostly flat, with no faulting or significant dips in most horizons. The Colony channels appear to have a very distinctive expression in the PP seismic data, with lateral changes in amplitudes and waveform character around both wells at the top of the Colony, likely indicating the lateral extent of the sand channels (Figures 3.6 and 3.7). The Sparky interval is within a quiet seismic zone, where it appears there are little variations in the reflection coefficients. The amplitude ad waveform changes within the Sparky B zone are more subtle, and harder to identify directly from the seismic sections, suggesting it is more laterally continuous than the Colony interval.

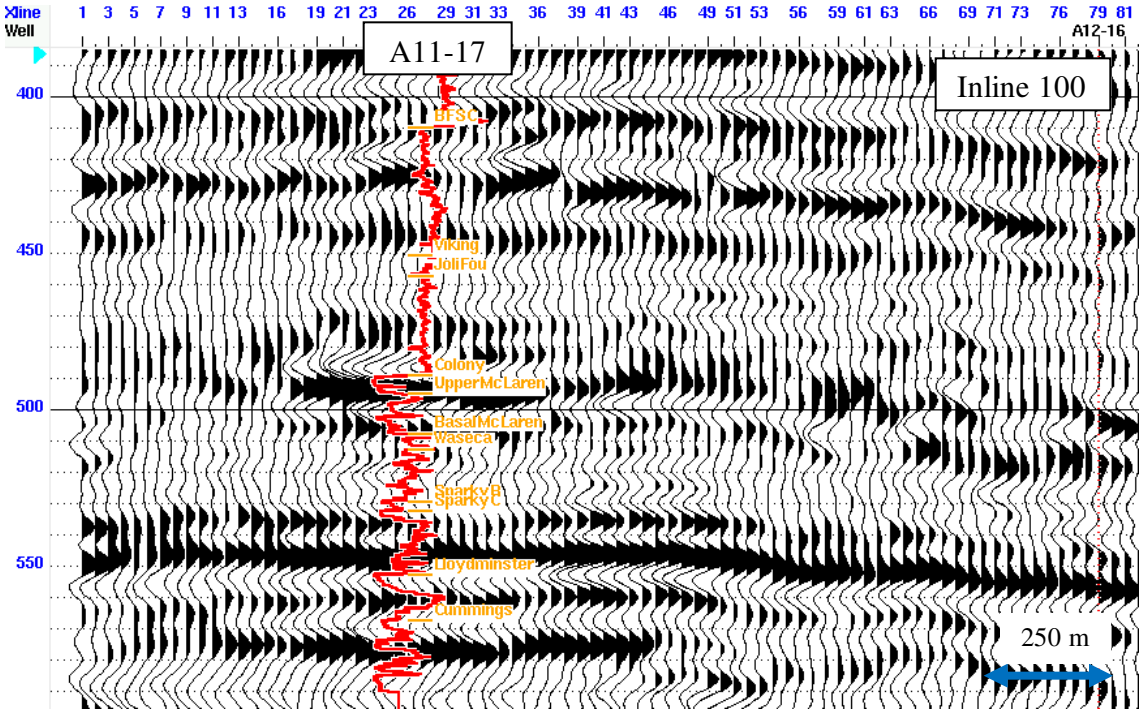

Figure 3.6: Seismic expression of the Colony channel at inline 100 from the PP volume. GR log is annotated in red at the location of well A11-17.

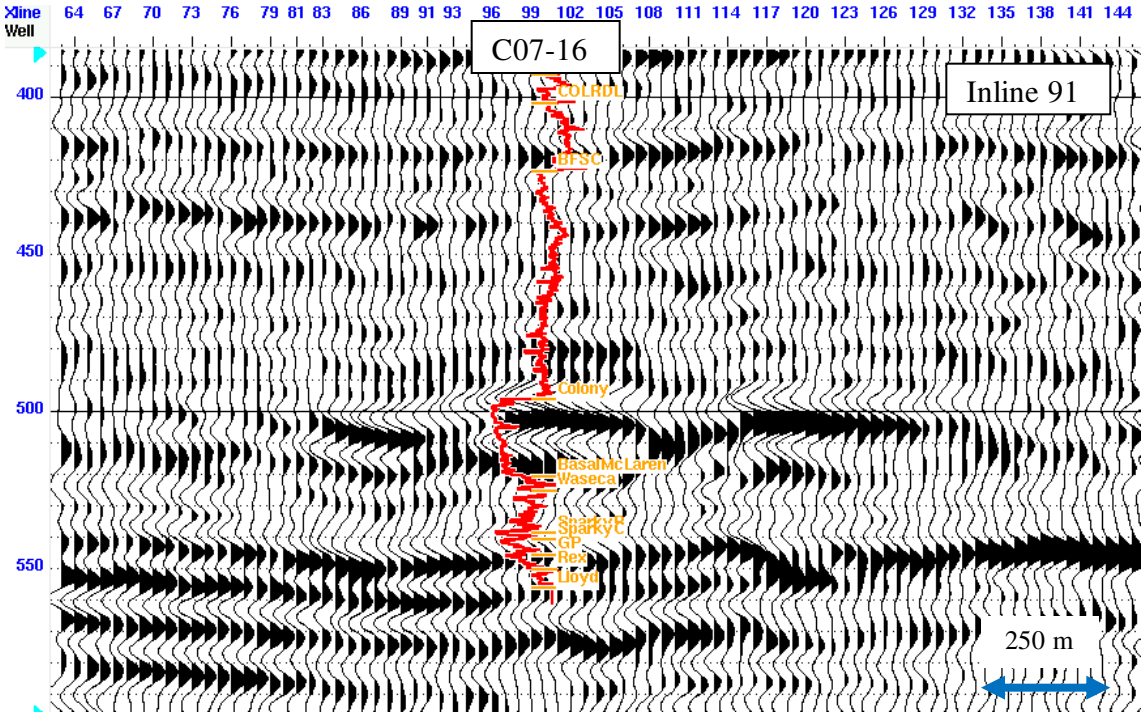

Figure 3.7: Seismic expression of the Colony channel at inline 91 from the PP volume. GR log is annotated in red at the location of well C07-16.

3.2.2. Vertical resolution of the PP and PS seismic volumes

As mentioned previously, the PP and PS seismic volumes from Manitou Lake have a significant difference in bandwidth, resulting in differences in the vertical resolution, which has a key impact when searching for subtle stratigraphic traps. The vertical resolution of the seismic data is related to the minimum thickness a bed must have so that reflections from the top and bottom of the bed can be distinguished. The Rayleigh criterion in optics (See Figure 3.8) establishes that the limit of an optical instrument to distinguish separate images of objects lying close together occurs when the two diffraction images are separated by a distance equal to the peak-to-trough distance of the diffraction pattern (Kallweit and Wood, 1982).

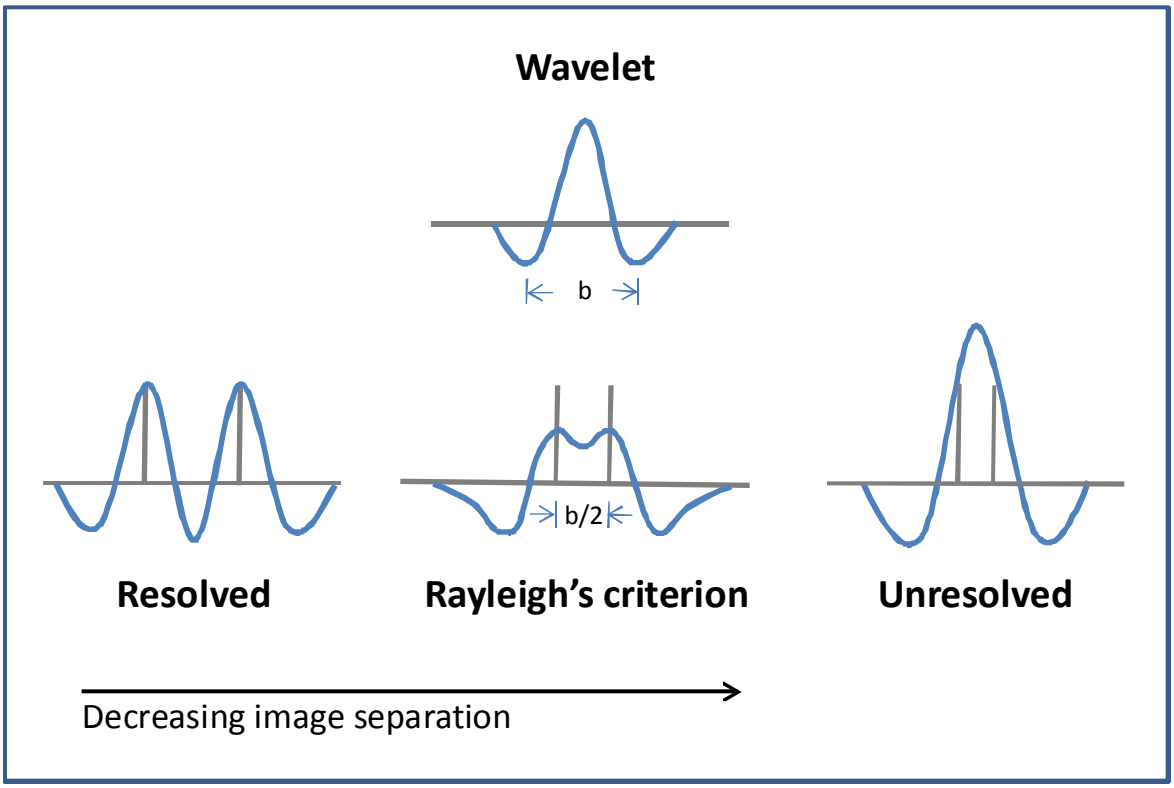

Figure 3.8: Rayleigh's criterion of resolution applied to a seismic wavelet. Two images can be resolved when they are separated by at least the peak-to-trough interval (Based on Kallweit and Wood, 1982)

To relate Rayleigh's temporal resolution formulas to bed thickness it is necessary to distinguish between the different terminology for frequency and wavelength. Kallweit and Wood (1982) define peak frequency of Ricker wavelets as the frequency component having the largest value in the Fourier amplitude spectrum; Widess (1973) defines predominant frequency as that obtained by computing the reciprocal of the time interval between the wavelets two central side lobes.

The amplitude spectrum of the PP seismic volume (Figure 3.a) was calculated using a time window from 200 to 700 ms and all traces in the volume, resulting in a frequency range from 10 to 120 Hz, and validating the results from the wavelet extraction at the well location. The amplitude spectrum of the PS volume (Figure 3.9b) was calculated using a time window from 500 to 1300 ms and all traces in the volume, and it shows the significantly lower frequency content of this volume, with -12 dB attenuation occurring around 35 Hz.

Based on Rayleigh's criterion, Sheriff (2001) defines the minimum distance between successive reflections as a 1/4 of the dominant wavelength (λ_d). For two spikes of equal amplitudes and opposite polarities, Widess' (1973) established the resolvability at 1/8 of the dominant wavelength. Minimum bed thicknesses were defined for PP, SS and PS seismic data using Rayleigh's criterion, based on the dominant frequency of the data (f_d), which can be easily estimated from the amplitude spectrum of the data, and interval velocities within the layer of interest (Figure 3.9). The generalized equation for the PS case can be reduced to the PP and SS cases by assuming Vp=Vs.

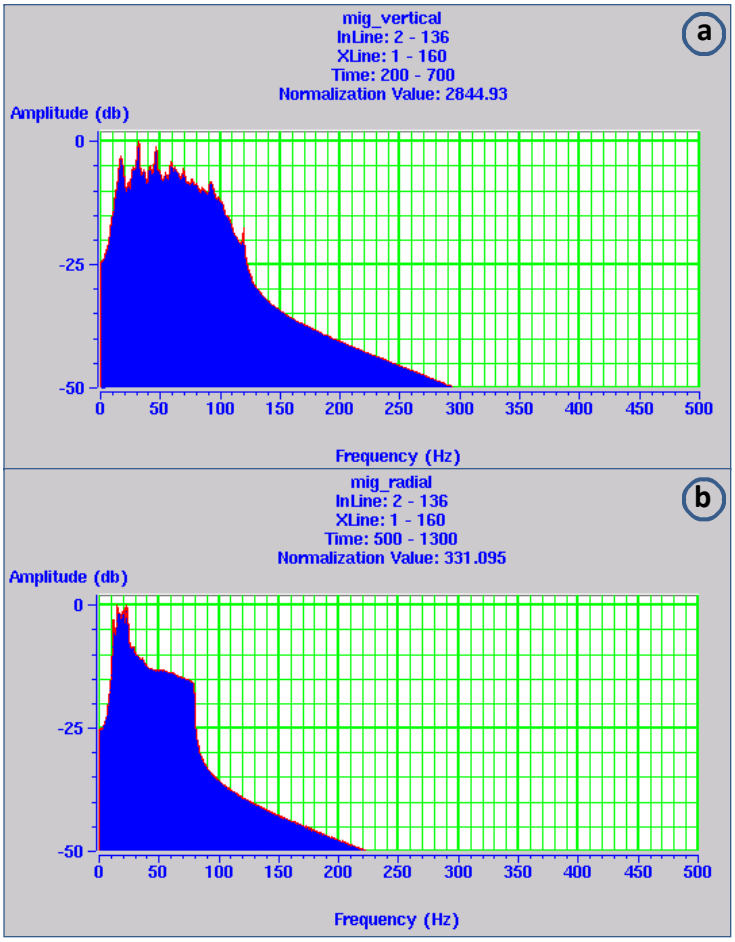

Figure 3.9: Fourier amplitude spectrum in dB of the (a) PP and (b) PS seismic volumes

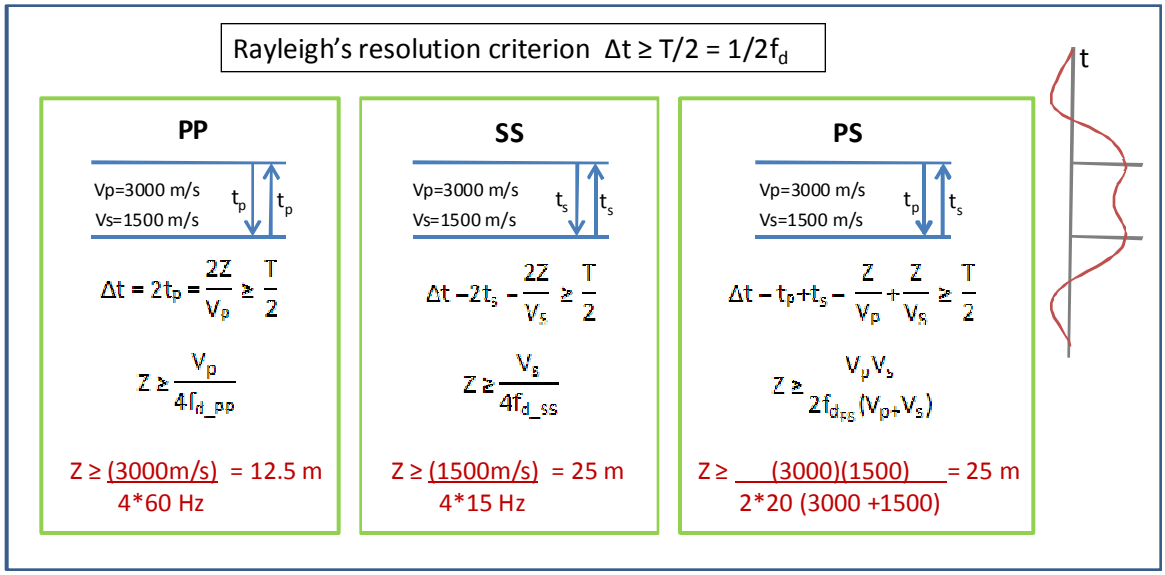

Figure 3.10: Minimum bed thickness formulation for PP, SS and PS seismic data, based on the Rayleigh criterion.

Based on the estimated amplitude spectrum and the extracted wavelet, the dominant frequency is defined as 60 Hz for the PP volume and 20 Hz for the PS volume. The average P-wave velocity within the Mannville interval is 2900 m/s, while the S-wave velocity averages 1500 m/s. The minimum thickness that can be resolved by each data set was calculated based on the equations shown in Figure 3.10 for the PP, SS and PS case for a range of dominant frequencies between 5 to 100 Hz (Figure 3.11).

In particular for the Manitou Lake data, and considering a target within the Mannville interval, results in minimum bed thicknesses of 12.5 m for the PP data and 25 m for the PS data. Based on the wireline data, the Colony channel is 8 m thick in well A11-17, and the Sparky B is just 5 m thick. In well C07-16, the Colony member reaches a thickness of 33 m, but the Sparky B is just 3 m thick. This indicates that most reservoir targets are below the vertical resolution of the PP data, and significantly below the resolution of the PS data. This could difficult the delineation of the channels with the seismic data, especially for the case of the Sparky B interval, which is very thin and in some cases overlain by htin coal seams.

Given the lower S-wave velocities of any layer, with respect to its corresponding P-wave velocity, SS and PS data will have a better resolution than the P-wave data for any given frequency. However, due to the higher attenuation of S-waves, SS and PS data generally have lower frequency content than the PP data. For the particular case at Manitou Lake, PS data with a dominant frequency of 40 Hz would have the same vertical resolution as PP data with a dominant frequency of 60 Hz.

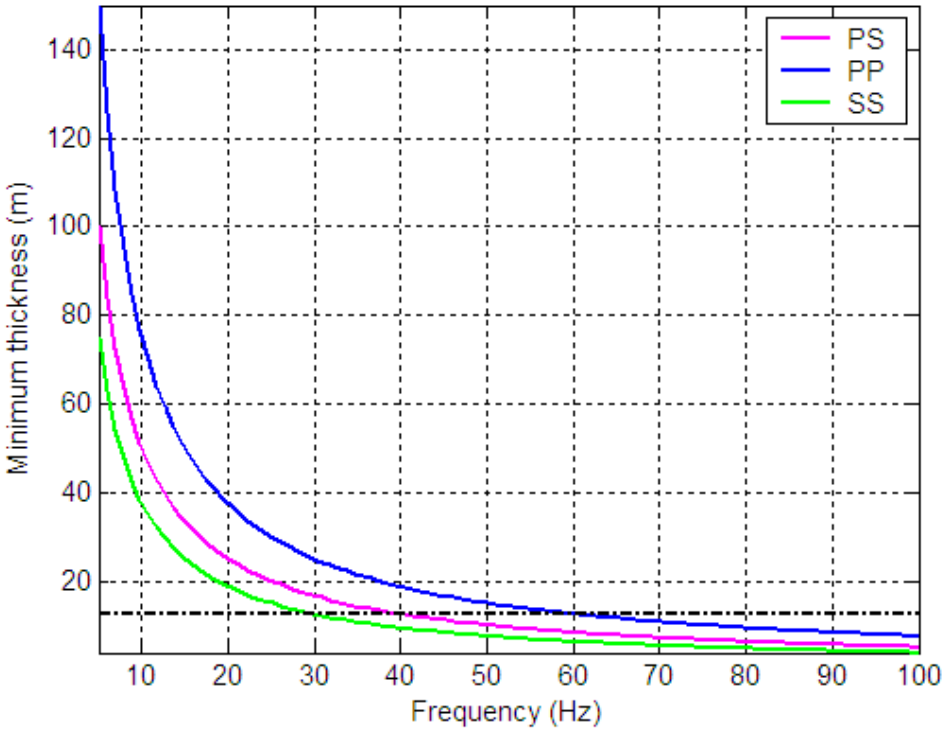

Figure 3.11: Minimum bed thickness that can be resolved with PP, PS and SS seismic data, assuming Vp=3000 m/s and Vs=1500 m/s. Dashed black line shows the minimum bed thickness resolved by 60 Hz PP data. PS seismic with a 40 Hz dominant frequency has the same resolution as the 60 Hz PP seismic, for this velocity pair.

3.2.3. PP and PS registration and horizon picking

Registration of the PP and PS seismic volumes is necessary for an accurate joint interpretation of both volumes. Different automatic methods exist for the registration process, including data correlation (Gaiser, 1996), automatic warping (Fomel et al., 2003), and auto transferring (Nickel and Sonneland, 2004). Zou et al (2006) mention the following problems in event registration procedures: differences of PP and PS reflection responses from a rock physics point of view, uncertainty in the phase of PP and PS reflected wavelets, and differences in PP and PS frequency content. These issues limit the use of automatic correlation approaches, where it is assumed that the PP and PS wavelets reflected at a geologic boundary have the same phase, polarity and strength.

The 3D-3C survey from Manitou Lake is affected by all of these issues. In this area, the top of the Colony sand corresponds to a trough in the PP section, due to the decrease in density and V_p, while it corresponds to a peak in the PS section, due to the increase in V_s at this interface. Also, there is a significant difference in the bandwidth of both datasets, evidenced in the amplitude spectra of the extracted wavelets. The registration between PP and PS synthetics generated for well A11-17 using Ricker wavelets with a dominant frequency of 60 and 18 Hz, respectively, shows the difficulty in correlating two single events from the two synthetics, due to the changes in polarity in the main reservoirs and the lower frequency content of the PS data (Figure 3.12).

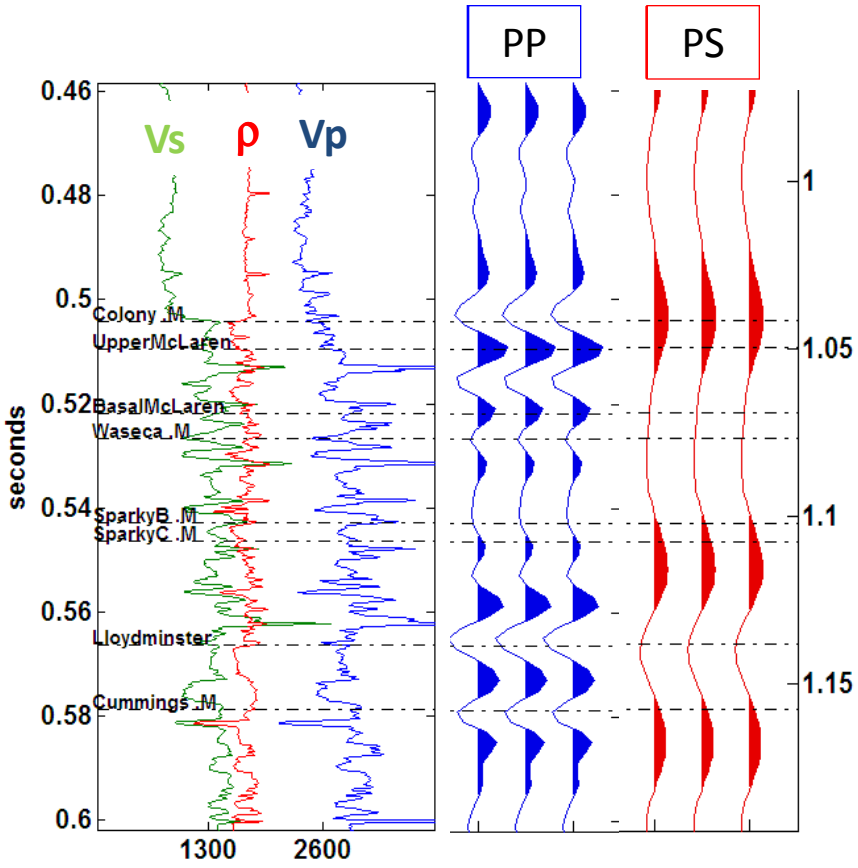

Figure 3.12: Registration between the PP (blue traces) and PS (red traces) stacked synthetic traces for well A11-17. Vp, Vs and density used to generate synthetics are shown to the left of the traces. Note the different character of PP and PS response at the top of the Colony and Sparky horizons.

The registration of the actual PP and PS data (Figure 3.13) highlights the frequency differences between the two volumes, and the variations in reflection character between the two volumes. The PS volume also seems to be affected by some residual static, or possibly some acquisition footprint, which make it difficult to identify lateral variations associated with the sand channels.

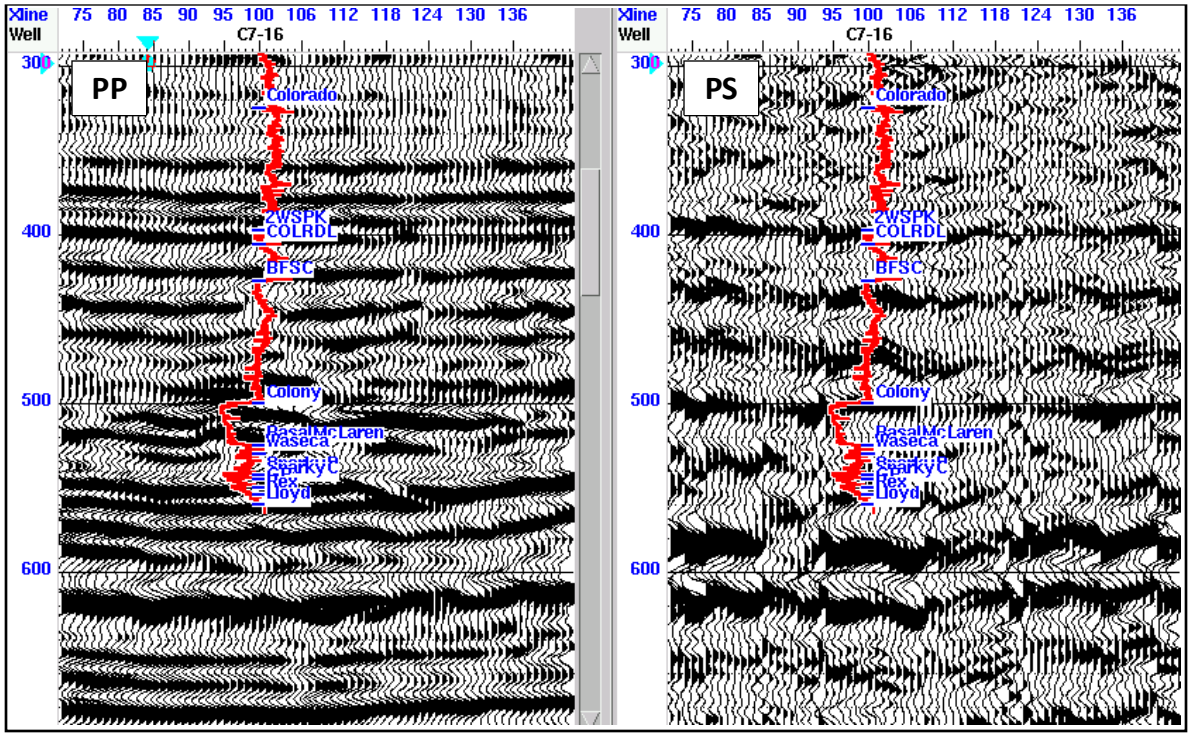

Figure 3.13: Registration between the PP and PS seismic volumes. GR log is annotated in red at the location of well C07-16.

3.2.4. AVO effects

PP and PS pre-stack synthetic seismograms were generated for well A11-17 using the Syngram program (Figure 3.14). Given the very different character of the P- and S-wave velocities at the top of the sand channels, it is also expected that they will have different AVO responses. The significant increase of the S-wave velocity at the top of the Colony suggests bright spots are expected in the PS section associated with sand intervals.

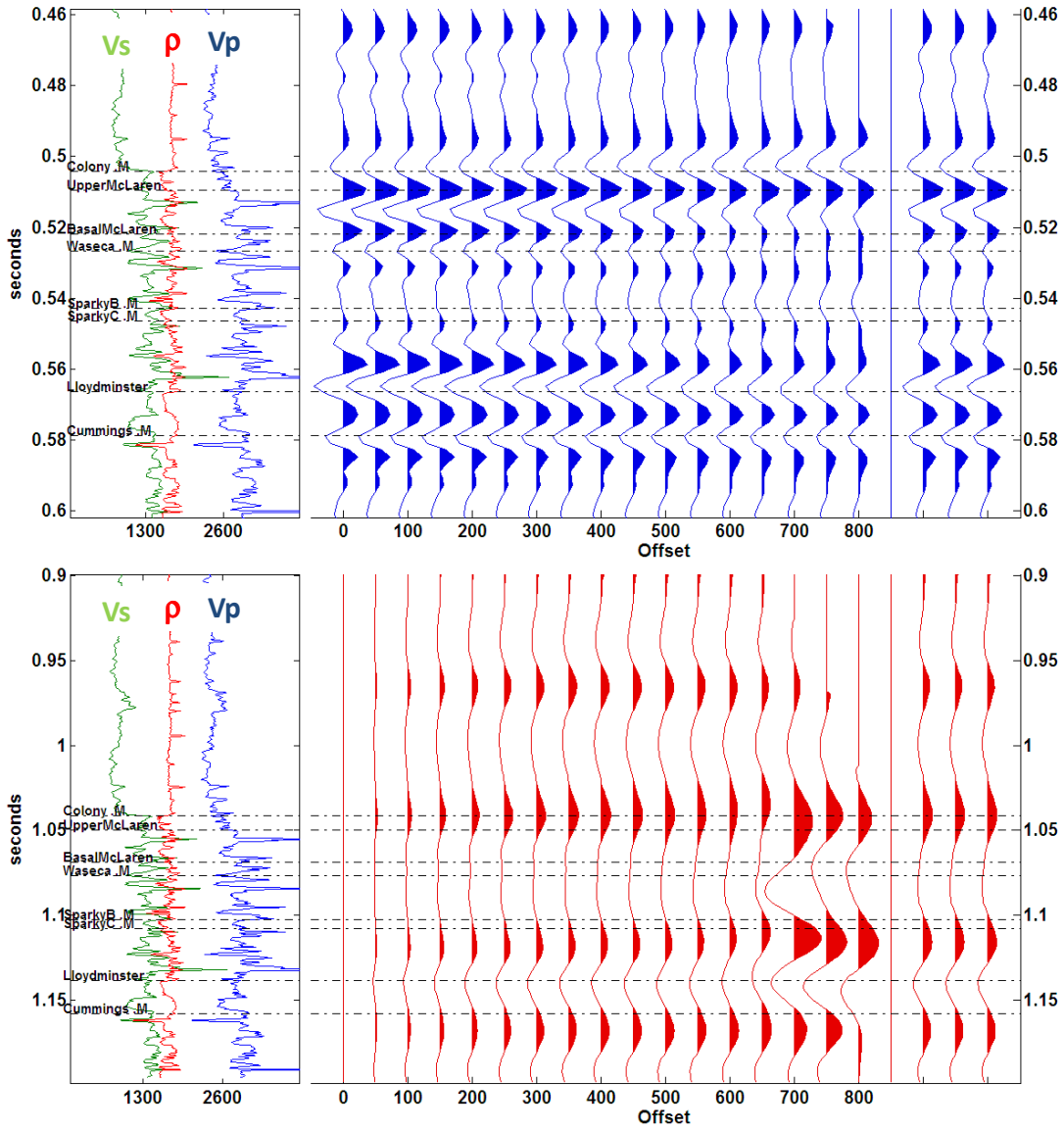

Figure 3.14: Pre-stack PP (blue) and PS (red) synthetic gathers for well A11-17.

The top of the Colony sand in the PP section appears to show a class III AVO anomaly, corresponding to a large negative reflection coefficient at zero-offset and brightening with increasing offset. A similar response is observed at the top of the Sparky B interval. Note that the response in the water-saturated Lloydminster interval is opposite to the one seen at the Sparky and Colony tops, having a large negative reflection coefficient at zero-offset and dimming with increasing offset.

3.3. SEISMIC INVERSION

Different approaches can be used for post-stack inversion of seismic data, including band-limited, model-based, or sparse spike, among others. Band-limited impedance inversion is often undertaken with the classical recursive inversion algorithm (Lindseth, 1979), which ignores the effect of the seismic wavelet, and treats the trace as a set of reflection coefficients, with the low-frequency component added from the well logs. The advantage is its simplicity, short computation time and robustness in the presence of noise, but thin layer interference is not accounted for since the wavelet is ignored.

Sparse-spike inversion models the reflectivity as a minimal series of spikes, with spikes being added until the trace is matched accurately enough. This method creates a broad-band, high-frequency model, without the very thin layers in the model inversion method. It results in the simplest possible model that can fit the seismic data, resulting usually in over-simplified geology. It is less dependent on the initial guess model, so it should be use when the area of interest has few major reflectors and there is little knowledge of the geology.

In the next sections we will show the results from using the band-limited and model-based inversion approaches to estimate impedance from synthetics, and PP and PS seismic data. The forward modelling approaches are also evaluated to further estimate Vp, Vs and density from these impedance estimates.

3.3.1. Band-limited impedance inversion

The first inversion approach was done using the BLIMP (Band Limited Impedance Inversion) algorithm (Ferguson and Margrave, 1996) in a Matlab workspace. The normal

incidence reflection coefficients (R_i) are defined in terms of the impedance (I_i), where i and $i+1$ are consecutive layers, as:

$$R_i = \frac{I_{i+1} - I_i}{I_{i+1} + I_i} \tag{3.1}$$

Solving for I_{i+1}, taking the natural logarithm, making an approximation for small R and modelling the seismic trace as a scaled reflectivity ($S_k = 2R_k / C$), equation (3.1) is expressed as:

$$I_{i+1} = I_1 \exp\left(C \sum_{k=1}^{i} S_k \right) \tag{3.2}$$

The inversion is performed using an approach similar to that of Waters (1978). An initial impedance estimate is calculated from the well logs, and the seismic trace is integrated and exponentiated, according to equation 3.2. The Fourier spectrum of the integrated trace is scaled to that of the estimated impedance, and the low-pass filtered impedance is added to the trace. The result is transformed to the time domain, and a new impedance estimate is obtained. In this case, the low- and high-cut frequencies were set to 10 and 100 Hz, respectively.

The first synthetic trace is generated using the function *theosimple* from Matlab, which calculates a 1-D synthetic seismogram using a convolutional model. A Ricker wavelet with a dominant frequency of 80 Hz was used. The sampling interval was set to 0.001 s and no multiples or transmission losses are included in the model. Figure 3.15 shows the synthetic seismogram generated and the estimated impedance using the band-limited approach described above. The inverted impedance reflects the major changes in the log accurately; however, it fails to reproduce the very high-frequency variations seen in the original impedance log, due to the band-limited character of the seismic data.

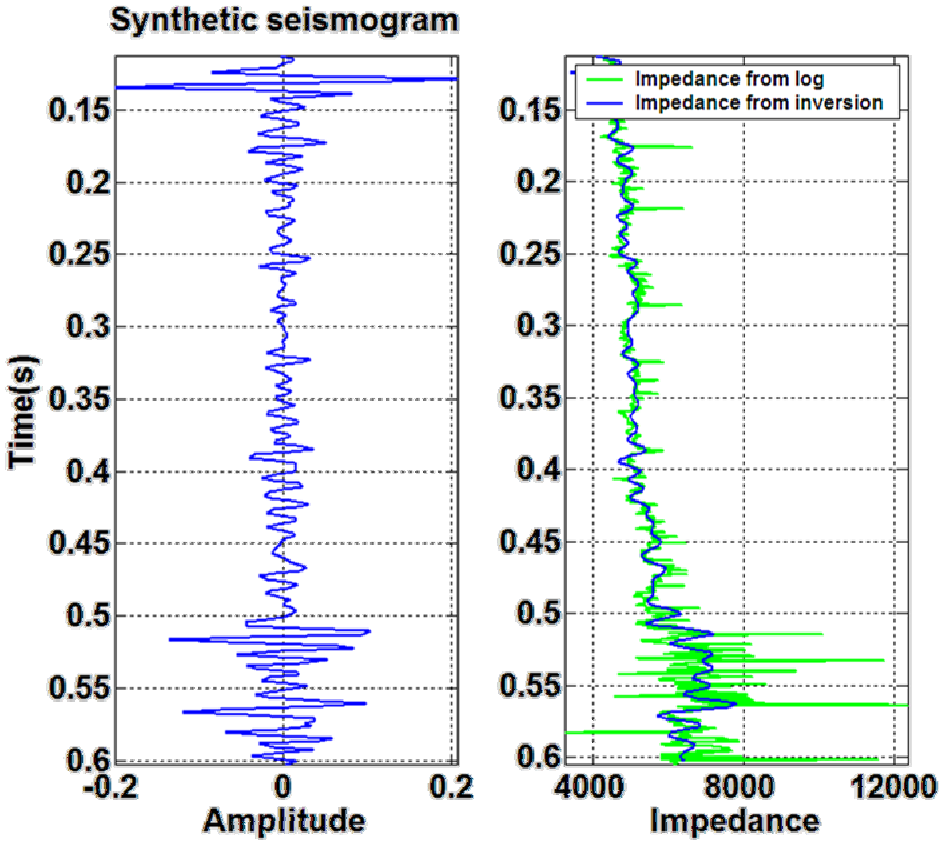

Figure 3.15: Estimated impedance from the band-limited inversion of a synthetic PP stacked trace.

The following approach consists of applying the BLIMP algorithm to the PS seismic data. Converted-wave reflectivity is not defined for zero-offset, since there is no conversion from P- to S-wave for the case of vertical incidence. Theoretically, this limits the application of the band-limited inversion approach to PP data, since the method is defined based on a zero-offset reflectivity. Stewart and Bland (1997) derived an expression that relates PS reflectivity (R^{ps}) to pure shear reflectivity (R^{ss}) at zero-offset, defined as

$$R^{ss}(0) \approx \frac{\alpha}{4\beta}\csc(\theta)R^{ps}(\theta), \tag{3.3}$$

where $R^{ss}(0)$ is the pure-shear reflectivity at zero-offset, α and β are the average P- and S-wave velocity, θ is the angle of incidence, and R^{ps} (θ) is the reflectivity of the converted-

wave. This equation works reasonably well for angles of incidence up to 15° (Stewart and Bland, 1997).

The PS stacked trace results from summing up trace with angles of incidence ranging from 25° in the shallow section to 45° in the deeper intervals. To simplify the application of equation 3.3, it was assumed that the angle of incidence increased linearly with depth. With these assumptions it is then possible to convert the PS trace to SS reflectivity, and then apply the BLIMP inversion. A PS synthetic trace was generated in Syngram considering a 40 Hz Ricker wavelet, and then converted to the equivalent pure-shear trace. A higher frequency than that actually observed on the PS seismic data was used to generate these synthetics in order to be able to evaluate more subtle differences between the traces, which would be harder to identify in the lower frequency synthetics.

The conversion results in an overall change in the magnitude of the amplitudes, as well as a small decrease in the relative amplitudes with depth (Figure 3.16). After evaluating the band-limited inversion of both the PS and the SS trace it is possible to note that there is very little change in the inverted impedance, especially within the shallow section. This is probably due to the scaling step within the algorithm, which scales the amplitude spectra of the trace to that of the initial model. If the variations in relative amplitudes were more significant, the conversion could result in bigger differences.

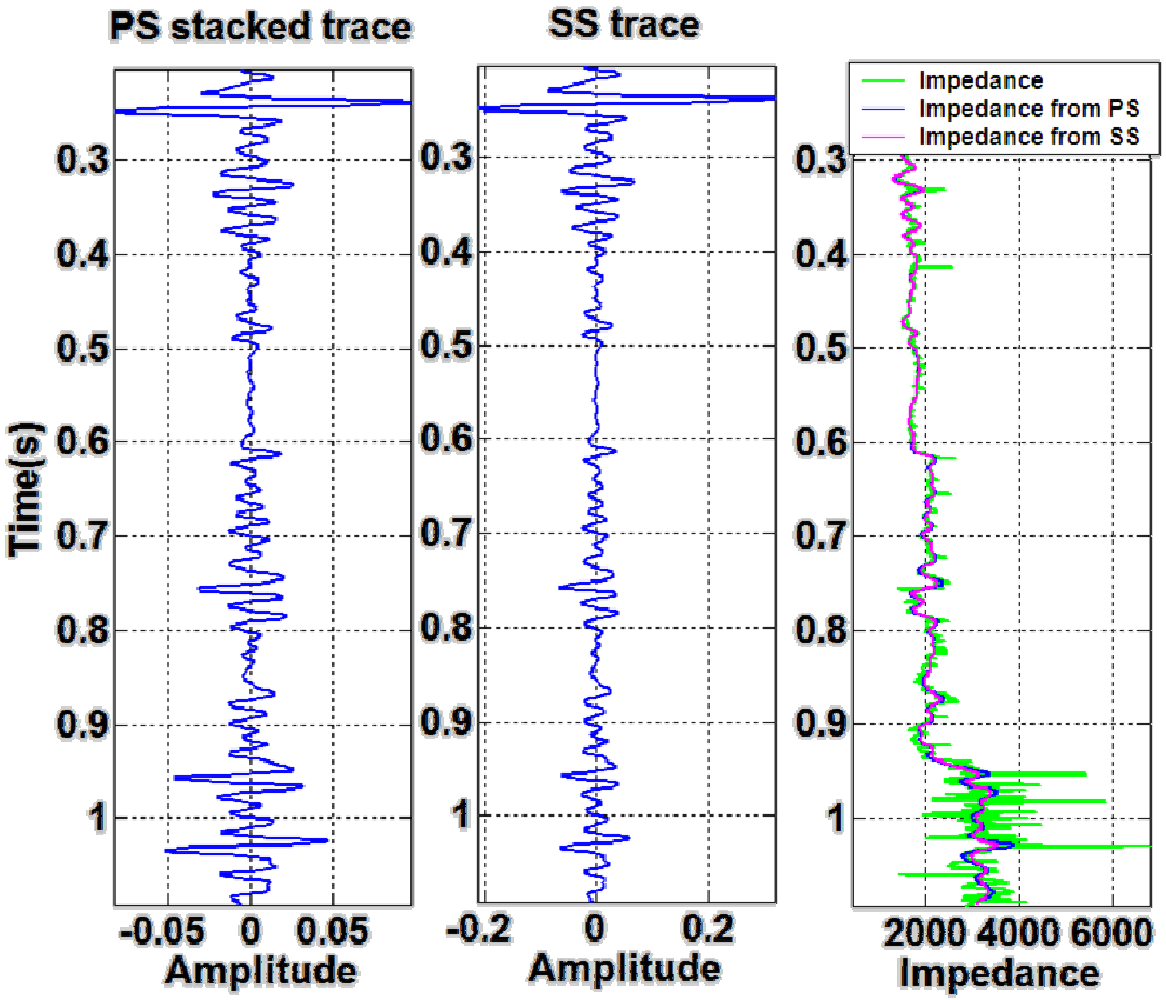

Figure 3.16: (a) PS reflectivity converted to (b) SS reflectivity using Stewart and Bland's (1997) expression, and (c) inverted impedance from the PS and SS traces.

3.3.2. Model-based inversion

Model-based inversion (Russell and Hampson, 1991) uses a generalized linear inversion algorithm (GLI) which attempts to modify the initial model until the resulting synthetic matches the seismic trace within some acceptable bounds. This method is effective when there is considerable knowledge about the geology and a reliable model can be created.

An initial model for this inversion approach was generated using the P-impedance logs calculated at the two well locations that had sonic logs available, filtered with a 10/15 Hz low-pass filter (Figure 3.17). P-impedances in the model range from 4000 to almost 8000 m/s*g/cm^3, and have a general increasing with depth trend. The 3D impedance volume is generated by interpolating the impedance at the well locations using two picked horizons above (~400 ms) and below the target zone (~ 600 ms).

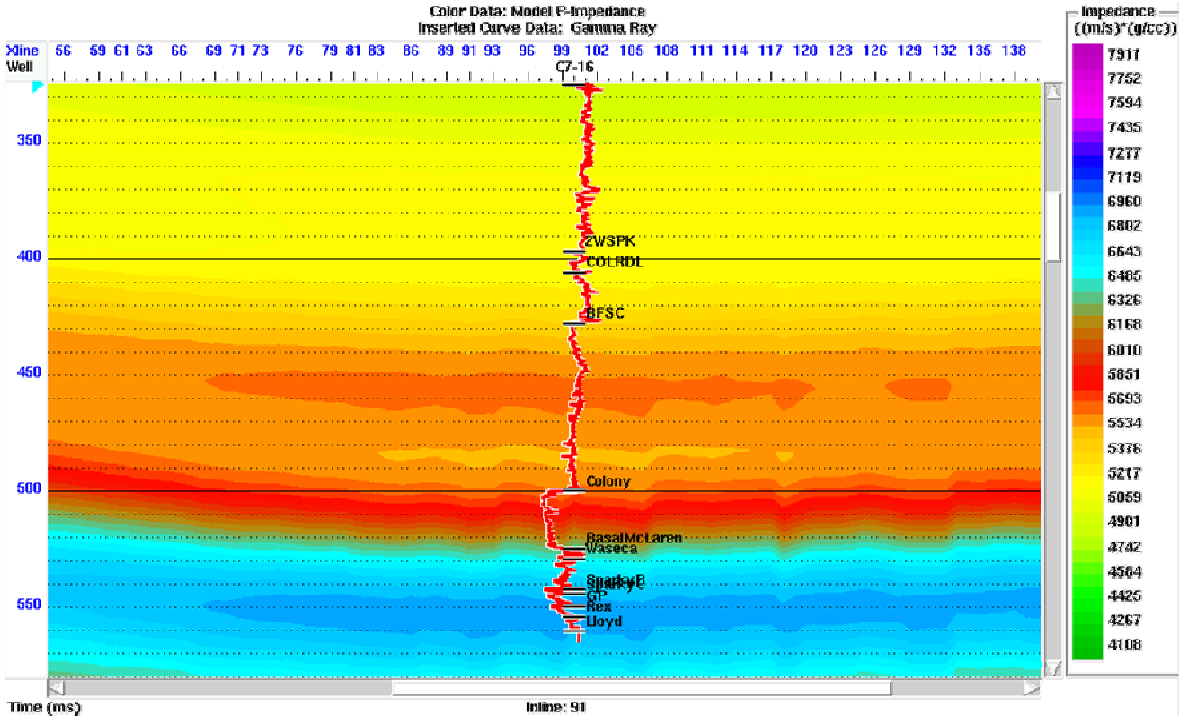

Figure 3.17: Initial low frequency P-impedance model for the model based inversion of the PP stacked volume along inline 91, with the GR log annotated at the location of well C07-16.

A post-stack inversion analysis was performed in the location of wells A11-17 and C07-16 to evaluate the accuracy of the inversion and to calculate amplitude scalars between the seismic data and the impedance at the well. P-impedance is inverted from a single trace at the well location, and then a synthetic trace generated using this impedance and the extracted PP wavelet is compared with the extracted trace from the PP seismic volume at

the well location (Figures 3.18 and 3.19). The correlation between the synthetic (red) and the seismic trace (black) looks very good in both wells, with correlation coefficitents of over 0.99 in both wells. The estimated error was 439.78 for well A11-17 and 956.82 for well C07-16, corresponding to 7 and 14 %, respectively. As mentioned previously, the inverted impedance is band-limited, and fails to reproduce the higher frequency variations observed in the wireline logs. Within the more uniform shaly interval the inversion estimates are very close to the actual impedance; meanwhile, within the Mannville interval the inverted impedance shows the general trend and relative variations. It is also important to remember that a lot of the intervals within the Mannville are below the seismic vertical resolution, in which case, the amplitudes of the seismic data could be significantly affected by tuning and interference effects from surrounding beds.

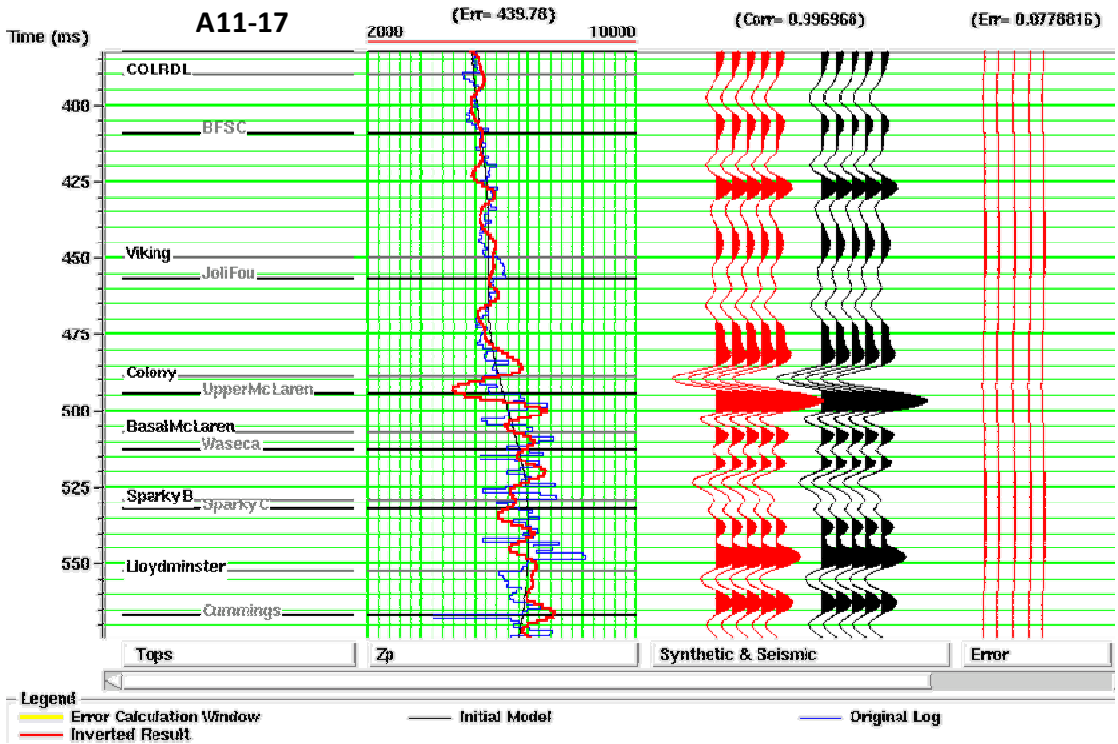

Figure 3.18: Analysis of the post-stack model-based PP inversion at wellA11-17. (a) P-impedance log (blue), initial P-impedance model (black), and inverted P-impedance (red). (c) syntethic trace generated from the inversion result (red) and extracted trace from the seismic (black).

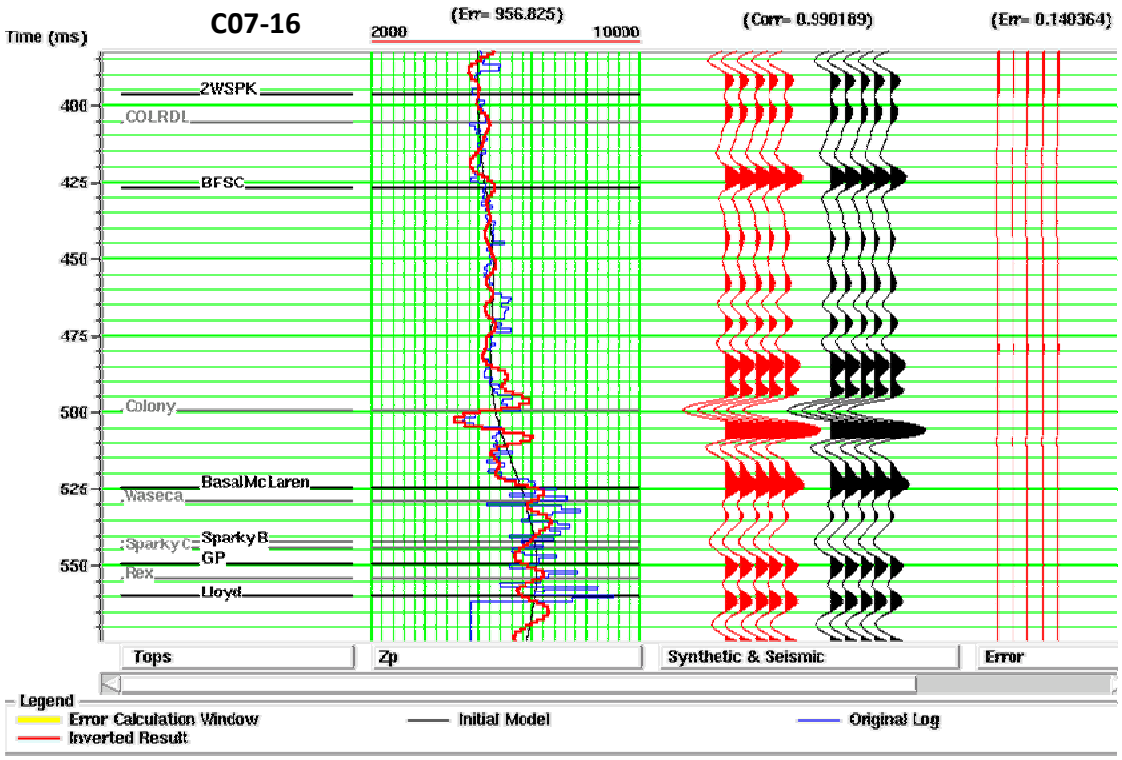

Figure 3.19: Analysis of the post-stack model-based PP inversion at well C07-16. (a) P-impedance log (blue), initial P-impedance model (black), and inverted P-impedance (red). (c) syntethic trace generated from the inversion result (red) and extracted trace from the seismic (black).

Following the analysis at the well locations, the model-based inversion was done on the PP volume using the extracted wavelet from the seismic data and a single value hard constraint of 50%, indicating that the initial model can be modified within a range of ± 50%. The inverted impedance shows zones of low impedance within the Mannville interval which can be correlated to the prospective reservoirs. At the Colony top in well C07-16 the lateral extent of the impedance anomaly could be indicating the edges of the sand channel (Figure 3.20), while at the Sparky interval the low amplitude anomaly is more continuous, suggesting the facies and/or fluid changes are less dramatic within this interval. Also note the lowest amplitude in the Mannville occurs in the interpreted gas zone in the Colony

sand, suggesting that the P-impedance could be showing the effect of the fluids more than of lithology.

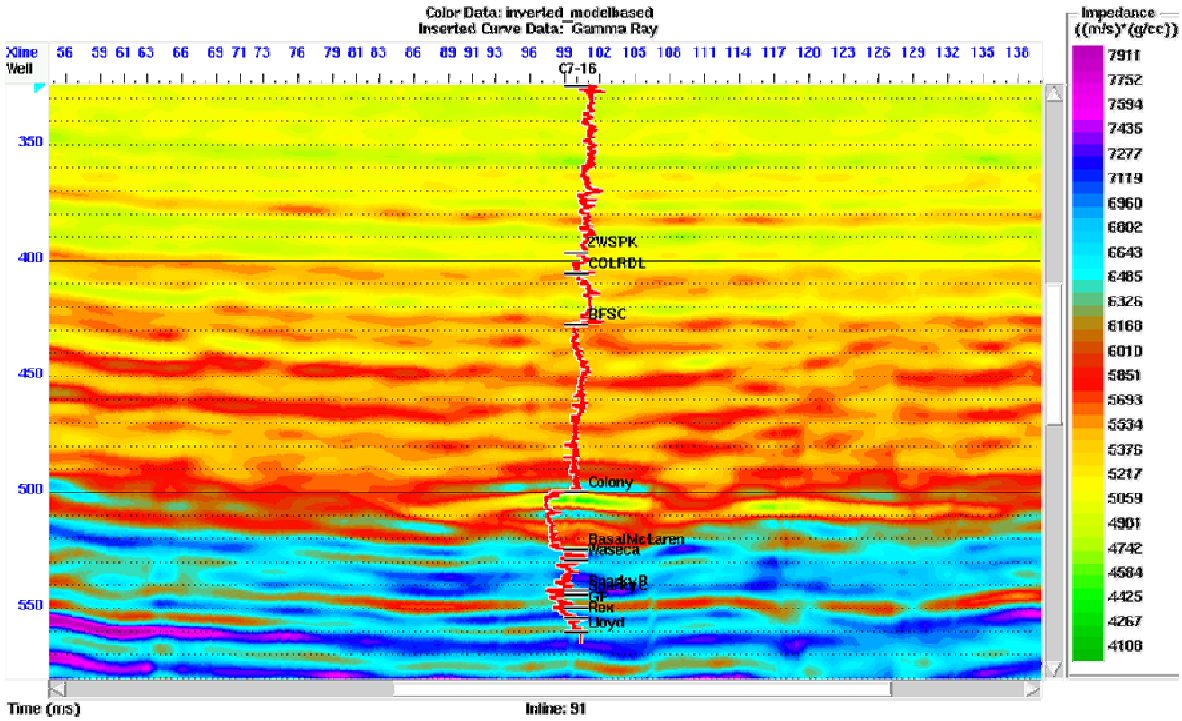

Figure 3.20: P-impedance inversion results for inline 100, showing the low impedance channel at the Colony level. GR log is annotated at the location of well C07-16.

Amplitude extractions from the PP seismic and the inverted impedance volume at the top of the Colony horizon (Figure 3.12) show low amplitude linear features which are generally interpreted as channel facies, and most of the wells drilled in the area are located within the channel trends. P-impedance values range from 5000 to 7000 m/s*g/cm^3. In this particular case, the impedance inversion does not seem to bring out any additional information.

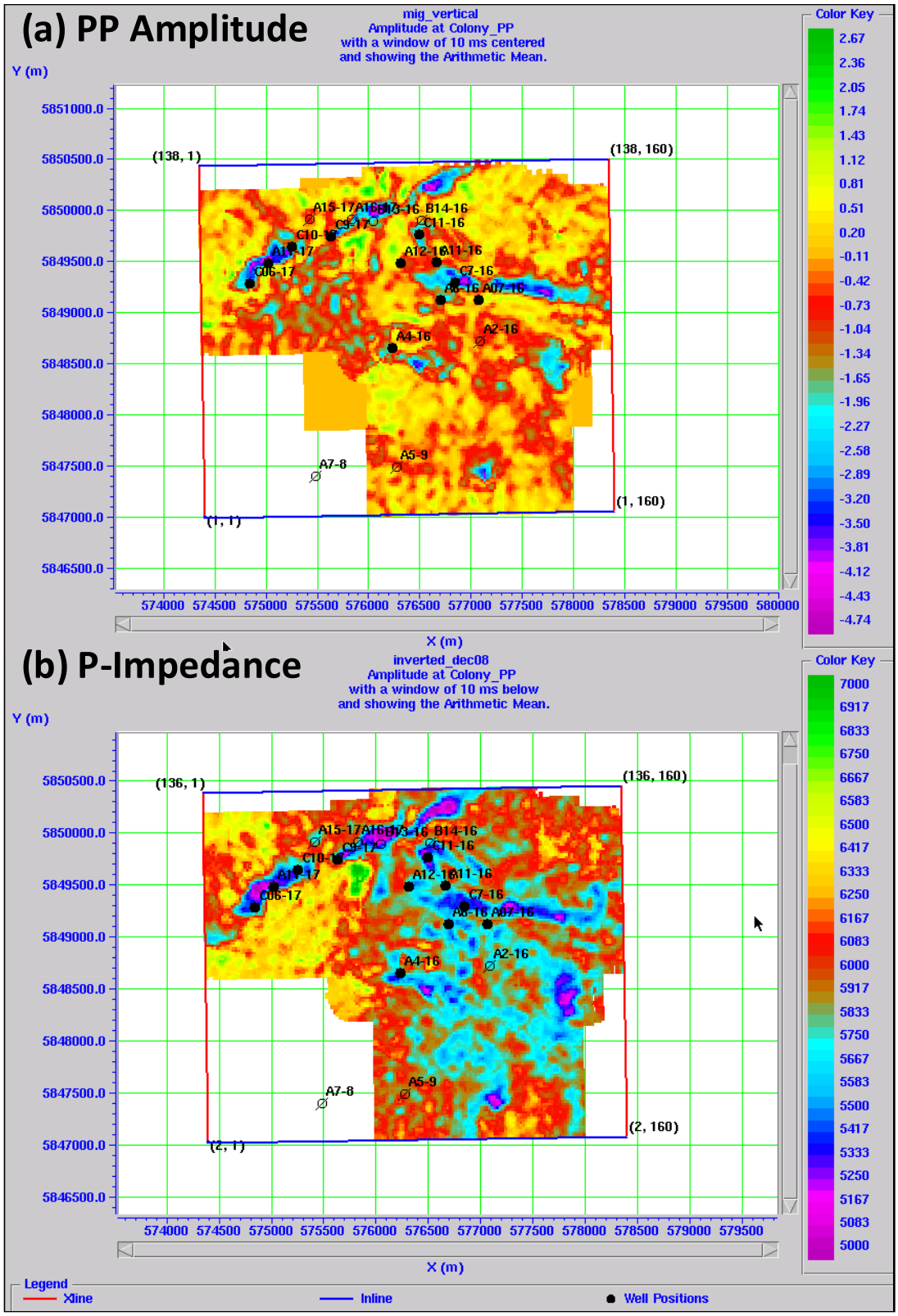

Figure 3.21: (a)Extracted amplitudes from the PP seismic volume at the Colony top, using a 10 ms centered window, (b) Extracted P-impedance from the model-based inversion of the PP volume, at the Colony top using a window of 10 ms below the horizon.

Following the PP inversion, a post-stack model-based inversion of the converted data set was evaluated. An initial S-impedance model was generated using the logs in well A11-17, which is the only one with a shear sonic available. It was extrapolated using the same horizons as those used for the PP initial model. The model has increasing S-impedance values ranging from 1500 to 3400 m/s*g/cm^3, with a sharp change occurring at the top of the Colony (Figure 3.22).

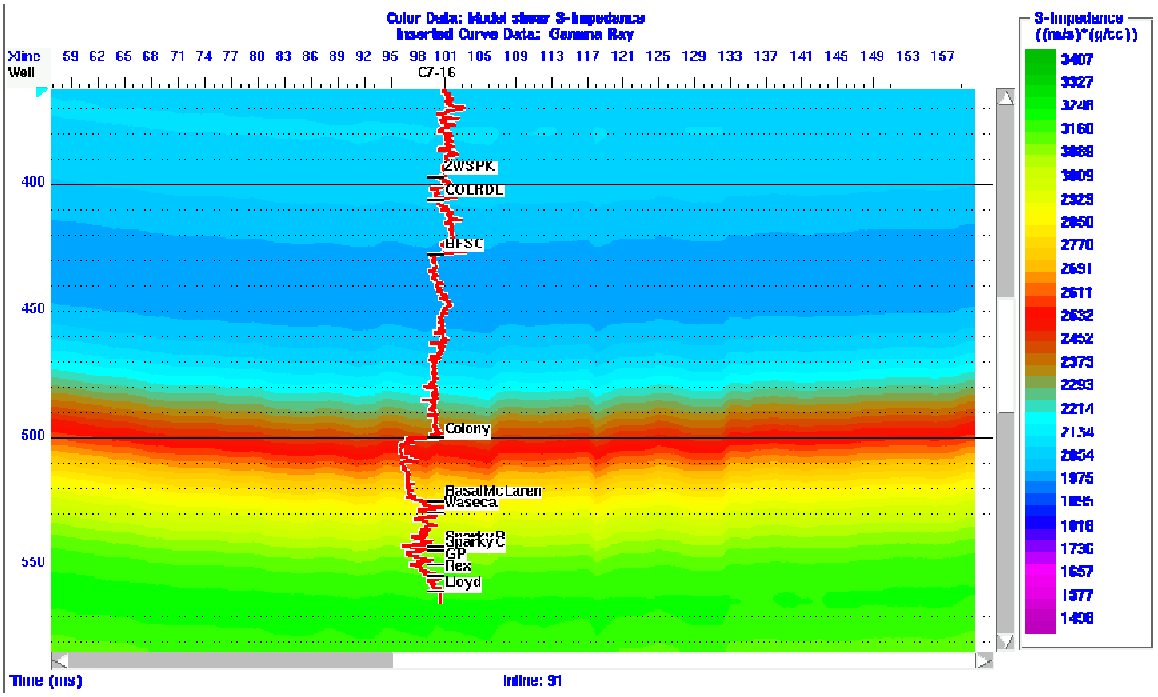

Figure 3.22: Initial S-wave impedance model for the model-based inversion of the PS seismic data. GR is annotated in red at the location of well C07-16.

The same inversion analysis was carried on at the well location (Figure 3.23), resulting in a correlation coefficient of 0.98 and an error of 279 m/s*g/cm^3, which corresponds to 18 %. Due to the lower frequency of the PS data, the inverted result has considerably less detail than the PP inversion,

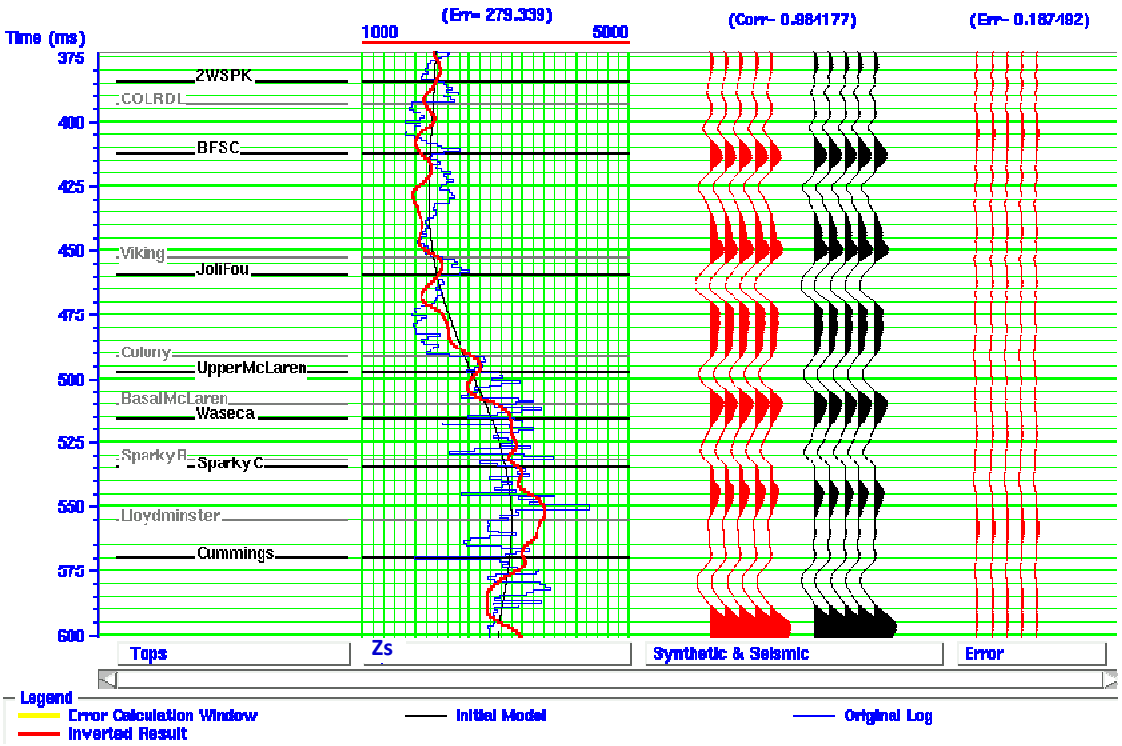

Figure 3.23: Post-stack inversion analysis of the PS seismic volume at well A11-17. (a) S-impedance log (blue), initial S-impedance model (black), and inverted S-impedance (red). (c) syntethic trace generated from the inversion result (red) and extracted trace from the seismic (black).

In this case, the inversion was performed using a soft constraint of 0.01, which lowers the weights given to the initial model, since the initial attempts using the hard constraint option resulted in inverted impedances very similar to those of the initial model. Overall, there is not a dramatic change in the inverted values with respect to the initial model, even with the lower weights, but some lateral variability is introduced in the model by the inversion (Figure 3.24). The initial model is made based on a 5/10 Hz bandpass on the well logs, and considering the converted-wave data has a dominant frequency of 18 Hz, it becomes evident why there are not significant changes in the inversion.

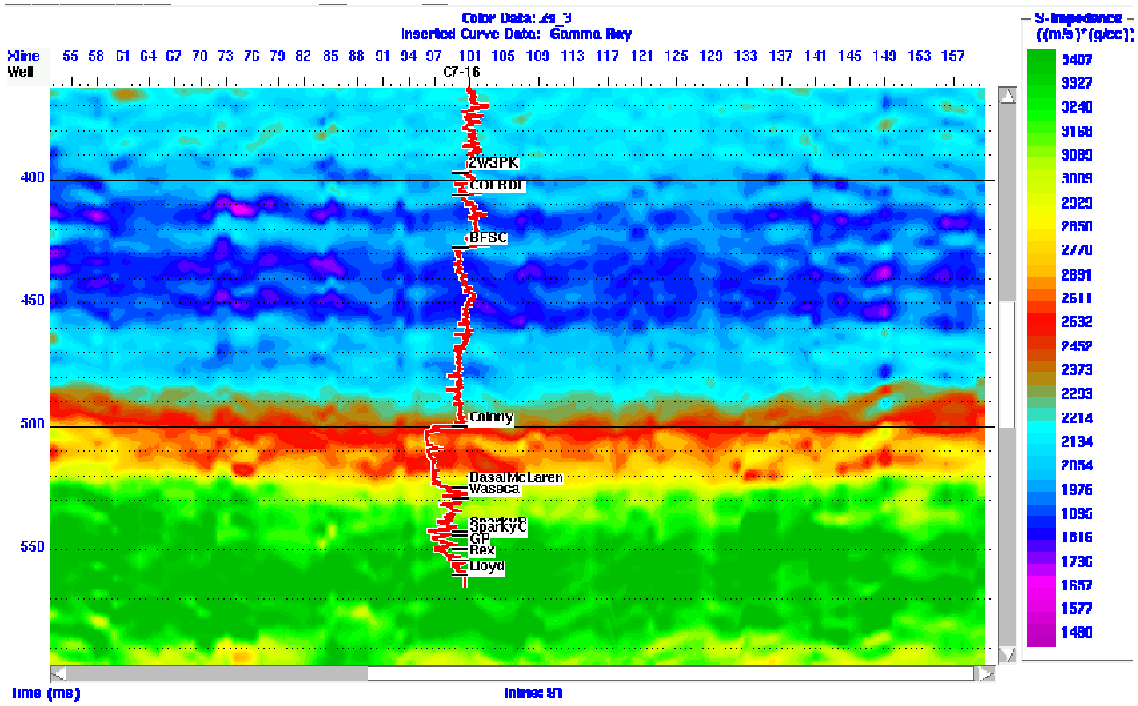

Figure 3.24: S-impedance estimate from the model-based inversion of the PS seismic volume. GR is annotated at the location of well C07-16.

The extracted S-impedance using a 20 ms window below the Colony horizons (Figure 3.25) shows a high amplitude linear feature that correlates with one of the interpreted channels in the PP amplitude map; however, only one channel feature is evident, in contrast with the two features seen in the PP map. It is also interesting to note how much noisier the PS data set is, probably due to static problems, which are harder to address in converted-wave data due t the very low S-wave velocities in the near-surface.

The joint interpretation of the PP and PS seismic volumes is hindered by the significantly different bandwidth of the two volumes, which affects the registration process and the subsequent interpretation of the generated maps.

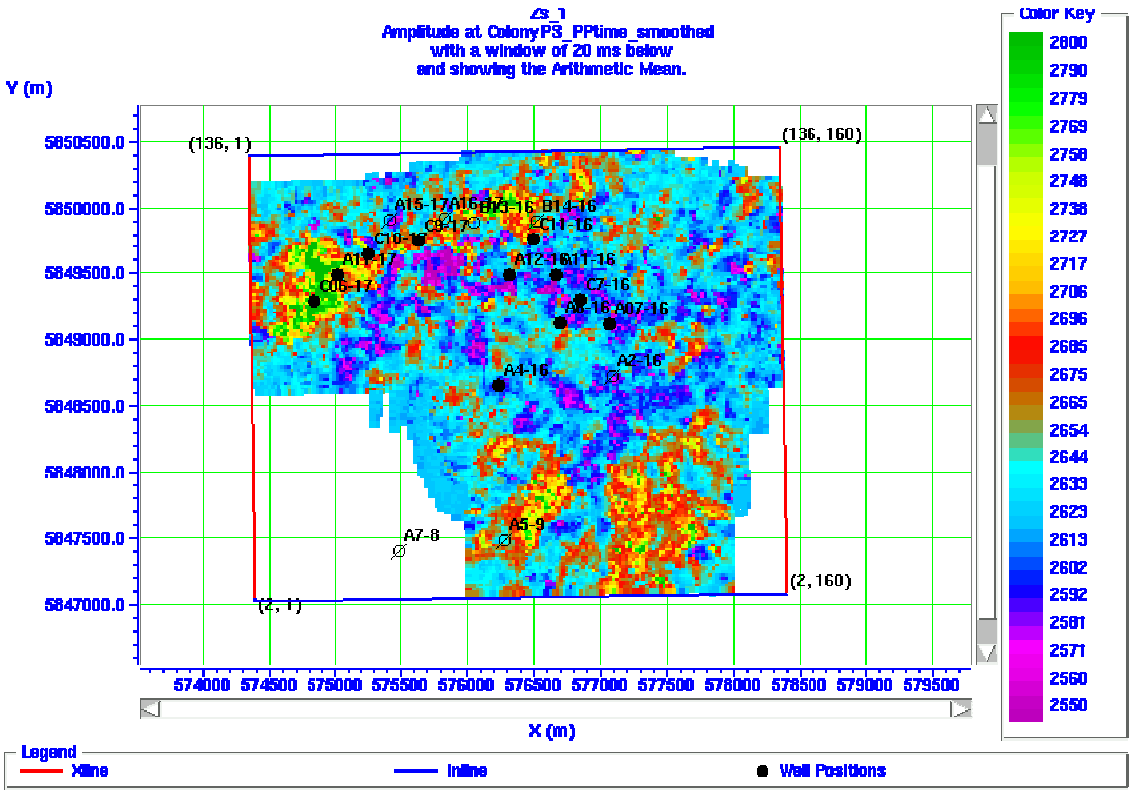

Figure 3.25: Amplitude extraction on the inverted S-impedance volume at the top of the Colony sand, using a window of 20 ms below the Colony horizon.

3.3.3. Residual from the mudrock line

The use of the mudrock line to estimate S-wave velocity from P-wave velocity was evaluated in Chapter 2, showing that it consistently underestimates Vs within the sand intervals. Based on this result, the results from the model-based inversion of the PP and PS seismic volumes are used to calculate a mudrock residual that could be used to differentiate lithologies. Both the inverted P- and S-impedances were converted to velocities assuming a constant density of 2 g/cm^3, in order to simplify the calculations The P-wave velocity estimate was then converted to S-wave by using the best fit equation defined in Chapter 2, and a residual was calculated by subtracting Vs minus the mudrock estimate. In this approach it is assumed that the density effects should be the same in the P- and S-impedance estimates, and they should not contribute to the estimated residual.

Positive residuals are associated with sands, while negative residuals are associated with shales. Figures 3.26 and 3.27 show the residual S-wave velocity along inlines 91 and 100, respectively, with the GR log annotated at the well locations. The residuals range from -500 m/s to 500 m/s, and there is a significant change evident at the top of the Colony interval. There is a good correlation between the sand and shale intervals interpreted from the GR log and the residual. Also note that the magnitude of the residual is consistent between the different sands in the Mannville interval, unlike the P-impedance inversion results, which shows a very low impedance zone at the top of the Colony, and higher values in the deeper sands, as the P-impedance is also showing the effect of the saturating fluid.

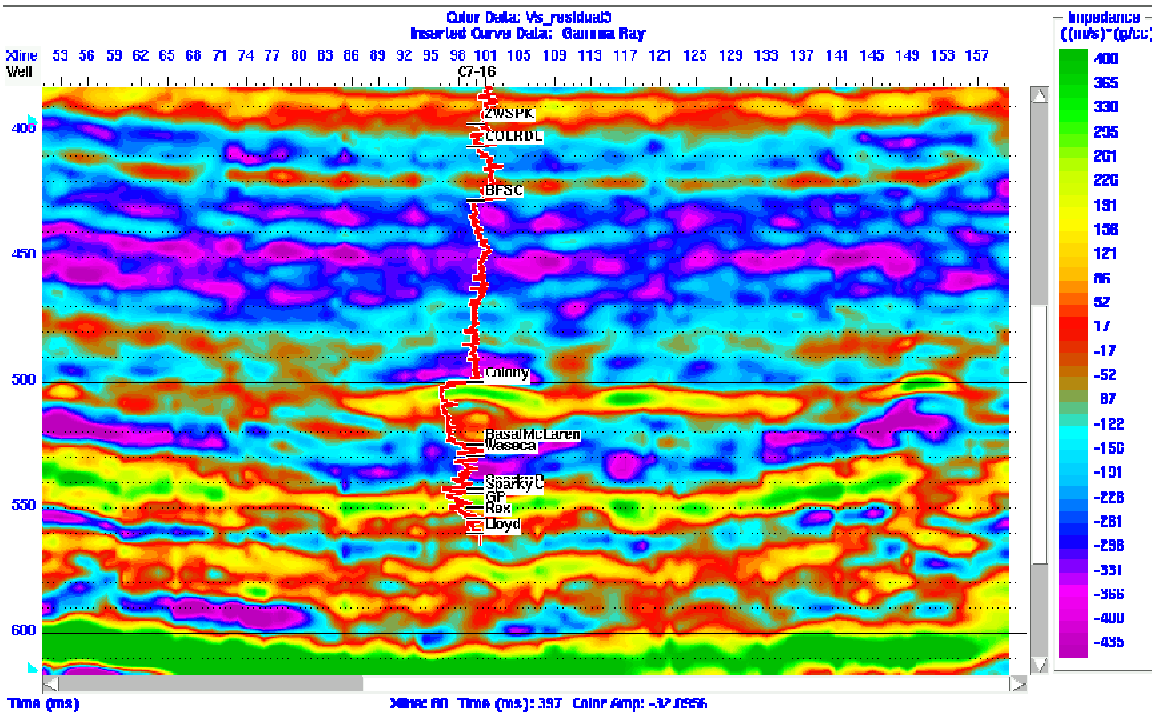

Figure 3.26: Residual from the mudrock line along inline 91, showing the GR log annotated at the location of well C07-16.

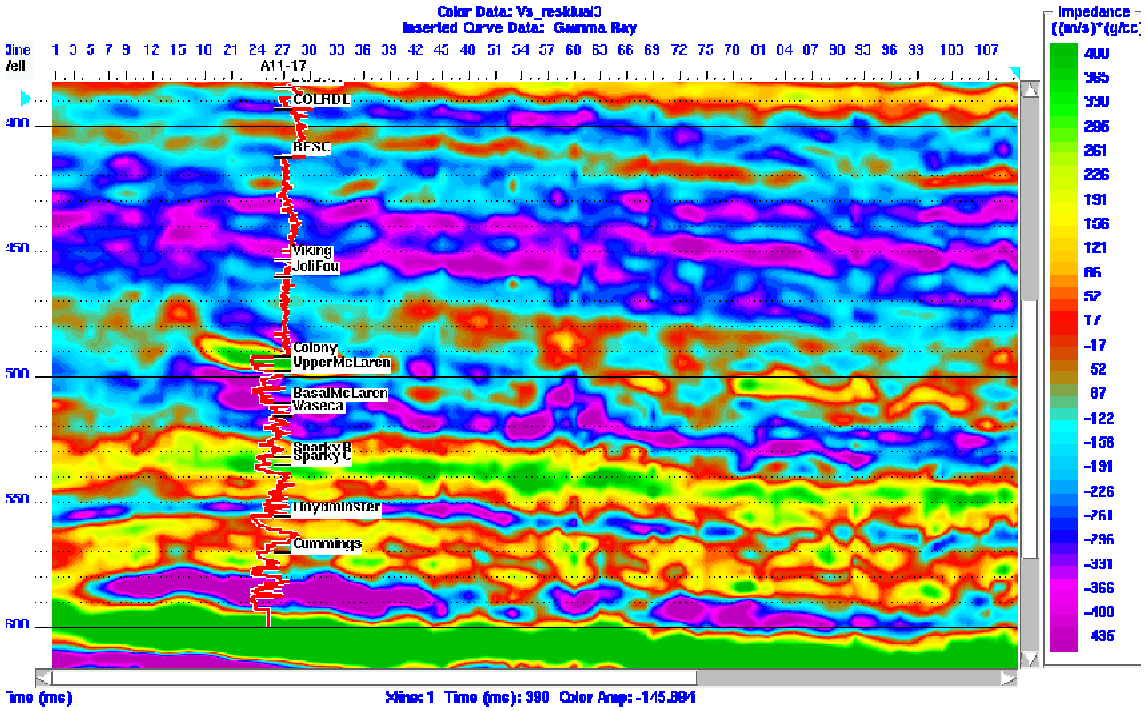

Figure 3.27: Residual from the mudrock line along inline 100, showing the GR log annotated at the location of well A11-17.

The amplitude extraction of the residual along the Colony horizon (Figure 3.28) shows the same trend as the PP amplitude map, which appears to indicate that the P-impedance results are the major factor controlling the residual. An improvement with respect to the P-impedance inversion results appears to occur in the deeper intervals, such as the Sparky and the Lloydminster, which did not appear as areas of low impedance in the PP inversion result, but have high Vs residual, indicative of sands.

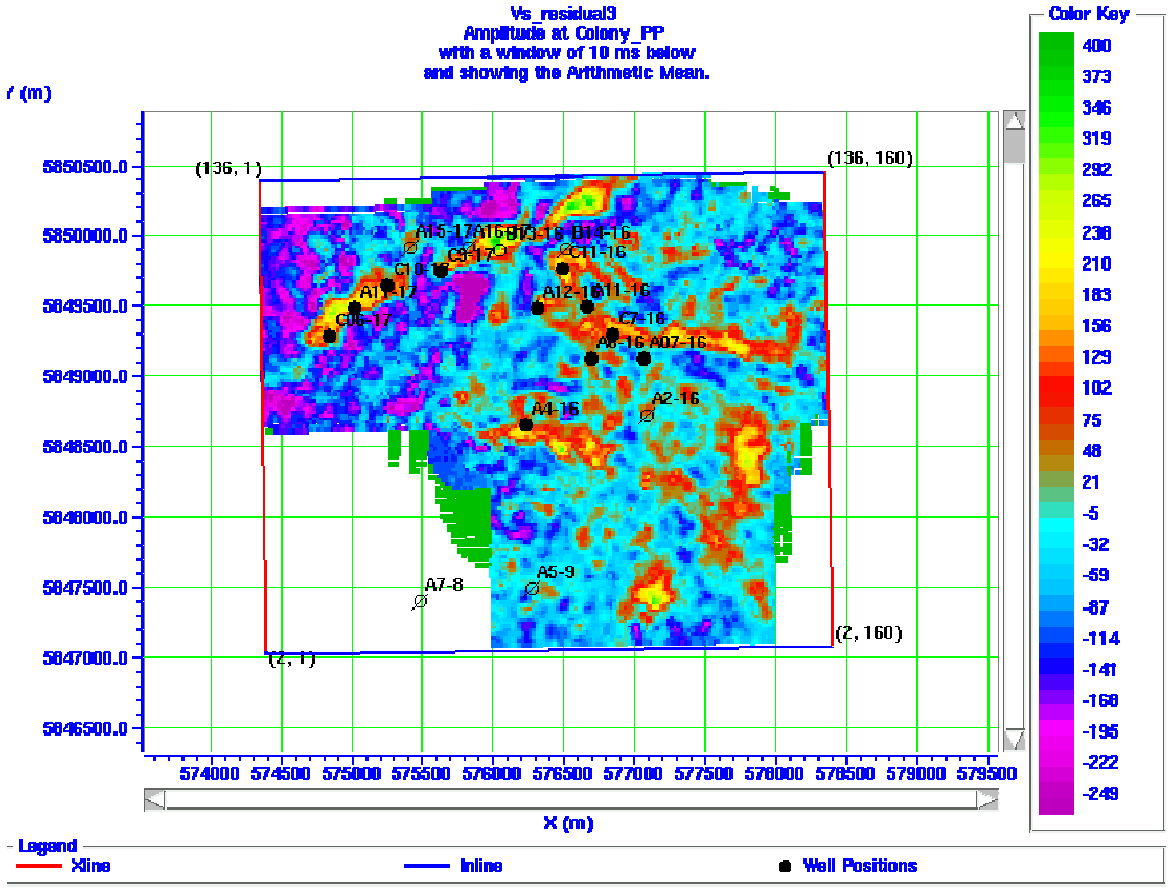

Figure 3.28: Vs residual extracted along the Colony horizon using a 10 ms window below the horizon.

3.3.4. Density estimations

In this section we evaluate density estimates from impedance estimates from the inversion of synthetic PP and PS traces evaluated in section 3.3.1.

The first approach is to use Gardner's and Lindseth's relation to estimate density from the inversion of a PP synthetic trace. To calculate density from impedance it is necessary to know the velocity model. In this case, the density-velocity relations evaluated previously will be used to estimate density. Assuming Gardner's relation is valid, the expression for velocity in terms of density is:

$$V = \left(\frac{\rho}{a}\right)^{\frac{1}{m}}, \tag{3.3}$$

and substituting this equation into $I = \rho * V$ and solving for density results in:

$$\rho = \left(aI^{m}\right)^{\frac{1}{m+1}} \tag{3.4}$$

Using Lindseth's equation, velocity is expressed in terms of density as:

$$V = \frac{d}{1 - c\rho}, \tag{3.5}$$

and substituting into equation 2 and solving for density:

$$\rho = \frac{I}{d + cI}. \tag{3.6}$$

Using equations 3.4 and 3.6, densities were estimated from the estimated impedance from the band-limited inversion of the PP synthetic traces for each well (See Figure 3.29), using the coefficients for sands and shales previously determined. In general, the estimated impedance is smoother than the impedance from the log, and as a consequence the density estimates are also smoother than the actual density. The estimated densities follow the general trend of the density log, but some error has been introduced by the used of the lithology constraints and the application of Gardner's rule. Note that up to 0.5 s the inverted and original impedance are very similar, but the inverted and original densities start to show some noticeable deviations.

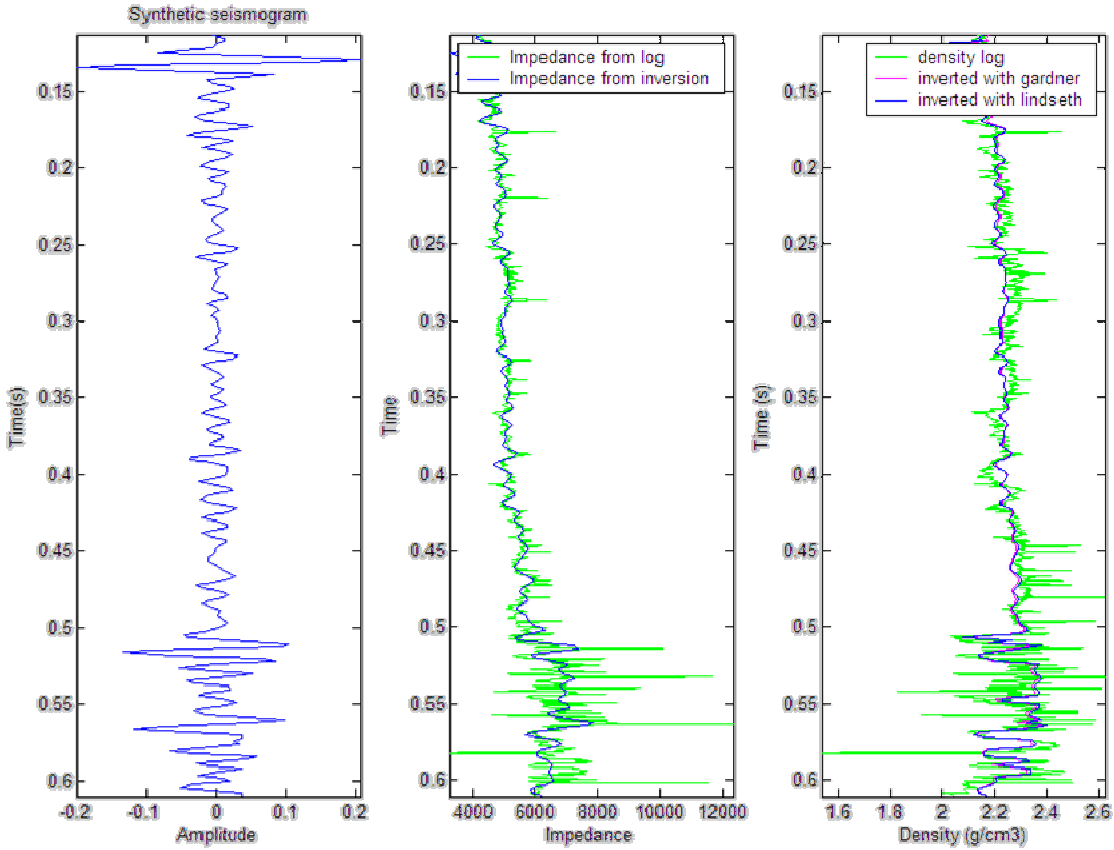

Figure 3.29: Density estimated from the inversion of the impedance log using Gardner's and Lindseth's relations with the coefficients for sand and shale.

The following approach involves using the inversion of the PS trace, and the Vs estimates from the log response equation to calculate density. Figure 3.30 shows the PS stacked trace, the resulting S-impedance inversion, and the corresponding density estimates when using the actual Vs log and the modelled Vs log. Even in the case of using the actual Vs log to estimate density, there are some errors included in the estimation just because of the band-limited character of the seismic. In the case when the modelled shear-wave velocity is used significant errors are brought into the density estimates.

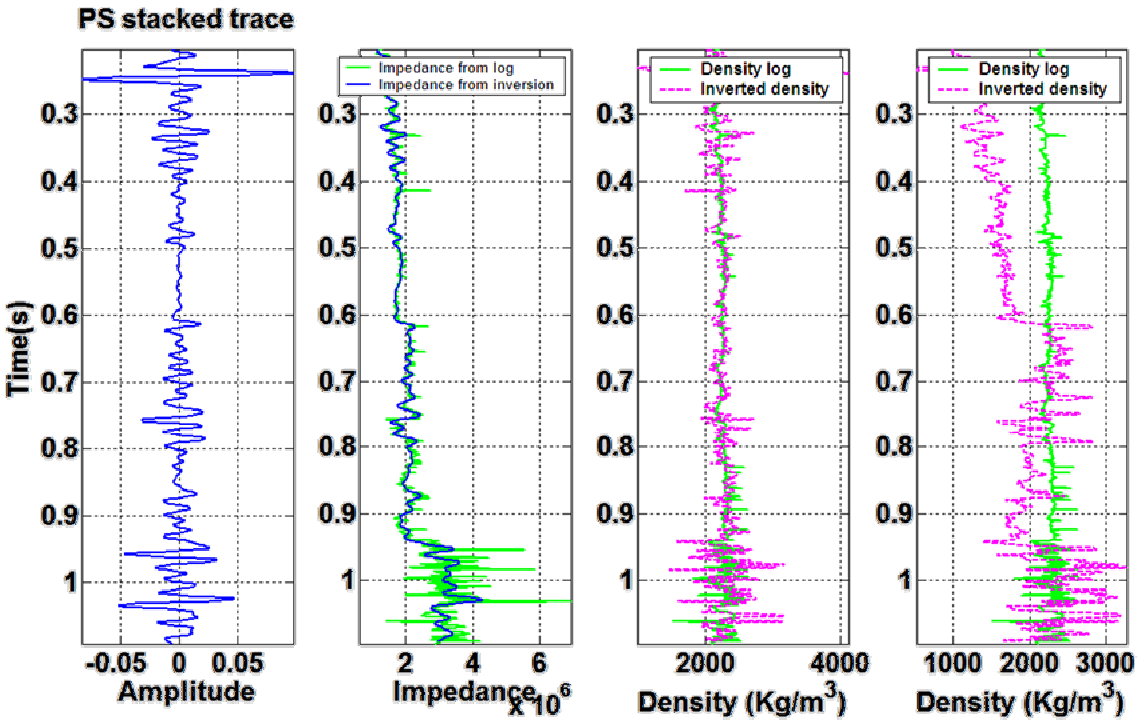

Figure 3.30: Impedance and density estimates from the inversion of a synthetic PS stacked trace. (a) PS stacked trace, (b) Inverted PS impedance, (c) inverted density using correct S-wave velocity log, and (d) inverted density using S-wave velocity log modelled using the log response equation.

CHAPTER FOUR: LOG ANALYSIS IN THE ASSAM PROVINCE, INDIA.

4.1. INTRODUCTION

Elastic properties and rock properties were analyzed using well logs from two wells in the Assam province in India, to evaluate the feasibility of using multicomponent seismic to enhance interpretation in the area (Stewart et al., 2008). The motivations for acquiring multicomponent (especially, converted P-to-S) seismic data are several-fold, including: improvement of the P-wave sections (via multicomponent filtering techniques), developing new structural details (faults, compartments, closures) using PS images, assisting with defining new stratigraphic features and providing some large-scale lithology (e.g., sand versus shale) information, and help in providing information about fluid distributions.

The following sections show a review of the geology and stratigraphy of the Assam province, followed by the analysis of the wireline data available from two wells in the area, to determine the variations in the elastic properties between reservoir and non-reservoir rocks, and finalizing with the generation of PP and PS synthetic seismograms, to evaluate the additional information that could be attained using multicomponent data for the exploration efforts in this area.

4.2. GEOLOGIC SETTING

The Upper Assam basin represents a structurally warped foreland basin between two convergent margins (Mathur et al., 2001). Near-shore to shallow marine conditions prevailed during a major part of the Cretaceous and early Paleogene, as well as during the early and Middle Eocene, changing to deltaic-estuarine conditions during the latter part of

the Eocene and Oligocene, and followed by a fluvial setting in the Miocene and younger times (Mathur et al., 2001).

The general stratigraphy of the Assam shelf is shown in Figure 4.1. The oldest rocks within the basin are Upper Cretaceous and correspond to continental and lagoonal sandstones and interbedded shales of the Dergaon and Disang Formations. These formations are unconformably overlain by over 250 m of massive sandstones of the Tura and Langpar Formations within the Jaintia Group, deposited in a fluvial to marginal marine environment during Paleocene and Eocene times. The overlying Eocene Sylhet Formation is subdivided into the Lakadong, Narputh and Prang members. The basal part of the Lakadong member constitutes more than 350 m of thin sandstones and interbedded shales and coals, deposited in a lagoonal environment. The middle Lakadong consists of thick sands deposited in a strand plain or barrier bar environments, while the upper Lakadong is a calcareous sandstone of restricted shallow water platform (Mathur et al., 2001). The overlying Narputh member consists of claystones and siltstones of a shelf environment, while the Prang member is a shelf carbonate with interbedded siltstones and clay. The Sylhet formation thickens towards the southeast due to contemporaneous platform tilting and basement sourced block faulting.

Unconformably overlying the Sylhet is the Eocene Kopili formation, with as much as 500 m of shallow marine to lagoonal shales and interbedded limestones. The Eocene and Oligocene Barail group comprises as much as 900 m of sands with minor shales deposited in a delta front environment, and as much as 1,200 m of interbedded coals, shales and discontinuous sandstone reservoirs from delta plain environment. The overlying Surma Group is missing on much of the Assam shelf. It is typified by a series of thin siltstones, sandstones and shales deposited in fluvial deltaic to estuarine environments.

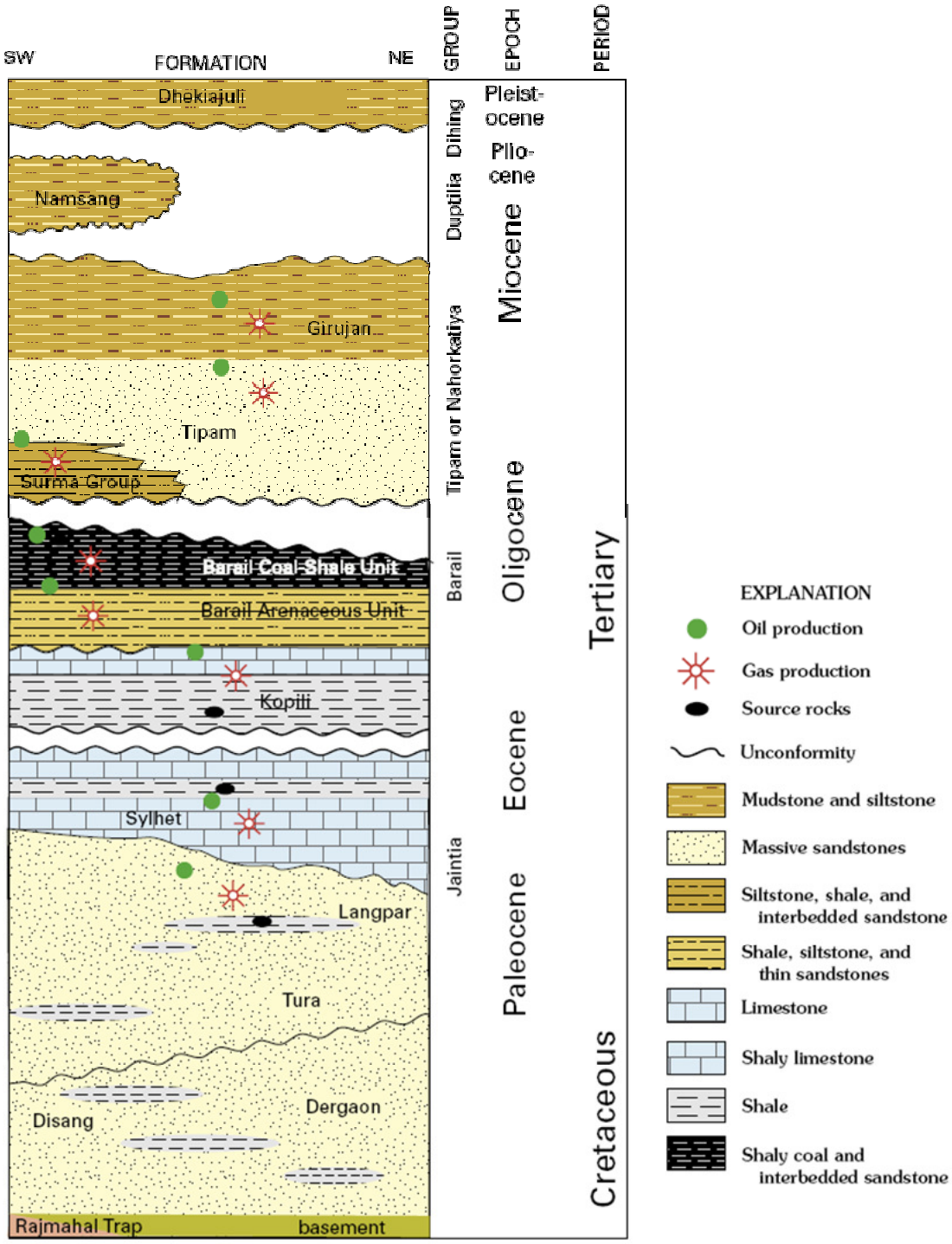

Figure 4.1: Generalized stratigraphy of the Assam shelf, India (From Wandrey, 2004)

The Lower Miocene Tipam Formation sandstone is largely of fluvial origin and the heavy mineral content of the unit indicates derivation from the rising Himalayas, with

depositional transport towards the south (Mathur et al., 2001). The overlying Girujan formation consists consists of more than 1300 m of mottled clays containing minor sandstone lenses (Wandrey, 2004) deposited in a lacustrine to fluvial environment. It is unconformably overlain by poorly consolidated fluvial sandstones with interbedded clay and lignite of the upper Miocene Namsang Formation. Quaternary strata in the upper Assam shelf thicken north, where it can exceed 2000 m.

Most hydrocarbon production in the area comes from units above the Oligocene unconformity, mainly from the Barail group and Tipam formation, with quite productive reservoirs found in the Barail and Tipam sandstones, with permeabilities ranging from less than 7 mD to 800 mD, and porosities up to 30%. However, more recent discoveries have been found in the near shore upper Paleocene-lower Eocene clastic sequence, with Eocene reservoirs constituting more than 50 % of crude oil production by Oil India Limited (Mathur et al., 2001).

4.3. LOG ANALYSIS AND ELASTIC PROPERTIES

A detail of the suite of logs from well A in the Hapjan field, and well B in the Deohal field is shown in Figures 4.2 and 4.3. Significant variations in the GR log, due to the complex stratigraphy of the area where the sand intervals are interbedded with shales and coals, difficult the identification of the better reservoir sections. The SP log is considerably less variable and appears to give a better indication of the good quality sandier intervals. Note that there are distinct S-wave velocity (V_s) anomalies in the Barail sands, with V_s generally increasing and deviating from the P-wave trend where sand content increases.

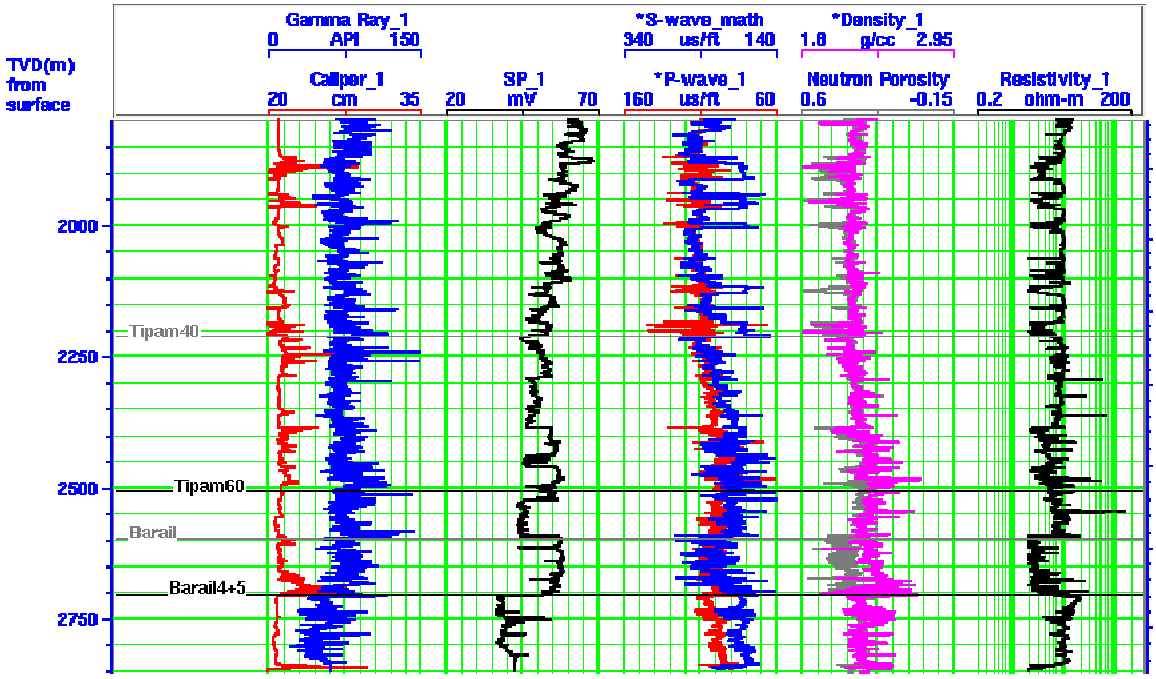

Figure 4.2: Detail of the logs within the reservoir interval for well A (Hapjan field). Note separation between the P-and S-wave sonics at the top of the productive Barail4 & 5 interval.

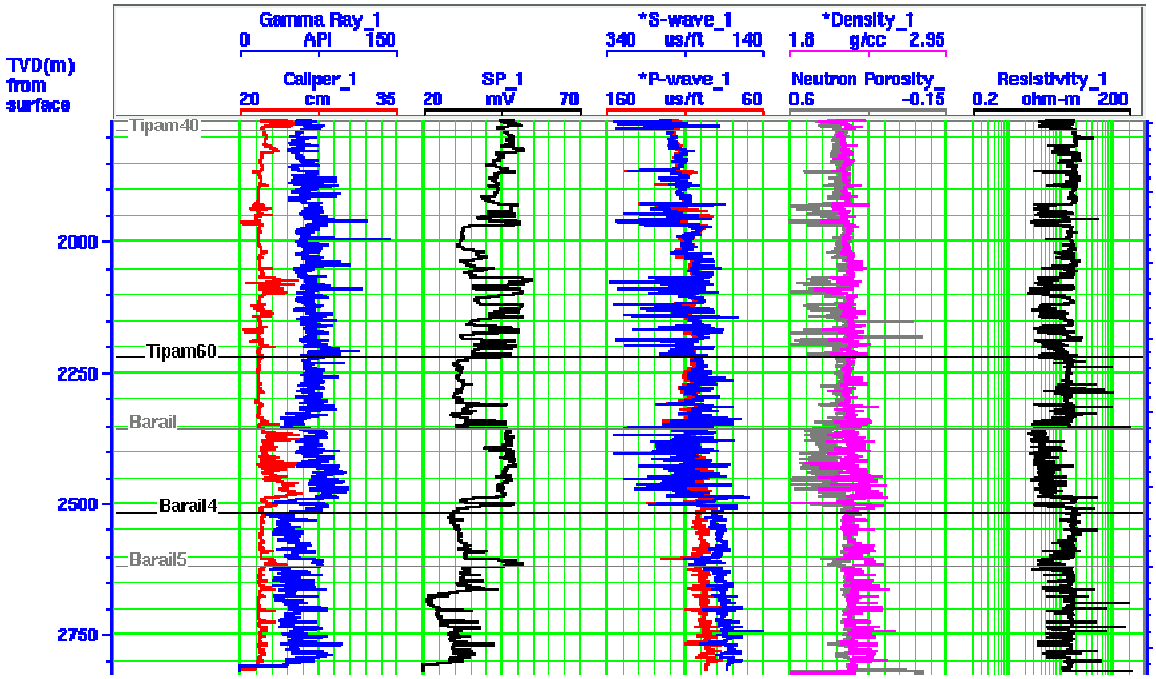

Figure 4.3: Detail of the logs within the reservoir interval for well B (Deohal field). Note separation between the P-and S-wave sonic logs at the top of the productive Barail4 interval.

Dipole sonic logs from well A show little difference between fast and slow shear waves, suggesting small azimuthal anisotropy at this location. However, the area does have faulting and fracturing, so on a larger scale azimuthal anisotropy may be present. With the vertically layered strata, we would expect some vertical transverse isotropy or variations of seismic velocity with angle from the vertical.

In general, good sands are indicated by a lowered SP, low gamma ray (~50 API), 30% porosities, lowered densities, resistivities between 10 and 20 ohm-m, and high S-wave velocities. The sands generally plot (on a V_p versus V_s chart) below $V_p/V_s=2$ (Figure 4.4).

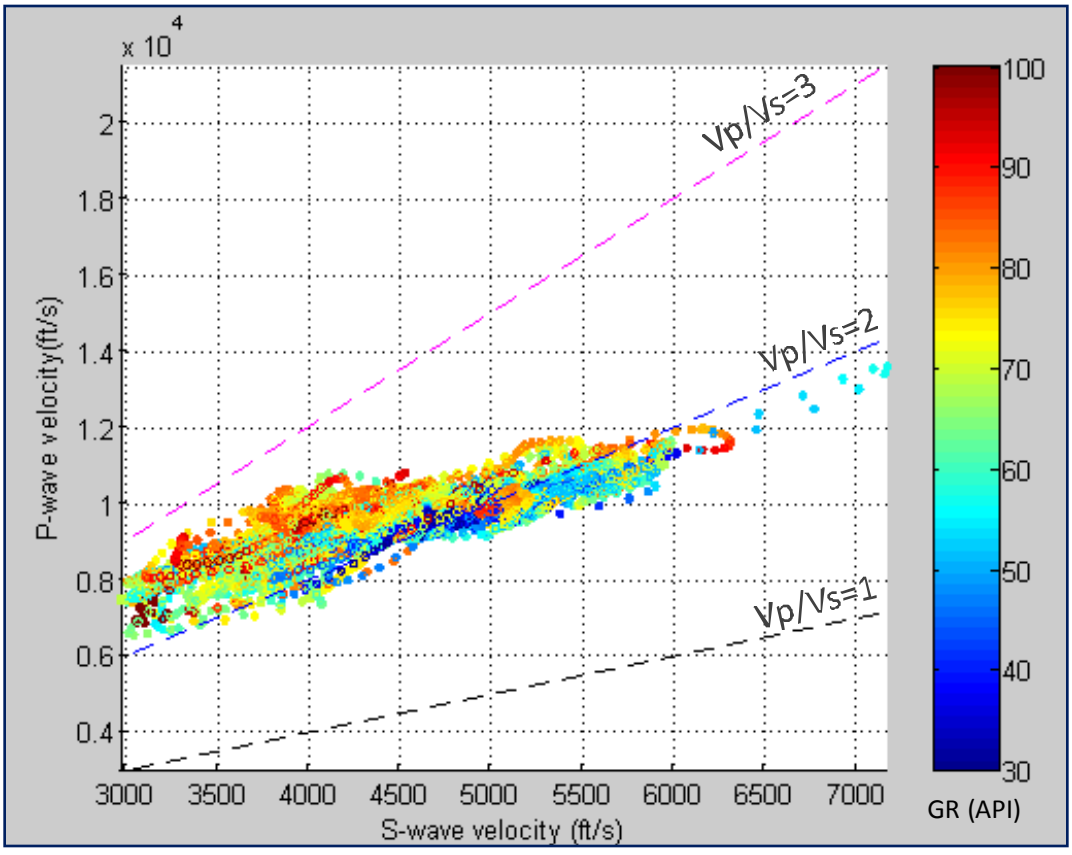

Figure 4.4: P- versus S-wave velocity crossplot for well B showing lines of constant V_p/V_s. Colorbar indicates GR values.

A density-porosity log was calculated using default sandstone parameters, with a matrix density of 2.65 g/cc and a brine density of 1.09 g/cc, showing a slight crossover of the neutron and density porosity at the top of the Barail4 and 5 intervals on well B, indicating a gas cap might be present. Neutron and density porosity crossovers are not necessarily associated with gas effects in the area. Mallick et al. (1997) attributed these anomalous crossovers to the lower density of amorphous silica relative to quartz in the reservoir sand, and concluded that the density-neutron crossover should only be used to identify sands within comparatively clean sandstone reservoirs. This problem can be partially resolved by changing the matrix convention used to calculate the porosity logs from limestone scale (2700 kg/m^3) to actual matrix scale (2550 kg/m^3). In general, for oil-bearing zones the crossover magnitude is less than three porosity units in the actual matrix scale, compared with more than 6 porosity units on the limestone scale, with crossover being greater than six for gas-bearing zones in the actual matrix scale (Borah et al., 1998)

We are searching for properties and their values that will isolate the sands of interest. In Figure 4.3, we see that the sands of interest (as indicated by low gamma ray values and high resistivity), have fairly high S-wave velocities, average P-wave velocities, V_p/V_s values around 2, and somewhat lowered densities (2.15 – 2.3 g/cm^3). In general, crossplots from different wells show that good sands are indicated by $V_p/V_s \leq 2$, V_s in the range between 1400 and 1800 m/s, V_p between 2650-3300 m/s, densities between 2.15-2.35 g/cm^3, and high resistivities.

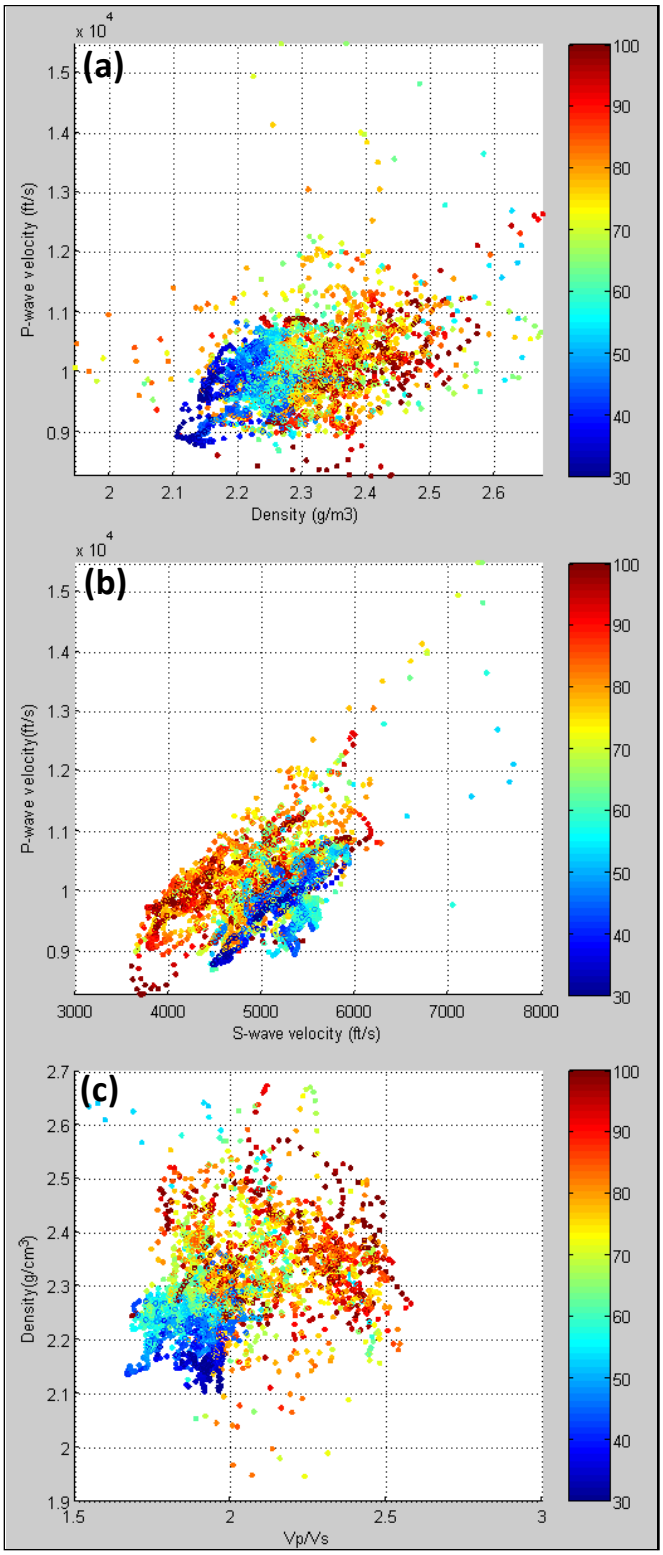

Figure 4.5: Crossplots for well A within the reservoir interval (2500-2800 m). (a) Density versus Vp, (b) Vp versus Vs, and (c) density versus Vp/Vs. Color bar indicates GR values

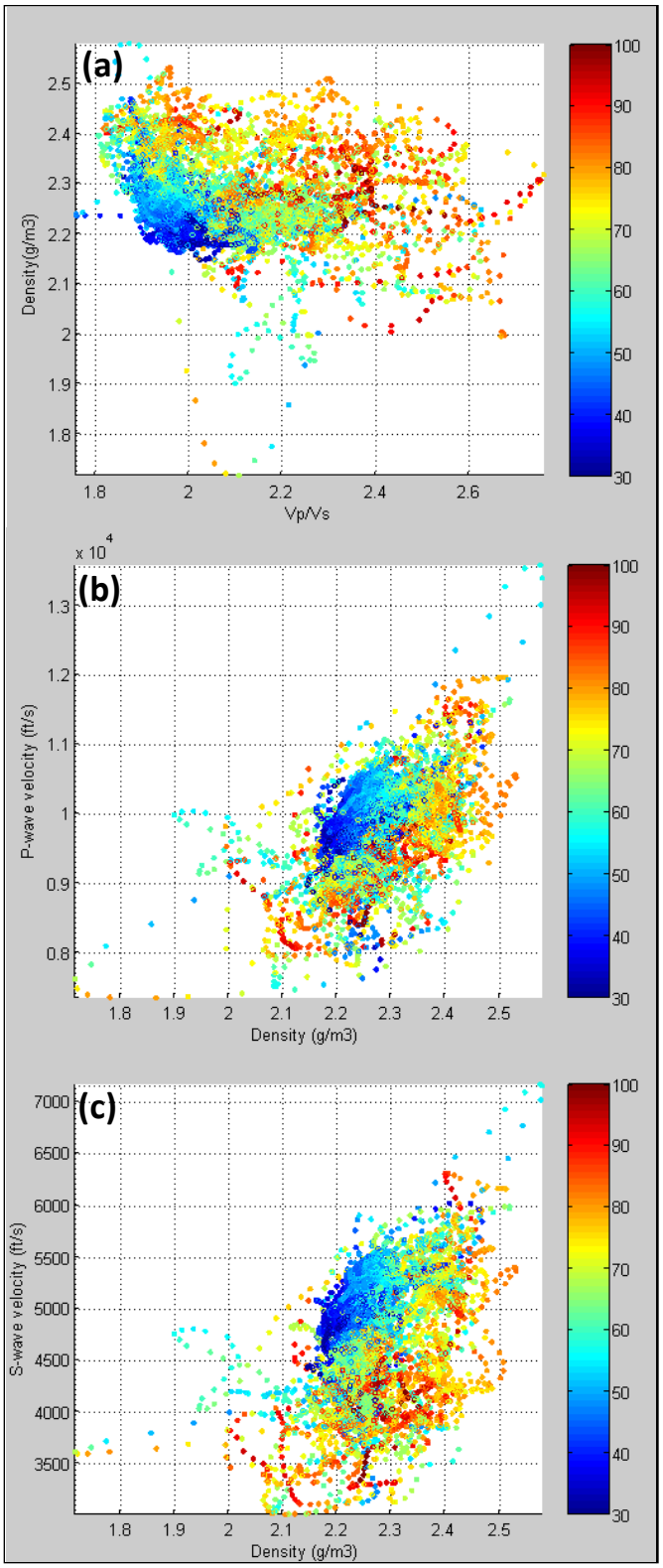

Figure 4.6: Crossplots for well B from 2200-2800 m depth. (a) Density versus Vp, (b) Vp versus Vs, and (c) density versus Vp/Vs. Color bar indicates GR values.

4.3.1. Modelling using the mudrock line

Well A was used to evaluate the accuracy of using the mudrock line to predict shear-wave velocity. In Chapter 2, it was noted that the mudrock line consistently underestimated shear-wave velocities in the sand intervals in the Manitou Lake area. The geology in the area of well A is not significantly different than that seen in the Mannville interval at Manitou Lake, consisting of clastic deposition within a fluvial setting, with sporadic coal intervals. However, in the Assam province the reservoir intervals are considerably deeper than in the Manitou Lake area. The crossplot between Vp and Vs in Well A shows significant dispersion from a single line (Figure 4.7), however, it is possible to note that the cleaner intervals, as identified by low GR values, fall below the mudrock line.

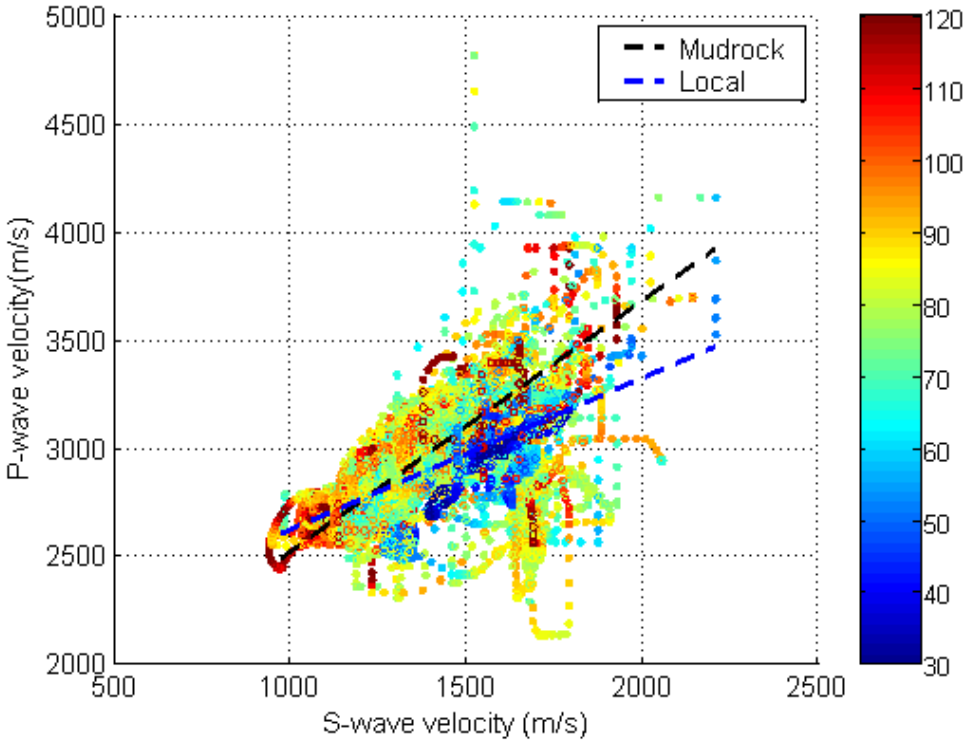

Figure 4.7: Vp versus Vs crossplot for well A. Colorbar indicates GR values. Dashed black line shows the general mudrock line, while the dashed blue line shows the best fit line to the data.

The mudrock line and the best fit line were used to estimate Vs from Vp in Well A, and a residual between the original Vs log and the predicted log with the mudrock line was also calculated (Figure 4.8). In this well the reservoir interval corresponds to the Barail4 and Barail5 intervals, indicated by the cleaner intervals in the GR at approximately 2700 m depth. Note the same type of response occurs at the top of the reservoir interval as in the Manitou Lake area, with a sharp increase in the residual at the top. Other sections that show positive residuals seem to correlate with areas of questionable S-wave velocity measurements.

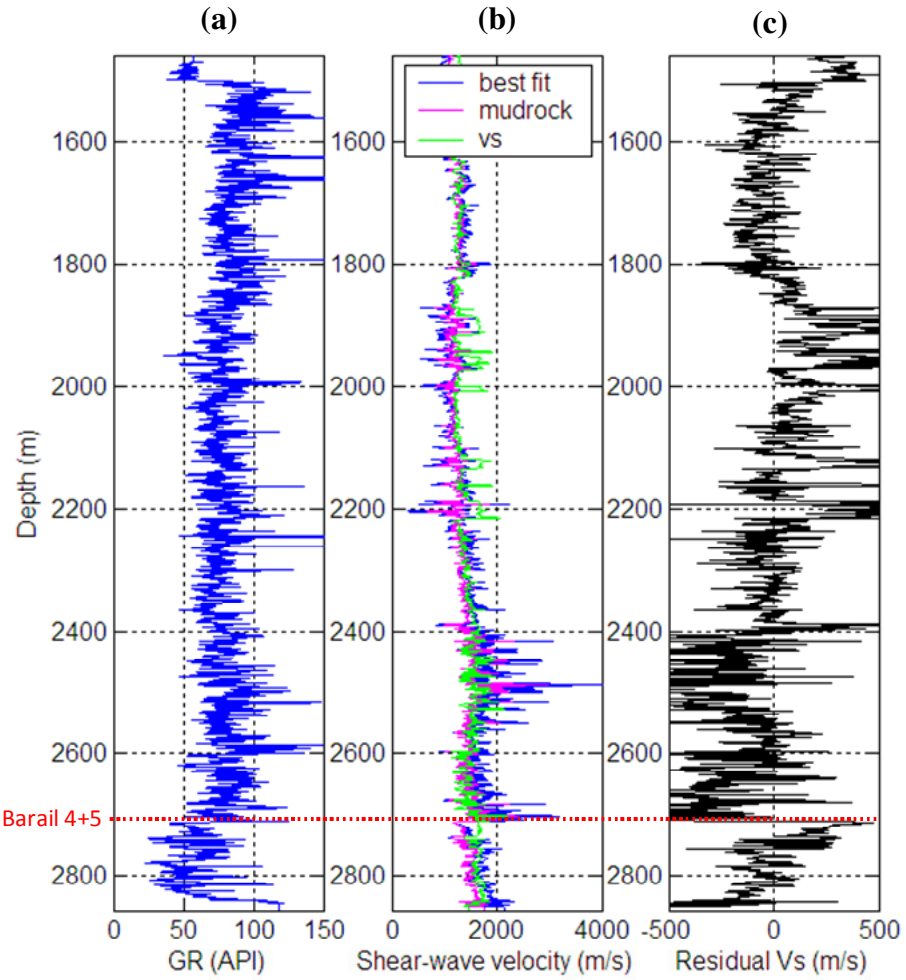

Figure 4.8: (a) GR, (b) Original and modelled S-wave velocity, and (c) residual between the original log and the best fit estimate. Top of the productive interval is highlighted by the dotted red line.

4.4. SYNTHETIC SEISMOGRAMS

PP and PS synthetic seismograms were generated for the two wells to evaluate the seismic response at the top of the reservoirs. None of the synthetics image the Eocene targets, as sonic logs were not available for that interval. The surface seismic data available in the area indicate that there is a signal frequency band from about 10-60Hz for the P-waves. This suggests that we should expect a PS bandwidth from about 5-30Hz. Thus, we have computed the PP synthetic seismograms using a Ricker wavelet with a dominant frequency of 30 Hz, and the PS synthetics with a Ricker wavelet of 15 Hz. No transmission losses or spherical divergence were included in the models.

Synthetic seismograms for Well A show shallow AVO effects, from 1.55s to 1.8s, which are probably related to problematic V_s logs. The logs look more reliable deeper in the section. There is also a strong AVO response at the top of the Barail4 and 5 in the PP synthetic. The PS synthetic seismogram shows a response at the top of the Barail, as well as at the deeper Barail 4 and 5. The PS synthetic seismograms from well B (Figure 4.10) show an amplitude increase with offset at the top of the Barail sand, which is not evident in the PP section. Also note that out to offsets of about 3500m there are little or no changes in polarity. This suggests that an offset-to-depth ratio of about 1.5 is useful.

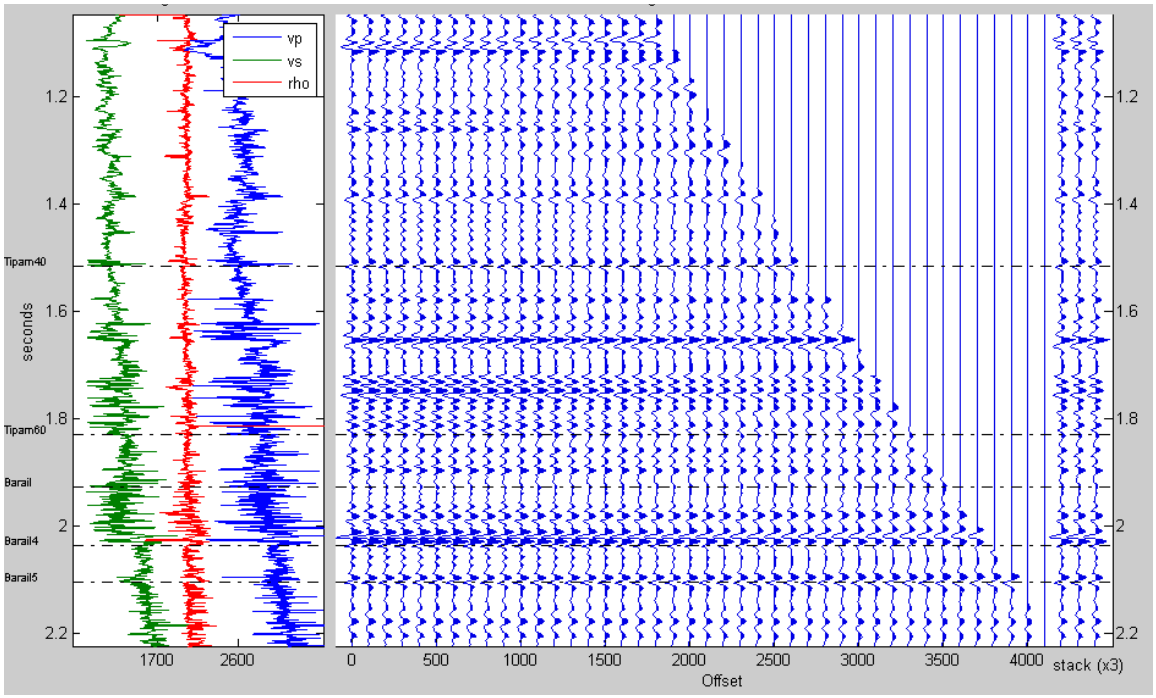

Figure 4.9: PP synthetic seismogram for well B (Deohal field)

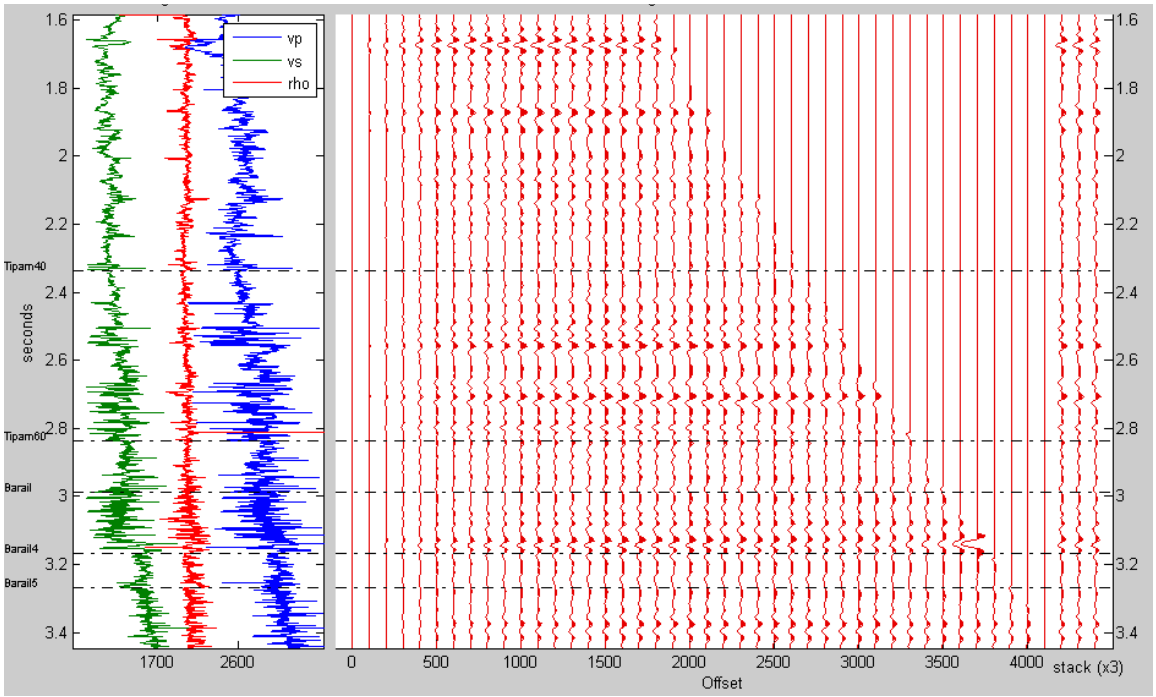

Figure 4.10: PS synthetic for well B (Deohal field)

CHAPTER FIVE: CONCLUSIONS AND RECOMMENDATIONS

5.1. CONCLUSIONS

In the Manitou Lake area, shear-wave velocity is a very good lithological indicator, showing a change of 500 m/s at the sand/shale interface, which should result in significant changes in the PS section. Variations in density are more complex, as it is affected by the saturating fluid. Within the target zone, densities lower than 2250 kg/m^3 corresponds to clean sands, while shaly sands and shales have densities between 2250 and 2600 kg/m^3.

Empirical methods for log modelling, such as Gardner's and the mudrock line, can be very accurate when local parameters and a few constraints are applied to the data. In the Manitou Lake area the values for *a* and *m* in shales are 0.52 and 0.19, and 0.22 and 0.28 in sands, compared to default values of 0.31 and 0.25.

Modelling with the log response equation results in good density estimates; however, it requires significant input from the interpreter, including values for the effective porosity, water saturation and shale volume. Variations observed in the shallow section, between 100 and 350 m depths, likely indicate a drastic change in the elastic properties associated with compaction. Understanding of the local geology properly is necessary in order to effectively apply any of these modelling approaches.

The converted-wave data from the Manitou Lake area has significantly lower frequency content than the PP data, making it difficult to correlate both data sets and to isolate the response associated with the productive sand channels in the Colony and Sparky members. Although there is almost no change in the P-wave velocity at the top of the reservoir, low-impedance areas associated with the Colony sand channels appear in the post-stack P-impedance inversion, indicating the decrease in density in the reservoir is

significant enough to drive the impedance decrease. Inversion results in the Sparky are less definitive, probably due to the thickness of the reservoir, which is below seismic resolution, and the lack of a gas cap at the reservoir.

The map of residual Vs calculated from the P- and S-impedance inversion results shows that the sand intervals are indicated by areas of positive residual values, indicating that Castagna's equation consistently underestimates Vs values in the sands. The residual Vs calculation results in a better definition of the sand intervals than the P-impedance or S-impedance results alone, and could be also used to quantify the effect of fluids by comparing with the P-impedance inversion results.

In our study of the Assam reservoir in India, the reservoir sands also appear to have an anomalous S-wave velocity character that may be detectable using converted-wave methods. Petrophysical analysis and synthetic seismogram modelling show the often distinctive character of the reservoir sands. In general, crossplots from different wells show that good sands are indicated by $V_p/V_s \leq 2$, V_s in the range between 1400 and 1800 m/s, V_p between 2650-3300 m/s, densities between 2150-2350 kg/m^3, and high resistivities.

5.2. FUTURE WORK

A Bayesian inversion approach could be used to estimate the elastic properties, using the crossplots between the elastic properties from the wireline data to estimate probability distributions. This could be the best way to use the log data as a constraint for the inversion results, and would help in quantifying the uncertainty associated with the inversion results.

The use of neural networks and multi-regression attributes could also be useful to estimate densities in the Manitou Lake area, allowing to incorporate the results from the PP and PS inversions with the log information available in a more quantitative approach.

REFERENCES

Asquith, G.B., and D. Krygowski, 2004, Basic Well Log Analysis: AAPG Methods in Explorations Series, No. 16, 2nd Edition.

Archie, G.E., 1942, The Electrical Resistivity log as an aid in determining some reservoir characterisitics: J. Pet. Tech, **5**.

Barnola, A.S., and R.E. White, 2001, Gardner's relation and AVO inversion: First Break, **19**, 607-611.

Berryman, J.G., 1980, Long-wavelength propagation in composite elastic media II. Ellipsoidal inclusions: J. Acoust. Soc. Am., **68**, 1820-1831.

Chi et al., 2004.

Castagna, J.P., M.L. Batzle, and R.L. Eastwood, 1985, Relationships between compressional-wave and shear-wave velocities in elastic silicate rocks: Geophysics, **50**, 571-581.

Castagna, J.P., M.L. Batzle, and T.K. Kan, 1993, Rock physics - The link between rock properties and AVO response *in* Castagna, J.P., and M. Backus, Offset dependent reflectivity, Theory and Practice of AVO analysis: SEG, 135-171.

Chi, S., C. Torres-Verdin, J. Wu, and O.E. Alpak, 2004, Assesment of mud-filtrate invasion effects on borehole acoustic logs and radial profiling of formation elastic parameters: SPE, Paper 90159, 13 p.

Christopher, J. E., 1997, Evolution of the Lower Cretaceous Mannville Sedimentary Basin in Saskatchewan *in* Pemberton, S.G. and James, D.P.(eds.), Petroleum Geology of the Cretaceous Mannville Group, Western Canada, Can. Soc. Petrol. Geol. Memoir, **18**, 191-210.

Christopher, J.E., 2003, Jura-Cretaceous Success Formation and Lower Cretaceous Mannville Group of Saskatchewan: Report 223, Saskatchewan Industry and Resources, Saskatchewan Geological Survey, p.128.

Crain, R., 1986, The Log Analysis Handbook: Pennwell.

CWLS, 2002, Rw maps and data for western Canadian sedimentary basin and North Dakota, northern territories, East Coast: Canadian Well Logging Society, 4th ed.

Downton, J., 2005, Seismic parameter estimation from AVO inversion: Ph.D Thesis, University of Calgary.

Fam, M., and J.C. Santamaria, 1997, A study of consolidation using mechanical and electromagnetic waves: Geotechnique, **47**, 203-219.

Ferguson, R. J., and G.F. Margrave, 1996, A simple algorithm for band-limited impedance inversion: CREWES Research Report, **8**.

Fomel. S., M. Backus, M. DeAngelo, P. Murray, and B. Hardage, 2003, Multicomponent seismic data registration for subsurface characterization in the shallow Gulf of Mexico: Offshore Technology Conference, Houston.

Gaiser, J.E., 1996, Multicomponent Vp/Vs correlation analysis: Geophysics, **61**, 1137-1149.

Gardner, G. H. F., L. W. Gardner, and A. R. Gregory, 1974, Formation velocity and density—the diagnostic basics for stratigraphic traps: Geophysics, **39,** 770–780.

Garotta, R., P.Y.Granger, and H. Dariu, 2002, Combined interpretation of PP and PS data provides direct access to elastic rock properties: The Leading Edge, **21**, 532-535.

Gray, F. D., P. Anderson, and J. Gunderson, 2006, Prediction of Shale Plugs between Wells in Heavy Oil Sands using Seismic Attributes: Natural Resource Research, **15**, no. 2, 102-109.

Greenberg, M.L., and J.P. Castagna, 1992, Shear-wave velocity estimation in porous rocks: theoretical formulation, preliminary verification and applicationsL Geophysical Prospecting, **40**, 195-209.

Han, D.H., and M. Batzle, 1997, Fluid invasion effects on sonic interpretation: 67th Annual International Meeting, SEG, Expanded Abstracts, **16,** 298-301.

Han, D.H., J. Liu, and M. Batzle, 2008, Seismic properties of heavy oils – measured data : The Leading Edge, **27**, 1108-1115.

Han, D.H., A. Nur, and D. Morgan, 1986, effects of porosity and clay content on wave velocities in sandstones: Geophysics, **51**, 2093-

Hanssen, P., A. Ziolkowski, and X. Y. Li, 2003, A quantitative study on the use of converted waves for sub-basalt imaging: Geophysical Prospecting, **51**, 183–193.

Kallweit, R.S., and L.C. Wood, 1982, The limits of resolution of zero-phase wavelets: Geophysics, **47**, 1035-1046.

Kato, A., S. Onozuka, and T. Nakayama, 2008, Elastic property change in a bitumen reservoir during steam injection: The Leading Edge, **27**, 1124-1131.

Kuster, G.T., and M.N. Toksöz, 1974, Velocity and attenuation of seismic waves in two-phase media: Part I. Theoretical formulations: Geophysics, **39**, 587-606.

Leckie, D.A., Bhattacharya, J.P., Bloch, J., Gilboy, C.F., and Norris, B., 1994, Cretaceous Colorado/Alberta Group of the Western Canada Sedimentary Basin *In* Geological Atlas of the Western Canada Sedimentary Basin. G.D. Mossop and I. Shetsen (comps.). Calgary, Canadian Society of Petroleum Geologists and Alberta Research Council, chapter 20. URL <http://www.ags.gov.ab.ca/publications/ ATLAS_WWW/ATLAS.shtml>,[December 13th, 2006].

Leckie, D.A., and D. G. Smith, 1992, Regional setting, evolution, and depositional cycles of the Western Canada Foreland Basin *in* Foreland Basins and Fold Belts, Macqueen, R.W., Leckie, D.A. (Eds.). AAPG Memoir, **55**, 9–46.

Lindseth, R.O., 1979, Synthetic sonic logs – A process for stratigraphic interpretation: Geophysics, **44**, 3-26.

Lu, H.X., K. Hall, R.R. Stewart, D. Feuchtwanger, and B. Szatkowski, 2006, Searching for sand reservoirs: Processing 3C-3D seismic data from Manitou Lake, Saskatchewan: CREWES Research Report, **18**.

Mahmoudian, F., 2006, Linear AVO inversion of multicomponent surface seismic and VSP data: M. Sc. Thesis, University of Calgary.

Mallick, R. K., B. Choudhuri, and P. Vishnunavat, 1997a, An innovative technique resolves apparent anomalies in detection of gas zones based on density-neutron logs: Journal of Petroleum Science and Engineering, **18**, no. 3/4, p. 201–205.

Mathur, N., S.V. Raju, and T.G. Kulkarni, 2001, Improved identification of pay zones through integration of geochemical and log data: A case study from Upper Assam basin, India: AAPG Bulletin, **85**, no. 2, 309-323.

Mavko, G., T. Mukerji, and J. Dvorkin, 1998, The Rock Physics Handbook: Tools for Seismic Analysis in Porous Media: Cambridge University Press, 329 pp.

McCormack, M.D., J.A. Dunbarm and W.W. Sharp, 1984, A case study of stratigraphic interpretation using shear and compressional seismic data: Geophysics, **49**, 509-520.

Minear, M.J., 1982, Clay models and acoustic velocities: 57th Annual SPE of AIME,

Mossop, G.D. and I. Shetsen (comp.), 1994, Geological atlas of the Western Canada Sedimentary Basin; Canadian Society of Petroleum Geologists and Alberta Research

Council, Calgary, Alberta, URL http://www.ags.gov.ab.ca/publications/ATLAS_WWW/ATLAS.shtml, [April 15th, 2007].

Nickel, M., and L. Sonneland, 2004, Automated PS to PP event registration and estimation of a high-resolution Vp-Vs ratio volume: 74th Annual International Meeting, SEG, Expanded Abstracts, **23**, 869-872.

Orr, R.D., J.R. Johnston, and E.M. Manko, 1977, Lower Cretaceous geology and heavy oil potential of the Lloydminster area: Bulletin of Canadian Petroleum Geology, **25**, 1187-1221.

Pickett, G.R., 1963, Acoustic character logs and their applications in formation evaluation: J. Can. Petr. Tech., **15**, 659-667.

Pendrel, J., R.R. Stewart, J. Dufour, B. Goodway, and P. van Riel, 1999, Offset inversion of the Blackfoot P-wave data and discrimination of sandstones and shales: CSEG Convention, Expanded Abstracts, 4 pages.

Potter, C.C., and R.R. Stewart, 1998, Density predictions using V_p and V_s sonic logs: CREWES Research Report, **10**.

Purnell, G. W., 1992, Imaging beneath a high-velocity layer using converted waves: Geophysics, **57**, 1444–1452.

Putnam, P.E., Aspects of the petroleum geology of the Lloydminster heavy oil fields, Alberta and Saskatchewan: Bulletin of Canadian Petroleum Geology, **30**, 81-111.

Putnam, P.E. and T. A. Oliver, 1980, Stratigraphic traps in channel sandstones in the Upper Mannville (Albian) and east-central Alberta. Bulletin of Canadian Petroleum Geology, **28**, 489-508.

Reading, G.H., 1996, Sedimentary Environments: Processes, Facies and Stratigraphy: Blackwell Science, 3rd ed.

Royle, A. J., 2002, Exploitation of an oil field using AVO and post-stack rock property analysis methods: 72nd Annual International Meeting, SEG, Expanded Abstracts, **21**, 289-292.

Russell, B., and D. Hampson, 1991, Comparison of poststack inversion methods: 61st Annual International Meeting, SEG, Expanded Abstracts, **10**, 876-878.

Ryan, B., 2006, Coal Basics for CBM *in* Coal Bed Methane: An integrated Approach to Reservoir Characterization and Production. 2006 CSPG/CSEG/CWLS Joint Convention Short Course.

Schlumberger, 1989, Log Interpretation Principles/Applications: Houston (Schlumberger Educ. Services), SMP-7017.

Sheriff, R.E., 2002, Encyclopedic Dictionary of Applied Geophysics: SEG, 4th ed. p.429.

Smith, G.G. 1989. Coal resources of Canada: Geological Survey of Canada, Paper 89-4, 146 p.

Souboutcheva, N., 2006, Reservoir property prediction form well-logs, VSP and multicomponent seismic data: Pikes Peak heavy oilfield, Saskatchewan: M.Sc. Thesis, University of Calgary.

Stewart, R.R., and H. Bland, 1997, An approximate relationship between R^{ps} and R^{ss}: CREWES Research Report, **9**.

Stewart, R.R., J.E. Gaiser, R.J. Brown, and D.C. Lawton, 2003, Converted-wave seismic exploration: Applications: Geophysics, **68**, 40-

Stewart, R.R., M. F. Quijada, K.L. Mandal and Borgohain, R., 2008, Well log and synthetic seismogram analysis of an oilfield in Assam, India: A 3C seismic development feasibility study: 78th Annual International Meeting, SEG, Expanded Abstract, **25**,

Todorov, T.I., 2000, Integration of 3C-3D seismic data and well logs for rock property estimation: M. Sc. Thesis, University of Calgary.

Vasquez, G.F., L.D. Dillon, C.L. Varela, G.S. Neto, R.Q. Velloso, and C.F. Nunes, 2004, Elastic log editing and alternative invasion correction methods: The Leading Edge, **23**, 20-

Van Koughnet, R. W., C. M. Skidmore, M. C. Kelly, and R. Lindsay, 2003, Prospecting with the density cube: The Leading Edge, **22**, no. 10, 1038-1045.

Vigrass, L.W., 1977, Trapping of oil at intra-Mannville (Lower Cretaceous) disconformity in Lloydminster area, Alberta and Saskatchewan: American Association Petroleum Geologists Bulletin, **61**, 1010-1028.

Wandrey, C.J., 1994, Sylhet-Kopili/Barail-Tipam composite total petroleum system, Assam geologic province, India *in* Petroleum systems and related geologic studies in region 8, South Asia: U.S. Geological Survey Bulletin 2208-D. (Posted online June 2004, version1)

Wang, Y., 1999, Simultaneous inversion for model geometry and elastic parameters: Geophysics, **64**, 182-190.

Wang, Z., 2000, Velocity relationships in granular rocks, in Z. Wang and N. Amos, eds., Seismic and acoustic velocities in reservoir rocks, vol. 3: Geophysics Reprint series, 377–383.

Waters, K.H., 1978, Reflection Seismology: John Wiley and Sons.

Widess, M.B., 1973, How thin is a thin bed?: Geophysics, **38**, 1176-

Xu, S, and R.E. White,1995, A new velocity model for clay-sand mixtures: Geophysical Prospecting, **43**, 91-118.

Zimmer, M.A., M. Prasad, G. Mavko, and A. Nur, 2007, Seismic velocities of unconsolidated sands: Part I – Pressure trends from 0.1 to 20 MPa: Geophysics, **1**, E1-E13.

Zou, K., J. Dai, H. Xu, A. HannAn, and A. Koesoemadinata, 2006, A practical workflow of PP/PS event registration in multicomponent data interpretation: 68th Conference and Exhibition, EAGE, Expanded Abstracts.

APPENDIX A: LOG ANALYSIS OF WELLS FROM MANITOU LAKE.

The first step in a log analysis is to identify the zones of interest (clean zones with hydrocarbons), and define clean and shale baselines on the logs. The top of the Colony sand is clearly identified in all wells by a significant deviation to the right in the GR, SP and porosity logs, as we pass from the marine shales of the Joli Fou formation to the channel sands of the Colony member. The depth of this top varies between 547.5 m and 554 m in the three wells. The Sparky B member is thinner and shalier than the Colony in these particular wells, with lower resistivities but similar porosities. The zones of interest for the petrophysical interpretation (See Table A.1) were defined in terms of clean zones with hydrocarbon saturation (low GR and high resistivity), as well as two water zones used to calculate water resistivity at formation temperature, which is necessary to calculate water saturation and permeability.

Table A.1: Summary of analyzed zones in each well (Formation/Fluid).

	Well A11-17	Well C07-16	Well C10-17
Zone 1	Colony/Gas	Colony/Gas	Colony/Gas
Zone 2	Colony/Oil	Colony/Oil	Colony/Oil
Zone 3	Sparky/Oil	Colony/Water	Sparky/Oil
Zone 4	Lloydminster/Water	Sparky/Oil	Lloydminster/Water

After picking clean and shale lines on the logs, the next step is shale volume estimation. In this study, shale volume (V_{sh}) was calculated by the three common methods (Equations A.1 to A.3), which use values from the gamma ray (GR), spontaneous potential

(SP), and neutron (PHIN) and density (PHID) porosity logs, with the minimum of the three being selected as the shale volume

$$V_{shg} = \frac{GR - GR_{clean}}{GR_{shale} - GR_{clean}}, \tag{A.1}$$

$$V_{shs} = \frac{SP - SP_{clean}}{SP_{shale} - SP_{clean}} \text{ , and} \tag{A.2}$$

$$V_{shhx} = \frac{PHIN - PHID}{PHIN_{shale} - PHID_{shale}}. \tag{A.3}$$

GR, SP, PHIN and *PHID* are the picked log values, while *clean* and *shale* indicate values picked in the clean and shale base lines, respectively.

Porosity from logs is considered total porosity (*PHIt*), which includes the bound water in the shale; to obtain effective porosity (*PHIe*) it must be corrected for shale volume. When both the neutron and density porosity curves are available, as in this case, the best method for correcting porosity is the Complex Lithology Density Neutron Crossplot. First, porosity is corrected for shale volume by

$$PHIxc = PHID - \left(V_{sh} \times PHI_{shale}\right) \tag{A.4},$$

where x will be n for neutron or d for density porosity. Effective porosity is then calculated as:

$$PHI_e = \frac{PHI_{nc} + PHI_{dc}}{2}. \tag{A.5}$$

This method works equally well in quartz sands as in mixtures, except in areas with bad hole conditions which affect the density reading (Crain, 2006).

The density and neutron porosity logs show cross-over at the top of the Mannville, suggesting the presence of gas. For this reason, the porosity in the uppermost interval was

corrected using the equation for neutron-density porosity in a gas zone (Asquith and Krygowski, 2004)

$$PHIe_{NDgas} = \sqrt{\frac{PHI_{dc}^2 + PHI_{nc}^2}{2}} \,. \tag{A.6}$$

To calculate water saturation, most methods require a water resistivity (R_w) value. In this case, an obvious clean water zone is present in two of the wells in the area and the water resistivity was calculated from the porosity and resistivity in this zone, using the *Ro* method, given by the following equation:

$$RW\ @\ FT = \frac{PHI_{wtr}{}^{m} Ro}{a} \,. \tag{A.7}$$

RW@FT is the water resistivity at formation temperature, PHI_{wtr} and R_o are the total porosity and deep resistivity values in the water zone, *a* is the tortuosity factor and *m* is the cementation exponent.

Water saturation (S_{wa}) can then be calculated using Archie's method, given by:

$$S_{wa} = \left(\frac{RW\ @\ FT}{R_{wa}} \right)^{1/n} , \tag{A.8}$$

where *n* is the saturation exponent and R_{wa} is water resistivity in the zone of interest, calculated in the same manner as *RW@FT*:

$$R_{wa} = \frac{PHI_t{}^{m} * RESD}{a} \tag{A.9}$$

Note that in the water zone, saturation should be equal to 1, as *RW@FT* is equal to R_{wa}. The parameters *a*, *m* and *n* should be determined from core analysis if possible; however, in this case, *a*, *m* and *n* were set to 0.62, 2.15 and 2, respectively, based on usual values for unconsolidated sandstones.

Permeability (*Perm*) is calculated using the Wyllie-Rose method considering Morris-Biggs parameters, which is generally used when no core data is available:

$$Perm_w = \frac{CPERM * (PHI_e)^{DPERM}}{(SW_{ir})^{EPERM}}, \quad \text{(A.10)}$$

where SW_{ir} is the irreducible water saturation, and *CPERM*, *DPERM* and *EPERM* are constants, which should be adjusted by core calibration. In this case, they were set to Morris-Biggs values (65000, 6 and 2, respectively, for the oil-saturated zoned and 6500, 6 and 2 for the gas-saturated zones). SW_{ir} is assumed to be equivalent to the water saturation estimated from Archie's equation.

Finally, the productivity and reserves of the intervals of interest are estimated, along with an estimated flow rate. These values are a useful way of comparing the quality of wells from similar reservoirs, even when results are not calibrated (Crain, 2006).

Tables A.2-A.4 summarize the results from the log analysis from all three wells in the area. The picked values for each zone in every well and all intermediate calculations are shown in Tables A.5-A.7. The productivity calculations are expressed by the values *HPV* (Hydrocarbon volume per unit area), *NetH* (net pay thickness), R_{oil} (recoverable reserves of oil), Q_o (Calculated oil productivity), R_{gas} (recoverable reserves of gas) and Q_g (Calculated gas productivity).

Wells A11-17 and C10-17 are located very close to each other within the same sand channel, and the log analysis results in very similar values for the different parameters in both wells. The Colony channel has a thickness of approximately 8 m in both wells, with a gas cap of 2 m, and the remaining 6 m being saturated with oil. The Sparky B member shows a thickness of 3 m. Porosities are very high in all the interpreted zones, ranging from 0.3 to 0.38. The difference between neutron and density porosity is small in all zones,

except where there is gas present and significant cross-over occurs. This, coupled with the low shale volumes, results in effective porosities very similar to the total, except in the gas bearing zones, where a corrected equation for effective porosity is used and results in lower porosity values.

The three water zones used to calculate water resistivities at formation temperature give consistent results, between 0.13 and 0.15 Ωm. However, permeabilities calculated within the oil zone in the Colony sand are extremely high (between 8000 and 30000 mD) due to the very high resistivities and porosities of the interval. This probably implies that the default values of CPERM, EPERM and DPERM used are not appropriate for this area, and calibration with core is necessary to obtain better parameters.

The productivity parameters calculated are significantly affected by the permeability calculation, so they will only be considered comparatively between one well to another. Note that results for wells C10-17 and A11-17 are very similar, both for the Colony and the Sparky members, although there is significant variation in the flow rate for the Colony. This interval shows higher reserves and productivity than the Sparky, due to the higher permeability and thickness. The results for well C07-16 are consistent with those of the other two wells, although it has been interpreted to be located within a different channel.

Table A.2: Summary of results from log analysis in well A11-17-44-27

Zone	Top (m)	Bottom (m)	Vsh (frac)	PHIe (frac)	Sw (frac)	Perm (md)
1	553.5	555	0.0476	0.23	0.11	80.97
2	555	561	0.0761	0.33	0.06	20516
3	610	613	0.12	0.32	0.14	3795.07
4	646	654	0.0	0.35	1	119.48
Zone	**HPV (m)**	**NetH (m)**	**Roil (10^3m^3)**	**Qo (m^3/day)**	**Rgas (10^3m3)**	**Qg (m^3/day)**
1	0.30	1.5	N/A	N/A	5869	81.28
2	1.86	6	476.488	167.87	N/A	N/A
3	0.77	3	213.768	23.43	N/A	N/A
4	N/A	N/A	N/A	N/A	N/A	N/A

Table A.3: Summary of results from log analysis in well C10-17-44-27

Zone	Top (m)	Bottom (m)	Vsh (frac)	PHIe (frac)	Sw (frac)	Perm (md)
1	554	556	0.0442	0.18	0.21	5.46
2	556	561	0.0619	0.34	0.05	33847
3	609	612.5	0.1428	0.29	0.14	1964.47
4	648	655	0.0595	0.30	1	52.23
Zone	**HPV (m)**	**NetH (m)**	**Roil (10^3m^3)**	**Qo (m^3/day)**	**Rgas (10^3m^3)**	**Qg (m^3/day)**
1	0.28	2	N/A	N/A	5449	7.27
2	1.62	5	414.074	319.14	N/A	N/A
3	0.87	3.5	222.976	19.40	N/A	N/A
4	N/A	N/A	N/A	N/A	N/A	N/A

Table A.4: Summary of results from log analysis in well C7-16-44-27

Zone	Top (m)	Bottom (m)	Vsh (frac)	PHIe (frac)	Sw (frac)	Perm (md)
1	547.5	553	0.0462	0.19	0.14	13.94
2	553	561	0.0462	0.34	0.10	8136
3	561	580	0.1667	0.28	1	3.21
4	606.5	608.5	0.0462	0.36	0.14	742.86
Zone	**HPV (m)**	**NetH (m)**	**Roil (10^3m3)**	**Qo (m^3/day)**	**Rgas (10^3m^3)**	**Qg (m^3/day)**
1	0.88	5.5	N/A	N/A	16593	50.28
2	2.4	8	613.33	114.04	N/A	N/A
3	N/A	N/A	N/A	N/A	N/A	N/A
4	0.62	2	158.58	3.85	N/A	N/A

The base lines picked for each zone, as well as the detailed calculations and intermediate values, are shown in Table A.5-A.7. All calculations were done following the petrophysical analysis defined in Crain (1986).

Table A.5: Parameters and petrophysical calculations for well A11-17

	A11-17			
PARAMETERS:	Colony gas	Colony Oil	Sparky oil	Lloyd Water
GR clean line (GR0)	30	30	30	30
GR shale line (GR100)	135	135	135	135
SP clean line (SP0)	-50	-50	-50	-50
SP shale line (SP100)	27	27	27	27
DPHI shale line (PHIDSH)	0.2	0.2	0.2	0.2
NPHI shale line (PHINSH)	0.45	0.45	0.45	0.45
Sonic shale line (DELTSH)				
Resisitivity shale line (RSH)	2.5	2.5	2.5	2.5
Resisitivity of water zone (R0)	0.9	0.9	0.9	0.9
Bottom hole temperature (BHT)	22	22	22	22
Surface temperature (SUFT)	10	10	10	10
Bottom hole depth (BHTDEP)	707	707	707	707
	Zone 1	Zone 2	Zone 3	Zone 4
Layer top (m)	553.5	555	610	646
Layer bottom (m)	555	561	613	654
Deep Resistivity (RESD)	77	200	40	0.9
Neutron porosity (PHIN)	0.3	0.375	0.38	0.4
Density porosity (PHID)	0.38	0.34	0.35	0.3
Sonic travel time (DELT)				
Gamma Ray (GR)	35	38	50	53
Spontaneous potential (SP)	-24	-30	-38	-50
Photo-electric effect (PE)	1.9	2.1	1.9	1.9
Caliper (CAL)	234	234	234	234
Shale Volume				
Vshg (Using GR)	0.047619048	0.07619048	0.19047619	0.219047619
Vshs (Using SP)	0.337662338	0.25974026	0.155844156	0
Vshx	-0.32	0.14	0.12	0.4
Vsh (min of three)	0.047619048	0.07619048	0.12	0
Porosity				
PHIdc	0.37047619	0.3247619	0.326	0.3
PHInc	0.278571429	0.34071429	0.326	0.4
PHIxdn	0.231762081	0.3327381	0.326	0.35
PHIsc	0	0	0	0
PHIe=PHIxdn	0.231762081	0.3327381	0.326	0.35
Water Resistivity				
PHIwtr	0.35	0.35	0.35	0.35
RW@FT	0.151913761	0.15191376	0.151913761	0.151913761
Water Saturation				
PHIt	0.34	0.3575	0.365	0.35
Rwa	12.21177257	35.3331051	7.389209168	0.151913761

Swa	0.111534495	0.06557037	0.143383632	1
Sw	0.111534495	0.06557037	0.143383632	1
Irreducible water saturation				
KBUCKL	0.025849467	0.02181776	0.046743064	0.35
Swir	0.111534495	0.06557037	0.143383632	1
Permeability				
PERMw=perm	80.97467951	20516.9691	3795.070099	119.4872656
Fluid Properties				
PF	5764.2	5803.2	6359.6	6760
PF in psi	835.809	841.464	922.142	980.2
PS	100.21	100.21	100.21	100.21
FT	19.40735502	19.4710042	20.37906648	21.03253182
FT in Fahrenheit	66.93323904	67.0478076	68.68231966	69.85855728
DENShy	982.6388889	982.638889	982.6388889	982.6388889
GOR	1307.820833	1317.32683	1453.323663	1551.591875
Bo	1.002214569	1.00227698	1.003278408	1.004135231
VISd	34050.97493	33352.1525	25013.58796	20519.45793
VISo	32.37300036	31.6154036	22.98926982	18.64819914
Reserves				
NetH=THICK	1.5	6	3	8
PV	0.347643121	1.99642857	0.978	2.8
HPV	0.308868921	1.86552201	0.837770808	0
Kh	121.4620193	123101.814	11385.2103	955.898125
Roil	78895.72386	476488.679	213768.5064	0
Bg	74.22750428	74.713457	81.62342013	86.56960231
Rgas	5869201.712	35681177.1	17505719.97	0
Productivity				
Qo	0.160657801	167.876586	23.43525517	2.580815997
Qg	81.28810425	83505.81	9274.826474	879.5633632
Reserves:				
RF	0.4	0.4	0.4	0.4
KV3 (metric)	1	1	1	1
AREA	640000	640000	640000	640000
Productivity:				
KV1	0.00000756	0.00000756	0.00000756	0.00000756
KV2	0.0000061	0.0000061	0.0000061	0.0000061
KT2	273	273	273	273
ZF	0.75	0.75	0.75	0.75

Table A.6: Parameters and petrophysical calculations for well C10-17

	C10-17			
PARAMETERS:	Colony gas	Colony Oil	Sparky oil	Lloyd Water
GR clean line (GR0)	22	22	22	22
GR shale line (GR100)	135	135	135	135
SP clean line (SP0)	-70	-70	-70	-70
SP shale line (SP100)	14	14	14	14
DPHI shale line (PHIDSH)	0.225	0.225	0.225	0.225
NPHI shale line (PHINSH)	0.45	0.45	0.45	0.45
Sonic shale line (DELTSH)				
Resisitivity shale line (RSH)	3	3	3	3
Resisitivity of water zone (R0)	0.9	0.9	0.9	0.9
Bottom hole temperature (BHT)	25	25	25	25
Surface temperature (SUFT)	10	10	10	10
Bottom hole depth (BHTDEP)	709	709	709	709
	Zone 1	Zone 2	Zone 3	Zone 4
Layer top	554	556	609	648
Layer bottom	556	561	612.5	655
Deep Resistivity (RESD)	50	220	40	0.9
Neutron porosity (PHIN)	0.05	0.38	0.36	0.35
Density porosity (PHID)	0.375	0.35	0.32	0.3
Sonic travel time (DELT)				
Gamma Ray (GR)	27	29	40	40
Spontaneous potential (SP)	-40	-60	-58	-65
Photo-electric effect (PE)	1.8	1.8	2	1.9
Caliper (CAL)	222	222	222	222
Shale Volume				
Vshg	0.044247788	0.061946903	0.159292035	0.159292035
Vshs	0.357142857	0.119047619	0.142857143	0.05952381
Vshx	-1.444444444	0.133333333	0.177777778	0.222222222
Vsh	0.044247788	0.061946903	0.142857143	0.05952381
Porosity				
PHIdc	0.365044248	0.336061947	0.287857143	0.286607143
PHInc	0.030088496	0.352123894	0.295714286	0.323214286
PHIxdn	0.18314108	0.34409292	0.291785714	0.304910714
PHIsc	0	0	0	0
PHIe=PHIxdn	0.18314108	0.34409292	0.291785714	0.304910714
Water Resistivity				
PHIwtr	0.325	0.325	0.325	0.325
RW@FT	0.129538853	0.129538853	0.129538853	0.129538853
Water Saturation				
PHIt	0.2125	0.365	0.34	0.325
Rwa	2.886689176	40.64065042	6.343777956	0.129538853
Swa	0.211836119	0.056457247	0.142897962	1

Sw	0.211836119	0.056457247	0.142897962	1
Irreducible water saturation				
KBUCKL	0.038795896	0.019426539	0.041695584	0.304910714
Sw	0.211836119	0.056457247	0.142897962	1
Permeability				
PERMw=perm	5.465475563	33847.63925	1964.470155	52.23354104
PF	5772	5808.4	6351.8	6775.6
PF in psi	836.94	842.218	921.011	982.462
PS	100.21	100.21	100.21	100.21
FT	21.74188999	21.81593794	22.92136812	23.78349788
FT in Fahrenheit	71.13540197	71.26868829	73.25846262	74.81029619
DENShy	982.6388889	982.6388889	982.6388889	982.6388889
GOR	1303.448279	1312.241757	1443.818727	1546.792688
Bo	1.003538108	1.003618537	1.004954113	1.006181278
VISd	16683.04495	16333.99827	12030.80659	9594.356638
VISo	23.39798366	22.88418889	16.74315068	13.41703174
Reserves				
NetH=THICK	2	5	3.5	7
PV	0.36628216	1.720464602	1.02125	2.134375
HPV	0.288690368	1.623331907	0.875315456	0
Kh	10.93095113	169238.1963	6875.645542	365.6347873
Roil	73644.17331	414074.6235	222976.1078	0
Bg	73.73922492	74.18560942	80.82293154	85.96508961
Rgas	5449677.827	30829533.9	18110863.66	0
Productivity				
Qo	0.020031868	319.1413517	19.40834829	1.37527485
Qg	7.277566936	114096.9685	5539.211706	334.8812887
Reserves:				
RF	0.4	0.4	0.4	0.4
KV3 (metric)	1	1	1	1
AREA	640000	640000	640000	640000
Productivity:				
KV1	0.00000756	0.00000756	0.00000756	0.00000756
KV2	0.0000061	0.0000061	0.0000061	0.0000061
KT3	273	273	273	273
ZF	0.75	0.75	0.75	0.75

Table A.7: Parameters and petrophysical calculations for well C07-16

	C07-16			
PARAMETERS:	Colony Gas	Colony Oil	Colony water	Sparky Oil
GR clean line (GR0)	27	27	27	27
GR shale line (GR100)	135	135	135	135
SP clean line (SP0)	-90	-90	-90	-90
SP shale line (SP100)	0	0	0	0
DPHI shale line (PHIDSH)	0.225	0.225	0.225	0.225
NPHI shale line (PHINSH)	0.45	0.45	0.45	0.45
Sonic shale line (DELTSH)	420	420	420	420
Resisitivity shale line (RSH)	2.5	2.5	2.5	2.5
Resisitivity of water zone (R0)	1	1	1	1
Bottom hole temperature (BHT)	23	23	23	23
Surface temperature (SUFT)	10	10	10	10
Bottom hole depth (BHTDEP)	640	640	640	640
	Zone 1	Zone3	Zone 2	
Layer top	547.5	553	561	606.5
Layer bottom	553	561	580	608.5
Deep Resistivity (RESD)	100	78	1	40
Neutron porosity (PHIN)	0.11	0.375	0.375	0.38
Density porosity (PHID)	0.375	0.33	0.3	0.375
Sonic travel time (DELT)	364	364	364	364
Gamma Ray (GR)	32	32	45	32
Spontaneous potential (SP)	-77	-77	-85	-80
Photo-electric effect (PE)	1.9	1.9	1.9	1.9
Caliper (CAL)	217	217	217	217
Shale Volume				
Vshg	0.046296296	0.046296296	0.166667	0.0462963
Vshs	0.144444444	0.144444444	0.055556	0.1111111
Vshx	-1.177777778	0.2	0.333333	0.0222222
Vsh	0.046296296	0.046296296	0.166667	0.0462963
Porosity				
PHIdc	0.364583333	0.319583333	0.2625	0.3645833
PHInc	0.089166667	0.354166667	0.3	0.3591667
PHIxdn	0.187664396	0.336875	0.28125	0.361875
PHIsc	0.58451897	0.58451897	0.661585	0.584519
PHIe=PHIxdn	0.187664396	0.336875	0.28125	0.361875
Water Resistivity				
	0.3375	0.3375	0.3375	0.3375
#VALUE!	0.156097854	0.156097854	0.156098	0.1560979
Water Saturation				
PHIt	0.2425	0.3525	0.3375	0.3775
Rwa	7.668996822	13.36887997	0.156098	7.9440095

Swa	0.142668859	0.108056514	1	0.1401776
Sw	0.142668859	0.108056514	1	0.1401776
Irreducible water saturation				
KBUCKL	0.026773865	0.036401538	0.28125	0.0507268
Sw	0.142668859	0.108056514	1	0.1401776
Permeability				
PERMw=perm	13.94910324	8136.247376	3.21713	742.86119
PF	5722.6	5792.8	5933.2	6318
PF in psi	829.777	839.956	860.314	916.11
PS	100.21	100.21	100.21	100.21
FT	21.17695313	21.3140625	21.58828	22.339844
FT in Fahrenheit	70.11851563	70.3653125	70.85891	72.211719
DENShy	982.6388889	982.6388889	982.6389	982.63889
GOR	1292.752671	1309.737192	1343.737	1437.1213
Bo	1.003173643	1.003318457	1.00362	1.0045292
VISd	19659.73366	18882.86356	17435.87	14098.347
VISo	25.6430756	24.56147662	22.57533	18.13256
Reserves				
NetH=THICK	5.5	8	19	2
PV	1.032154175	2.695	5.34375	0.72375
HPV	0.884897917	2.403787694	0	0.6222965
Kh	76.72006783	65089.979	61.12546	1485.7224
Roil	225817.2036	613334.3264	0	158589.61
Bg	73.24852015	74.11252861	75.83813	80.55114
Rgas	16593270.51	45606600.77	0	12832433
Productivity				
Qo	0.127169109	114.048968	0.119399	3.8515575
Qg	50.28889609	43717.24285	43.06446	1186.3629
Reserves:				
RF	0.4	0.4	0.4	0.4
KV3 (metric)	1	1	1	1
AREA	640000	640000	640000	640000
Productivity:				
KV1	0.00000756	0.00000756	7.56E-06	7.56E-06
KV2	0.0000061	0.0000061	6.1E-06	0.0000061
KT4	273	273	273	273
ZF	0.75	0.75	0.75	0.75

APPENDIX B: VS MODELLING USING WELL LOGS FROM BLACKFOOT, ALBERTA.

The Blackfoot field is located in southern Alberta, about 15 km southeast of Strathmore. The main target in the area are incised, valley-fill sediments consisting of very fine to medium grained quartz sandstone, within the Glauconitic formation of the Mannville group (Todorov, 1999). In the Blackfoot area, the thickness of the valley-fill sediments vary from 0 to ever 35 m. Three phases of channel development have been identified, with different degrees of incision and different quality of sands deposited, with porosities up to 18 % (Pendrel, 1998)

In the Blackfoot area, as occurs in Manitou Lake, the analysis of P-wave seismic data can lead to ambiguous results, since the prospective channel sands and the non-productive shales have similar P-wave impedance response. Previous studies in the area (Miller et el., 1995, Pendrel et al., 1998) have shown that additional S-wave information can help in the differentiation of sands and shales.

The Vs residual evaluated in Section 2.5.3 was also applied to logs from the Balckfoot area, in order to verify the results obtained in Manitou Lake, and generalize the application of this methodology. Well 08-08 in the Blackfoot field had a full suite of logs, including P- and S-wave sonic logs (Figure B.1) at the reservoir interval, between 1400 and 1600 m. The GR log shows a predominantly shaly section, with the main sand intervals occuring within the Glauconitic formation. The Lower Cretaceous sediments rest above eroded Mississippian carbonates, indicated by very low GR, and high Vp and Vs values. There are also several coal seams above the reservoir interval, indicated by very low density values below 1500 m depth.

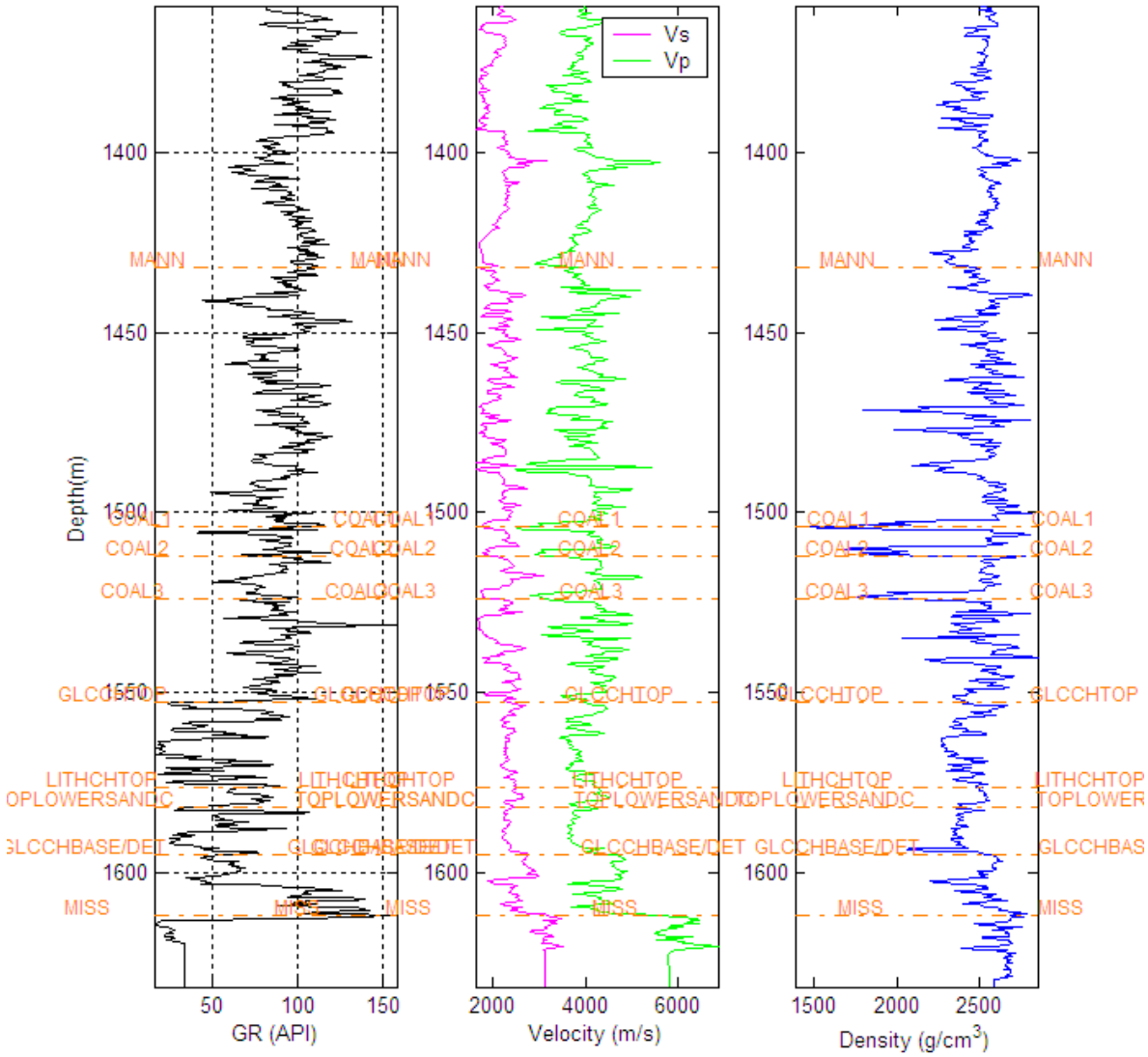

Figure B.1: Suite of logs for well 08-08 in the Blackfoot field. (a) GR log, (b) P- and S-wave velocities and (c) density. Formation tops are shown in orange.

.

Castagna's relation between Vp and Vs is defined as $V_p = 1.16V_s + 1.36$, where the velocities are in km/s. A linear least-square fit of the P- and S-wave velocities logs from the Blackfoot field results in a slope of 1.4 and an intercept of 1.53. A scatter plot of P- versus S-wave velocity using the logs from well 08-08, with the mudrock line in black, and the least-squares fit in blue, is shown in Figure B.2. The deviation between the two curves increases with decreasing S-wave velocities. The points with low GR values and high P- and S-wave velocities outliying the mudrock trend correspond to Mississippian carbonates.

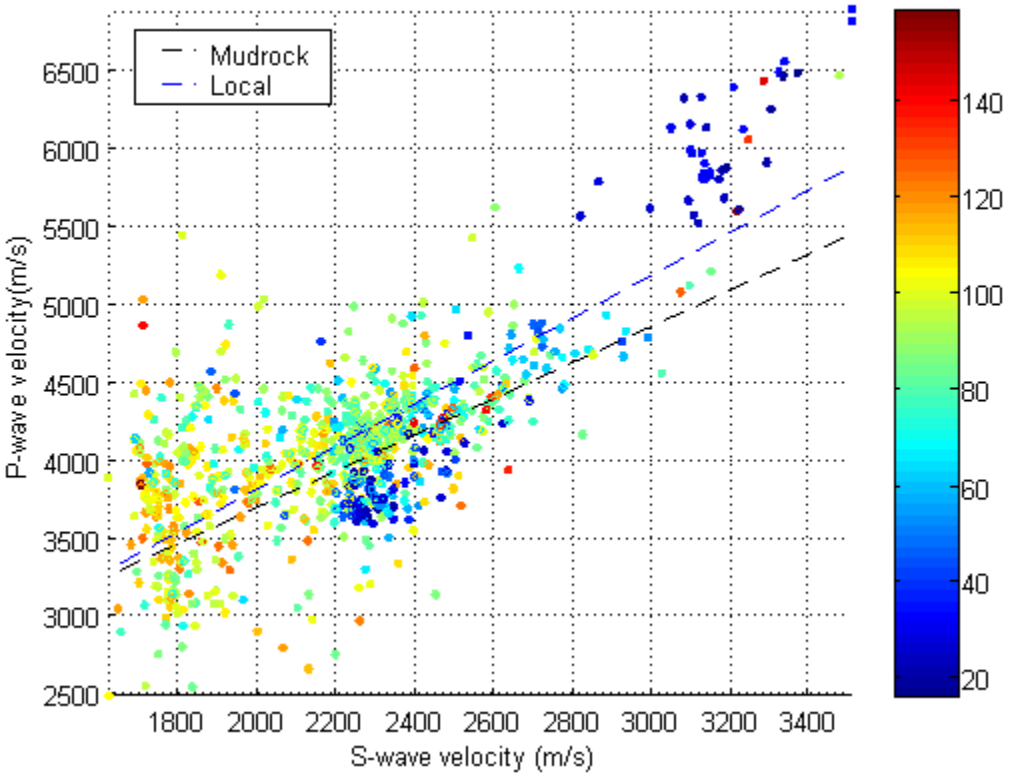

Figure B.2: P- versus S-wave velocity crossplot. Mudrock line is shown in black and best fit line is shown in blue. Colorbar indicates GR values.

The mudrock line and the locally fitted relation between Vp and Vs were used to predict shear-wave velocities in well 08-08 (Figure B.3). Note that the residual using the default mudrock line (Figure B.3c) appears to give a better separation between the sands and the shales, with most shale intervals showing negative residuals, and sand intervals showing positive residuals, assuming a cutoff of 60 API units for the sands. The points with very low GR values at the bottom of the logs correspond to the Mississippian carbonates and show very high negative residuals, between -700 to -1000 m/s, highlighting the inapplicability of Castagna's empirical fit for clastics to carbonate rocks.

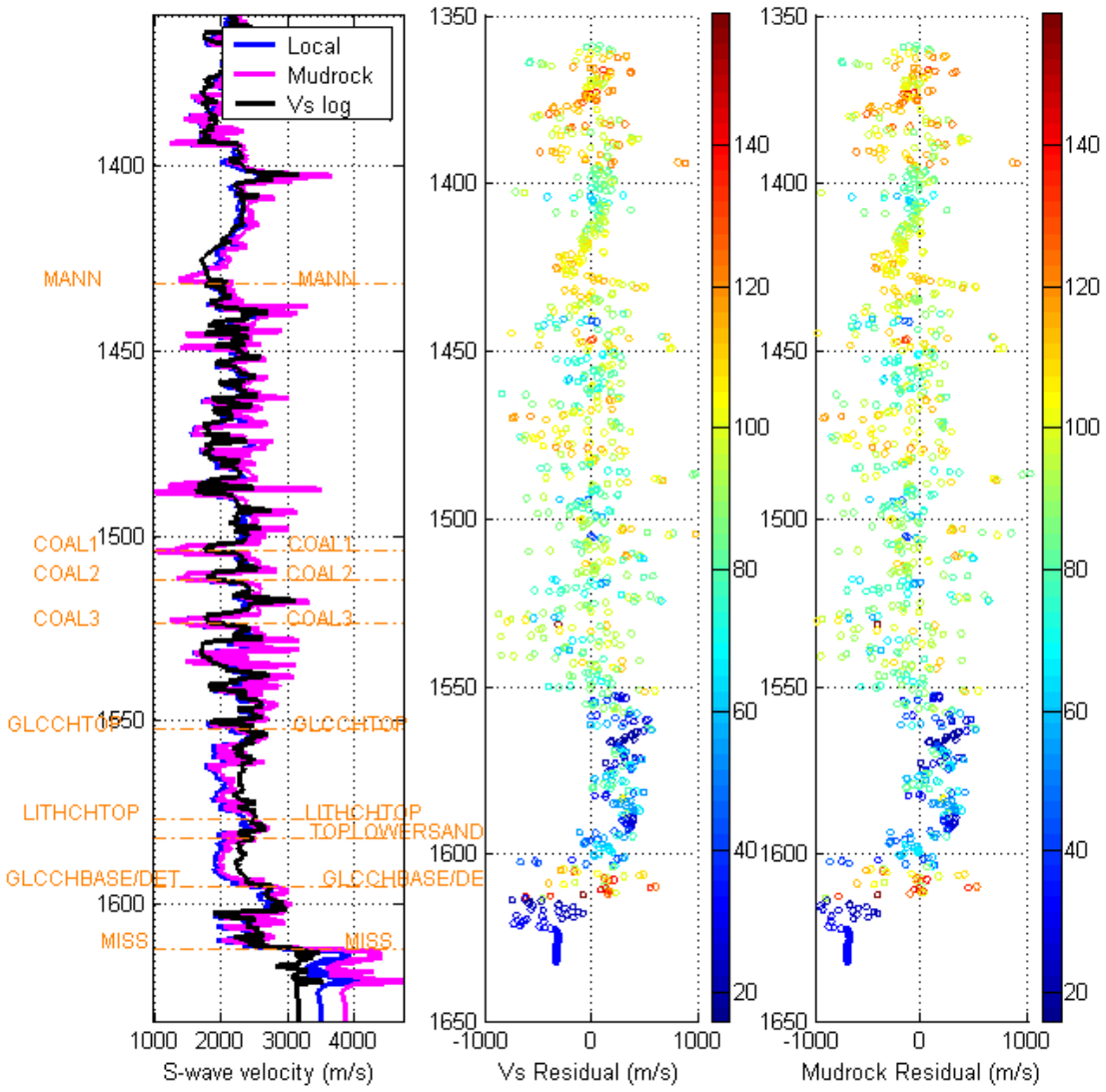

Figure B.3: (a) Predicted and original Vs logs using the mudrock line and the best fit parameters, (b) difference between the original Vs log and modelled Vs using the best fit, and (c) difference between original Vs log and modelled Vs with mudrock line.

The calculation of the Vs residual in Manitou Lake and Blackfoot fields in Alberta, and in Assam, India suggests that it can be used to identify zones with high sand content, which in all cases evaluated are associated with anomalously higher S-wave velocities than those predicted by the mudrock line.

APPENDIX C: PROCESSING FLOW

The following steps were followed in the processing flow for the Manitou Lake CDP gathers for AVO analysis (Lu, Pers. Comm, 2008):

- SEGY input
- 3D Geometry assignment
- True amplitude recovery
- Elevation statics and refraction statics
- Surface consistent Deconvolution
- Front end muting
- Velocity analysis
- Residual surface consistent statics
- Normal moveout
- Trim statics

For the migrated section, the following steps were applied:

- Decon
- Time variant spectral whitening.
- CDP stack:
- FD migration.

APPENDIX D: MODEL-BASED INVERSION THEORY

The model-based post-stack inversion the8ory is summarized in Russell and Hampson (1991). The model-based inversion is based on perturbing a low-frequency P-impedance model until the synthetic traces fits the seismic data, assuming zero-offset incidence. The method is based on the convolutional model, where the seismic trace is modelled as the convolution of the earth's reflectivity (R) and a bandlimited seismic wavelet (W), as defined by equation C.1:

$$S = W * R \tag{C.1}$$

The zero-offset P-wave reflectivity (R_{Pi}) is related to the acoustic impedance (Z) by:

$$R_{Pi} = \frac{Z_{i+1} - Z_i}{Z_{i+1} + Z_i}, \tag{C.2}$$

where Z_i is the impedance of the i^{th} layer, and Z_{i+1} is the impedance of the underlying layer. Assuming small reflection coefficients, this can be linearized as:

$$R_{Pi} \approx \frac{\Delta Z_{Pi}}{2Z_{Pi}}, \tag{C.3}$$

where $Z_{Pi} = \frac{Z_{Pi+1} + Z_{Pi+1}}{2}$ and $\Delta Z_{pi} = Z_{Pi+1} - Z_{Pi}$.

The logarithm of the impedance can be written as:

$$\frac{d \ln (Z(t))}{dt} = \frac{1}{Z(t)} \frac{dZ(t)}{dt}, \tag{C.4}$$

and removing the dt term in this equation, using Δ instead of d, and combining with equation C.3, results in:

$$R_{Pi} \approx \frac{1}{2} \Delta ln Z_{pi} = \frac{1}{2} [ln Z_{Pi+1} - ln Z_{Pi}]. \tag{C.5}$$

For an n sample reflectivity, this can be written in matrix form as:

$$\begin{bmatrix} R_{P1} \\ \vdots \\ R_{Pn} \end{bmatrix} = \frac{1}{2}\begin{bmatrix} -1 & 1 & 0 \cdots \\ 0 & -1 & 1 \ddots \\ \vdots & \ddots & \ddots \ddots \end{bmatrix}\begin{bmatrix} L_{P1} \\ \vdots \\ L_{Pn} \end{bmatrix}; \tag{C.6}$$

where L_{Pi}=ln(Z_{Pi}), and the matrix consisting of all 1's and -1's can be thought of as a derivative matrix D. Rewriting C.1 in matrix and combining with C.6 results in the forward model hich relates the seismic trace t the logarithm of the P-impedance:

$$S=(1/2)WDL_p., \tag{C.7}$$

where S_i represents the i^{th} sample of the seismic trace, and W_j represents the j^{th} term of an extracted seismic wavelet.

Equation C.7 can then be inverted using a standard matrix inversion technique, however, this can be costly and potentially unstable. To overcome this problem, the implementation used in STRATA is to start with the initial guess impedance model and iterate towards a solution using the conjugate gradient method.